

# DISSERTATION

submitted to the  
Combined Faculties for the Natural Sciences and Mathematics  
of the Ruperto-Carola University of Heidelberg, Germany  
for the degree of

**doctor rerum naturalium**

presented by

**Dipl.-Phys. Johannes Albrecht**

born in Heidelberg, Germany

Oral examination: July 8<sup>th</sup>, 2009



**Fast Track Reconstruction  
for the High Level Trigger  
of the LHC*b* Experiment**

Referees: Prof. Dr. Ulrich Uwer

Prof. Dr. Johanna Stachel



## Abstract

This work presents an algorithm for fast track reconstruction in the main tracking stations for the lowest level of the LHCb software trigger. True signals of the hardware trigger are confirmed by a track with an efficiency of larger than 95 % within 1 ms. The tracking algorithm improves the momentum resolution of the trigger objects significantly and can thus be used to reduce the trigger rate by a factor of two with almost no loss in efficiency. The trigger sequence based on the fast track reconstruction in the main tracker developed within this thesis is a complimentary approach to the existing vertex detector based trigger sequence. It yields comparable efficiency and retention rates. The new approach significantly improves the overall robustness of the LHCb trigger system. A detailed evaluation of its performance is presented here.

Additionally the complete software trigger for muons has been rewritten and optimized. It now allows to trigger events without affecting the  $B$  meson lifetime dependent acceptance nor the angular dependent acceptance of its decay products. This is crucial for the analysis of the  $CP$  violation in the decay  $B_s \rightarrow J/\psi\phi$ , one of the key measurements of the LHCb physics program.

## Kurzfassung

In der vorliegenden Arbeit werden Algorithmen für die schnelle Spurrekonstruktion in den Hauptspurkammern des LHCb Detektors für die niedrigste Stufe des Software-Triggers vorgestellt. Signalereignisse, welche vom Hardware-Trigger selektiert wurden, werden innerhalb von 1 ms mit einer Effizienz von über 95 % bestätigt. Der Spurfundungsalgorithmus verbessert die Impulsauflösung signifikant, daher kann fast ohne Effizienzverlust die Triggerrate halbiert werden. Die in dieser Arbeit entwickelte Triggersequenz, basierend auf der schnellen Spurrekonstruktion in den Hauptspurkammern, ist ein komplementärer Ansatz zur existierenden Triggersequenz, welche auf dem Vertex-Detektor basiert. Die hier präsentierte Sequenz zeigt vergleichbare Signaleffizienzen und Untergrundraten. Der neue Ansatz erhöht daher deutlich die Stabilität des Triggersystems von LHCb. Es wird eine detaillierte Auswertung seiner Leistung präsentiert.

Weiterhin wurde der gesamte Software-Trigger für Myonen derart umgeschrieben und optimiert, dass es nun möglich ist,  $B$ -Mesonen zu selektieren, ohne die Lebensdauer und Zerfallswinkel abhängige Akzeptanz zu modifizieren. Dies ist eine wesentliche Voraussetzung der Analyse von  $CP$ -Verletzung im Kanal  $B_s \rightarrow J/\psi\phi$ , eine der Schlüsselanalysen im Physikprogramm des LHCb Experimentes.



# Contents

<b>Introduction</b>	<b>2</b>
<b>1 Theoretical background</b>	<b>3</b>
1.1 The Standard Model of particle physics . . . . .	3
1.1.1 Quark mixing . . . . .	5
1.2 CP Violation in the Standard Model . . . . .	8
1.2.1 Mixing of neutral $B$ mesons . . . . .	9
1.2.2 $CP$ violation in the $B$ meson system . . . . .	11
1.3 Signatures of New Physics in the beauty system . . . . .	11
1.3.1 CP violation in the $B_s$ system . . . . .	12
1.3.2 Rare decays . . . . .	14
1.3.3 Electroweak penguin decays . . . . .	16
1.4 $B$ production at the LHC . . . . .	18
<b>2 The LHC<b><i>b</i></b> experiment</b>	<b>21</b>
2.1 Tracking System . . . . .	23
2.1.1 Vertex Locator . . . . .	23
2.1.2 Trigger Tracker . . . . .	25
2.1.3 Inner Tracker . . . . .	26
2.1.4 Outer Tracker . . . . .	27
2.1.5 Tracking strategy and performance . . . . .	28
2.1.6 Fast momentum estimation . . . . .	31
2.2 Calorimeter system . . . . .	31
2.2.1 Preshower and Scintillating Pad Detector . . . . .	32
2.2.2 Electromagnetic Calorimeter . . . . .	33
2.2.3 Hadronic Calorimeter . . . . .	34
2.3 Muon system . . . . .	34
2.3.1 Standalone muon track reconstruction . . . . .	36
2.4 Monte Carlo simulation . . . . .	36
2.4.1 Framework and applications . . . . .	36
2.4.2 Generated events . . . . .	37
<b>3 The LHC<b><i>b</i></b> trigger system</b>	<b>39</b>
3.1 The L0 hardware trigger . . . . .	39
3.1.1 The hardware muon trigger . . . . .	39
3.1.2 The hardware calorimeter trigger . . . . .	40

3.1.3	Global event veto . . . . .	42
3.2	Online farm . . . . .	43
3.3	High level software trigger . . . . .	44
3.3.1	First software trigger level: Confirmation of the hardware trigger . . . . .	45
3.3.2	Second software trigger level: Final selections . . . . .	49
<b>4</b>	<b>Fast track reconstruction</b>	<b>53</b>
4.1	Seed preparation . . . . .	53
4.1.1	Muons . . . . .	54
4.1.2	Electrons and photons . . . . .	57
4.1.3	Hadrons . . . . .	59
4.1.4	Seed extrapolation . . . . .	60
4.2	Hit preparation in the search window . . . . .	61
4.3	Track finding . . . . .	63
4.3.1	Principles of T-Station track finding . . . . .	63
4.3.2	Algorithm tuning for trigger tracking . . . . .	65
4.3.3	Performance comparison of trigger tracking algorithms . . . . .	67
4.4	Performance . . . . .	68
4.5	Summary . . . . .	71
<b>5</b>	<b>Track based software trigger</b>	<b>73</b>
5.1	The fast kalman filter based track fit . . . . .	73
5.1.1	Full track fit . . . . .	73
5.1.2	Simplified track fit . . . . .	75
5.2	Hadron selection in the first level of the software trigger . . . . .	76
5.2.1	Single hadron selection using the tracker . . . . .	77
5.2.2	Fast track fit in the hadron alley . . . . .	81
5.2.3	Summary of the hadron alley . . . . .	81
5.3	Muon selection in the first level of the software trigger . . . . .	82
5.3.1	Single muon selection . . . . .	84
5.3.2	Dimuon recovery selection . . . . .	86
5.3.3	Fast track fit in the muon alley . . . . .	88
5.3.4	Summary of the muon alley . . . . .	89
5.4	Inclusive dimuon selection for the second software trigger level . . . . .	90
5.4.1	Lifetime unbiased dimuon selection . . . . .	91
5.4.2	Lifetime biased dimuon selection . . . . .	93
5.4.3	Inclusive dimuon summary . . . . .	93
5.5	Trigger performance summary . . . . .	94
5.5.1	Hadronic channels . . . . .	94
5.5.2	Muonic channels . . . . .	95
5.5.3	Electromagnetic channels . . . . .	95

---

<b>6</b>	<b>Potential of LHC<b><i>b</i></b> to measure New Physics in B decays</b>	<b>97</b>
6.1	<i>CP</i> violation in the $B_s$ system . . . . .	97
6.1.1	Selection of $B_s \rightarrow J/\psi\phi$ events and trigger strategy . . . . .	99
6.1.2	Kinematic distributions of signal and control channels . . . . .	101
6.1.3	Proper time distribution . . . . .	101
6.1.4	Angular acceptances . . . . .	104
6.1.5	Extraction of the <i>CP</i> violating phase . . . . .	106
6.2	Rare Decays: $B_s \rightarrow \mu^+\mu^-$ . . . . .	109
6.2.1	Event selection and trigger strategy . . . . .	109
6.2.2	Sensitivity . . . . .	110
6.3	Radiative penguin transitions: $B_d \rightarrow K^{*0}\mu^+\mu^-$ . . . . .	111
6.3.1	Event selection and trigger strategy . . . . .	111
6.3.2	Sensitivity . . . . .	113
<b>7</b>	<b>Summary and conclusion</b>	<b>115</b>
	<b>List of Figures</b>	<b>117</b>
	<b>List of Tables</b>	<b>119</b>
	<b>Bibliography</b>	<b>121</b>



# Introduction

The standard model of particle physics (SM), developed in the 1960's [1–3] provides an excellent description of the results of all up to date collider experiments. However, the Standard Model cannot explain the following cosmological observations:

- **Dark matter** The existence of dark matter which is observed in cosmological experiments cannot be explained in the Standard Model [4].
- **Baryon asymmetry** The origin of the baryon asymmetry, i. e., the excess of matter over antimatter in the universe is not explained by the the Standard Model [5–7].

The Large Hadron Collider (LHC) at CERN in Geneva, a proton-proton collider with a center of mass energy of 14 TeV, will start in autumn 2009. Its aim is to find first evidence for a physics theory beyond the Standard Model (“New Physics”) which would solve these problems, e. g., by discovering supersymmetric particles. The LHC furthermore aims to find the Higgs boson, the last non confirmed building block of the Standard Model. The signatures of New Physics can be measured with two complementary approaches: direct searches for real particles, or searches for indirect effects by virtual particles which appear in loop processes. The first is covered by the two multi-purpose experiments ATLAS and CMS. The latter approach is followed by the Large Hadron Collider beauty experiment (LHC***b***).

The precise measurement of  $CP$  violation is considered to be one of the keys to discover new physics, see for example references [8, 9].  $CP$  violation is the violation of the combined symmetry operation of particle-antiparticle transformation (charge inversion,  $C$ ) and space inversion (parity,  $P$ ). Almost any extension of the Standard Model provides new sources of  $CP$  violation. The supersymmetric extension of the Standard Model predicts 44 new independent phases, most of them leading to  $CP$  violation [8].

LHC***b*** is a dedicated  $B$  physics experiment, it profits from the high production cross section of  $B$  mesons at 14 TeV. During regular running of the LHC, about 100 000 pairs of beauty mesons per second are created in the LHC***b*** experiment. In a year of running, this corresponds to  $10^{12}$   $B\bar{B}$  pairs. This very large sample allows to access very rare processes, down to  $B$  decay branching ratios of  $10^{-9}$ .

One of the main challenges of physics at high-energy hadron colliders is the harsh hadronic environment of proton-proton collisions. The  $B$  mesons studied in LHC***b*** decay into up to five stable particles. Additionally to these, about 50 other particles from the underlying event are measured. Another challenge is the high interaction rate: The

proton bunches at the LHC cross with a frequency of 40 MHz, producing a flow of data in the LHCb detector corresponding to about 500 Gbytes/s. This enormous amount of data cannot be saved directly but has to be filtered in real time to select interesting  $B$  decays. This online event filter, called trigger, is one of the key components of the LHCb experiment. The trigger selection is based on generic signatures of the  $B$  decay properties:

- The  $B$  meson invariant mass of more than 5 GeV results to transverse momenta to the decay products which are on average larger than the ones of background events.
- The relatively large lifetime of the  $B$  meson leads at the LHC to an average flight length of about 1 cm. The background can therefore be separated from the signal by requiring a separated secondary vertex.

Based on these signatures, the LHCb trigger system reduces the rate from 40 MHz to 2 kHz, the rate at which data is written to permanent storage. This is done in a two step procedure, the first is implemented in custom made hardware and the second is a software application running on a CPU farm.

In this thesis, the use of the main tracking stations in the first filter stage of the software trigger has been established. An algorithm has been developed to reconstruct tracks in a limited search window to confirm signals from the hardware trigger such as calorimeter clusters or hits in the muon chambers. The pattern recognition algorithms used for this need to be extremely fast and robust, as they are executed at the software trigger input rate of 1 MHz. The measurements from the main tracker allow a precise momentum estimate of the track which can be used for the trigger selection. Furthermore, a reconstructed track which matches to the hardware trigger seed reduces the rate of fake trigger candidates. The developed algorithm allows to set up a trigger sequence which is complimentary to the existing sequence based on the vertex detector. The implementation and optimization in the software trigger selection for hadrons and muons is presented.

One of the measurements which is considered to have a high sensitivity to physics beyond the Standard Model is the measurement of the  $CP$  violating phase  $\Phi_s$  in the interference of mixing and decay in the channel  $B_s \rightarrow J/\psi\phi$ . The measurement of  $CP$  violation for this channel is complicated by the fact that the final state is an admixture of different relative angular momenta and thus different  $CP$  eigenvalues. To disentangle them, a time dependent angular analysis is done. A crucial requirement of the analysis is that the acceptance of the  $B$  meson lifetime and the angular distribution of its decay products is well understood. The trigger selections developed in this thesis are optimized to modify these acceptances as little as possible.

# Chapter 1

## Theoretical background

This chapter briefly introduces the Standard Model of Particle Physics and the mechanism of quark mixing. It then describes  $CP$  violation in the system of mesons which contain beauty quarks (“ $B$  mesons”), followed by a discussion of the prime signatures of potential physics beyond the Standard Model (“New Physics”) in the  $B$  system. This chapter finishes with a description of the  $B$  meson production properties expected at the LHC.

### 1.1 The Standard Model of particle physics

The *Standard Model of Particle Physics* summarizes today’s knowledge of fundamental particles and their interactions [10–12]. The Standard Model consists of two types of elementary particles: fermions, which have half-integer spin, and bosons, which have integer spin. The fermions in the Standard Model are quarks and leptons, the building blocks of matter. The bosons are the force-carriers, which mediate the interaction between the particles. The Standard Model accommodates the electromagnetic, the strong, and the weak force. The corresponding bosons and coupling constants are listed in Table 1.1. Three of the four fundamental bosons have been observed, the Higgs boson has not yet been discovered. The given limit on the mass is the 95% CL limit obtained from direct searches at the LEP experiments [13]. The fourth and weakest force in nature, gravitation, is not included in the Standard Model.

Both quarks and leptons are divided into three generations with increasing mass, each generation contains again two types of fermions. For the quarks this results in six flavors: up, down, strange, charm, beauty, and top. For the leptons, each generation contains a charged lepton and a neutral neutrino. They can be of type electron, muon, or tau. The Standard Model fermions are summarized in Table 1.2. All listed fermions and their antiparticles have been observed. According to  $CPT$  invariance, which is a fundamental invariance in quantum gauge theory, particles and antiparticles must have equal masses and decay times.

The theory of the strong force is Quantum Chromodynamics (QCD), it acts on a quantum number of the quark called color. The quarks listed in Table 1.2 come in three different colors: red, green, and blue and the corresponding anticolors: antired, antigreen, and antiblue. The color of a quark can change by exchanging a gluon with another quark. Quarks can only occur in bound states, because QCD only allows color

**Table 1.1:** Boson content of the Standard Model and the approximate particle mass and relative strength of the corresponding interaction [14].

interaction	(gauge) bosons	mass	relative strength
Strong	gluons ( $g_1, \dots, g_8$ )	0	$\alpha_s \sim \mathcal{O}(1)$
Electromagnetic	photon ( $\gamma$ )	0	$\alpha \sim \mathcal{O}(10^{-2})$
Weak	$W^\pm$	80 GeV	$\alpha_W \sim \mathcal{O}(10^{-6})$
	$Z^0$	91 GeV	
—	Higgs boson ( $H^0$ )	> 114 GeV	—

**Table 1.2:** Fermion content of the Standard Model: quarks and leptons. The approximate particle masses are given in parenthesis (from [14]). The limits on the neutrino masses are obtained by tritium decay measurements [15]. For the light quarks,  $u$ ,  $d$ ,  $s$ , these are *current-quark* masses at a scale  $\mu \approx 2$  GeV. The  $c$  and  $b$  quark masses are *running* masses in the  $\overline{\text{MS}}$  scheme, while the  $t$  mass is obtained from the direct observation of top events.

	Type	1 <sup>st</sup> generation	2 <sup>nd</sup> generation	3 <sup>rd</sup> generation
Leptons	neutrino	$\nu_e$ (< 2 eV)	$\nu_\mu$ (< 2 eV)	$\nu_\tau$ (< 2 eV)
	lepton	$e$ (511 keV)	$\mu$ (106 MeV)	$\tau$ (1.78 GeV)
Quarks	up	$u$ (2 MeV)	$c$ (1.25 GeV)	$t$ (174 GeV)
	down	$d$ (5 MeV)	$s$ (95 MeV)	$b$ (4.2 GeV)

neutral hadrons (confinement). There are two types of hadrons: baryons and mesons. Baryons are built from three quarks (or three antiquarks), each having a different color quantum number. In contrast to baryons, mesons are built from a quark and an antiquark of opposite color. This thesis focuses on the physics of mesons containing either a  $b$  quark or an anti- $b$  quark:  $B$  mesons. An important aspect of the strong interaction is that quarks are always created in quark antiquark pairs of the same flavor. This also implies that  $B$  hadrons are produced in pairs, where one  $B$ -hadron contains a  $b$  quark and the other an anti- $b$  quark, denoted by  $\bar{b}$ .

The electromagnetic force acts on all charged particles through the exchange of massless photons, the weak force acts on all all fermions through the exchange of a massive  $W^\pm$  or  $Z^0$  boson.  $W^\pm$  bosons change the quark flavor from *up-type* to *down-type* and vice versa. They are referred to as the charged current of the weak interaction. In contrast, the neutral current, mediated by a  $Z^0$  boson, cannot change flavor. The absence of any flavor changing neutral current is described by the Glashow-Iliopoulos-Maiani (GIM) mechanism [16].

Table 1.3 summarizes the electroweak flavor quantum numbers of leptons and quarks. In the original Standard Model, neutrinos are massless and thus only interact weakly.

**Table 1.3:** Weak flavor quantum numbers of leptons and quarks. Weak isospin doublets are given in brackets. The weak eigenstates  $d'$ ,  $s'$  and  $b'$  are related to the mass eigenstates  $d$ ,  $s$  and  $b$  via the  $CKM$  matrix, Equation 1.1. The symbol  $T$  denotes the weak isospin,  $T_3$  is its third component,  $Y = Q - T_3$  the weak hypercharge, where  $Q$  is the electric charge in units of the elementary charge  $e$ . The subscripts L and R indicate left- and right-handed states. Table from Reference [11].

generation			$T$	$T_3$	$Y$	$Q$
$\begin{pmatrix} \nu_{eL} \\ e_L \end{pmatrix}$	$\begin{pmatrix} \nu_{\mu L} \\ \mu_L \end{pmatrix}$	$\begin{pmatrix} \nu_{\tau L} \\ \tau_L \end{pmatrix}$	$1/2$	$+1/2$ $-1/2$	$-1/2$ $-1/2$	$0$ $-1$
$e_R$	$\mu_R$	$\tau_R$	$0$	$0$	$-1$	$-1$
$\begin{pmatrix} u_L \\ d'_L \end{pmatrix}$	$\begin{pmatrix} c_L \\ s'_L \end{pmatrix}$	$\begin{pmatrix} t_L \\ b'_L \end{pmatrix}$	$1/2$	$+1/2$ $-1/2$	$+1/6$ $+1/6$	$+2/3$ $-1/3$
$u_R$	$c_R$	$t_R$	$0$	$0$	$+2/3$	$+2/3$
$d_R$	$s_R$	$b_R$	$0$	$0$	$-1/3$	$-1/3$

Since right-handed neutrinos would be isospin singlets, they would not interact at all and hence do not exist in the limit of massless neutrinos. The measurement of neutrino oscillations is a clear evidence that neutrinos have finite masses [11, 14].

### 1.1.1 Quark mixing

In the standard model, the electromagnetic and weak interaction are unified into a single electroweak interaction [1–3]. This unification is made at the cost of a new and yet unobserved particle: the Higgs boson. The higgs field is responsible for a spontaneously broken symmetry between the massive weak bosons and the massless photon. After the symmetry breaking, also the quarks and leptons obtain their mass from the Yukawa coupling to the Higgs field. However, the resulting mass eigenstates are not the same as the eigenstates of the weak interaction. In order to describe the necessary base transformation, the Cabibbo-Kobayashi-Maskawa ( $CKM$ ) quark mixing matrix was introduced [17, 18]. The base transformation of all quark states can be described by a rotation of the down type quarks. The transformation between the mass ( $d, s, b$ ) and the weak eigenstates ( $d', s', b'$ ) can be defined as

$$\begin{pmatrix} d' \\ s' \\ b' \end{pmatrix} = \mathbf{V}_{CKM} \begin{pmatrix} d \\ s \\ b \end{pmatrix}, \quad (1.1)$$

where  $\mathbf{V}_{\text{CKM}}$  is the quark mixing matrix. It can be defined as

$$\mathbf{V}_{\text{CKM}} = \begin{pmatrix} V_{ud} & V_{us} & V_{ub} \\ V_{cd} & V_{cs} & V_{cb} \\ V_{td} & V_{ts} & V_{tb} \end{pmatrix}. \quad (1.2)$$

The complex matrix elements represent 18 parameters. By definition, the *CKM* matrix is unitary,  $\mathbf{V}_{\text{CKM}}(\mathbf{V}_{\text{CKM}})^\dagger = \mathbf{1}$ , which results in the following unitarity conditions:

$$\sum_{k=1}^3 V_{ki}^* V_{kj} = \delta_{ij}, \quad (1.3)$$

with  $\delta_{ij} = 1$  if  $i = j$  and otherwise  $\delta_{ij} = 0$ . The unitarity reflects the fact that an up-type quark  $q_u$  must transform into a down-type quark  $q_d$  if a charged current interaction occurs. The unitarity conditions leave nine free parameters for the nine complex matrix elements  $V_{ij}$ . Five of these parameters can be absorbed by redefining the quark fields [11]. The four remaining parameters are three real rotation angles and one *CP*-violating phase  $\delta$ . This *Kobayashi-Maskawa phase* is responsible for all *CP*-violating phenomena in flavor-changing processes within the Standard Model [11, 14, 18]. The four parameters are free parameters of the Standard Model and have to be determined experimentally. A standard parameterization of the quark mixing matrix is the *Wolfenstein Parameterization* [14, 19] which shows its hierarchical structure:

$$\mathbf{V}_{\text{CKM}} = \begin{pmatrix} 1 - \frac{\lambda^2}{2} & \lambda & A\lambda^3(\rho - i\eta) \\ -\lambda & 1 - \frac{\lambda^2}{2} & A\lambda^2 \\ A\lambda^3(1 - \rho - i\eta) & -A\lambda^2 & 1 \end{pmatrix} + \mathcal{O}(\lambda^4). \quad (1.4)$$

The parameters of the matrix are defined as:

$$\begin{aligned} \lambda &= \frac{|V_{us}|}{\sqrt{|V_{ud}|^2 + |V_{us}|^2}}, \\ A\lambda^2 &= \lambda \left| \frac{V_{cb}}{V_{us}} \right|, \\ A\lambda^3(\rho + i\eta) &= V_{ub}^*. \end{aligned} \quad (1.5)$$

Experimentally they are determined to be [14]:

$$\begin{aligned} \lambda &\approx 0.22, \\ A &\approx 0.82. \end{aligned} \quad (1.6)$$

The constraint that the *CKM* matrix is unitary can be visualized as triangles in the complex plane. In total, six of these triangles can be constructed. The area within each triangle is the same for all six triangles and is a direct measure for the amount of *CP* violation in the Standard Model [20]. Only two have sides at the same orders, the others are squashed. One of the non-degenerate triangles is defined by the unitary condition:

$$V_{ud}V_{ub}^* + V_{cd}V_{cb}^* + V_{td}V_{tb}^* = 0, \quad (1.7)$$

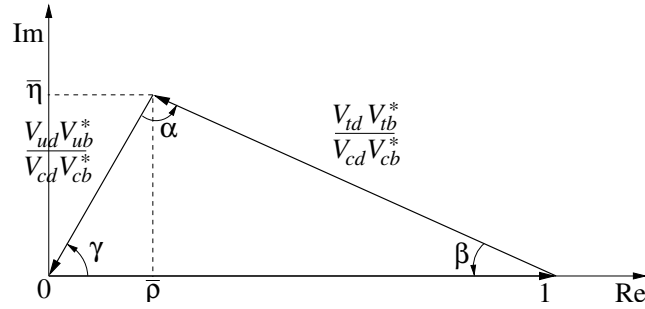


**Figure 1.1:** Scheme of the unitarity triangle in the complex plane. (Figure from [21].)

which is visualized in Figure 1.1. The three angles in Figure 1.1 are defined as counter-clockwise rotations of

$$\alpha = \arg\left(-\frac{V_{td}V_{tb}^*}{V_{ud}V_{ub}^*}\right), \quad \beta = \arg\left(-\frac{V_{cd}V_{cb}^*}{V_{td}V_{tb}^*}\right), \quad \gamma = \arg\left(-\frac{V_{ud}V_{ub}^*}{V_{cd}V_{cb}^*}\right). \quad (1.8)$$

One of the almost degenerate unitarity triangles is the  $b - s$  unitary triangle, corresponding to the relation:

$$V_{us}V_{ub}^* + V_{cs}V_{cb}^* + V_{ts}V_{tb}^* = 0. \quad (1.9)$$

The angle  $\beta_s$  is defined to be the (positive) smaller angle, corresponding to the relation:

$$\beta_s = \arg\left(-\frac{V_{ts}V_{tb}^*}{V_{cs}V_{cb}^*}\right), \quad (1.10)$$

which can be written with the Wolfenstein parameterization as:

$$\beta_s = \eta\lambda^2 + \mathcal{O}(\lambda^4). \quad (1.11)$$

The traditional goal of  $B$ -physics is to find out whether the  $CKM$  matrix describes all flavor changing interactions. Many extensions to the Standard Model predict new effects in flavor physics which may be observable by measuring ( $CP$ -violating) decays of  $B$  mesons. Many measurements have been performed to over-constrain the  $CKM$  matrix. Especially, the measurements with a clean theoretical (i.e., model-independent) interpretation determine the accuracy to which the Standard Model is tested. An accurate knowledge of the  $CKM$  matrix might give sensitivity to New Physics. The current status of all these measurements is summarized in Figure 1.2. Currently, all measurements confirm that the  $CKM$  mechanism describes the observed flavor changing interactions.

A significant constraint from a direct measurement to the  $CKM$  angle  $\gamma$  is missing up to now, see the large brown uncertainty band in Figure 1.2. The precise measurement of  $\gamma$  will be one of the central goals of the  $LHCb$  experiment. Another system which has not yet been precisely measured is the  $B_s$  system, a detailed discussion of this system can be found in the following sections.

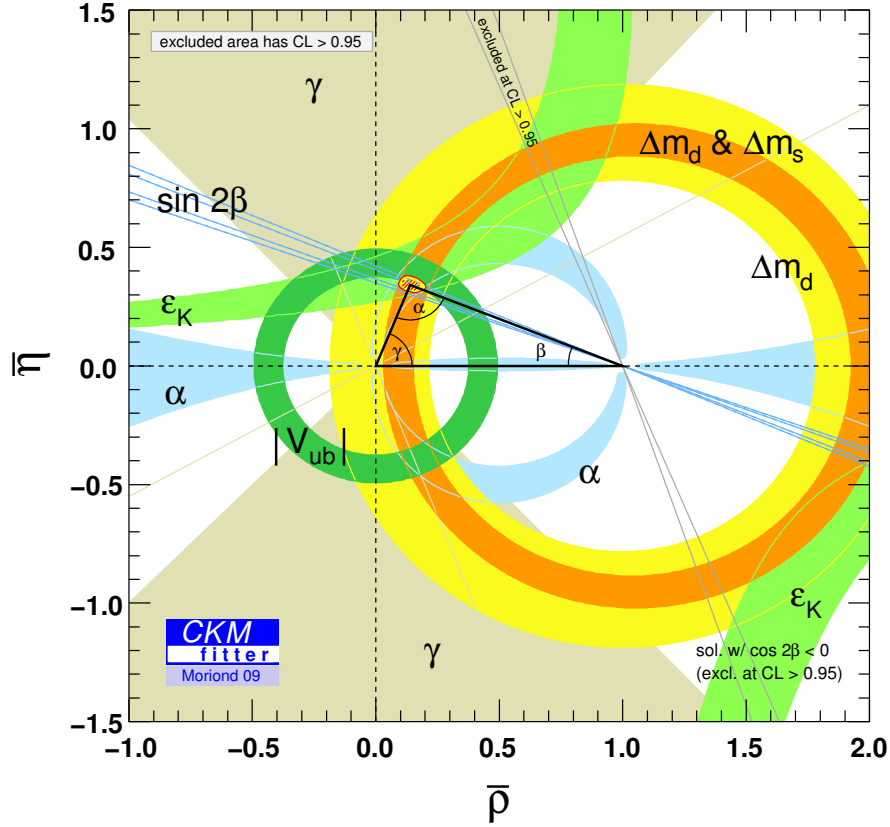


**Figure 1.2:** Global fit of all measurements contributing to  $V_{\text{CKM}}$ . The red hashed region of the global combination corresponds to 68% confidence level. (Figure from [22].)

## 1.2 CP Violation in the Standard Model

In this section, the theoretical context of the measurements of  $CP$ -asymmetries is given. It is, however, not intended to give a full theoretical description, more detailed discussions can for example be found in the following textbooks [23, 24].  $CP$  violation has been observed in the  $K$  meson and in the  $B$  meson system. Here, only the  $B$  meson system is discussed, which is relevant for  $LHCb$ . There are four types of neutral  $B$  mesons, which have a quark content of:

$$|B_d\rangle = |\bar{b}d\rangle \quad , \quad |\bar{B}_d\rangle = |b\bar{d}\rangle \quad (1.12)$$

$$|B_s\rangle = |\bar{b}s\rangle \quad , \quad |\bar{B}_s\rangle = |b\bar{s}\rangle. \quad (1.13)$$

These are also called the  $B$  flavor eigenstates. The  $B_d$  and  $\bar{B}_d$  as well as  $B_s$  and  $\bar{B}_s$  are antiparticles of each other. According to the  $CPT$  theorem they have the same mass and lifetime. In the remainder of this chapter most equations are written in terms of  $B_s$  and  $\bar{B}_s$ ; they equally hold for  $B_d$  and  $\bar{B}_d$ .

### 1.2.1 Mixing of neutral $B$ mesons

To simplify the notation, only the  $CP$  violation in the  $B_s$  meson system is discussed in the following. The flavor eigenstates  $|B_s\rangle$  and  $|\bar{B}_s\rangle$  transform under  $CP$  like

$$CP|B_s\rangle = -|\bar{B}_s\rangle, \quad (1.14)$$

$$CP|\bar{B}_s\rangle = -|B_s\rangle, \quad (1.15)$$

which leads to the following  $CP$  eigenstates:

$$|B_s^{\text{CP even}}\rangle = \frac{1}{\sqrt{2}} (|B_s\rangle - |\bar{B}_s\rangle) \quad (1.16)$$

$$|B_s^{\text{CP odd}}\rangle = \frac{1}{\sqrt{2}} (|B_s\rangle + |\bar{B}_s\rangle). \quad (1.17)$$

The time development of the flavor eigenstates  $|B_s\rangle$  and  $|\bar{B}_s\rangle$  is governed by the Schrödinger equation

$$i \frac{d}{dt} \begin{pmatrix} B_s \\ \bar{B}_s \end{pmatrix} = (M - \frac{i}{2}\Gamma) \begin{pmatrix} B_s \\ \bar{B}_s \end{pmatrix}, \quad (1.18)$$

where  $M$  and  $\Gamma$  are two hermitian two-by-two matrices. From  $CPT$  symmetry, it follows that  $B_s$  and  $\bar{B}_s$  mesons have equal masses ( $M_{11} = M_{22}$ ) and equal decay times ( $\Gamma_{11} = \Gamma_{22}$ ). The off-diagonal elements satisfy  $M_{12} = M_{21}^*$  and  $\Gamma_{12} = \Gamma_{21}^*$ , they are particularly important in the discussion of mixing and  $CP$  violation.  $M_{12}$  is the dispersive part of the transition amplitude from  $B_s$  to  $\bar{B}_s$ , while  $\Gamma_{12}$  is the absorptive part of that amplitude.

The off-diagonal terms stem from the  $B_s - \bar{B}_s$  mixing diagram shown in figure Figure 1.3. New Physics effects can significantly alter  $M_{12}$  which is short-distance dominated, while they are not expected to have a large effect on  $\Gamma_{12}$  which is mainly caused by tree level decays to common final states of  $B_s$  and  $\bar{B}_s$ .

Diagonalizing the Hamiltonian in Equation 1.18 leads to the mass eigenstates  $|B_L\rangle$  and  $|B_H\rangle$ .

$$B_L = p|B_s\rangle + q|\bar{B}_s\rangle \quad (1.19)$$

$$B_H = p|B_s\rangle - q|\bar{B}_s\rangle \quad (1.20)$$

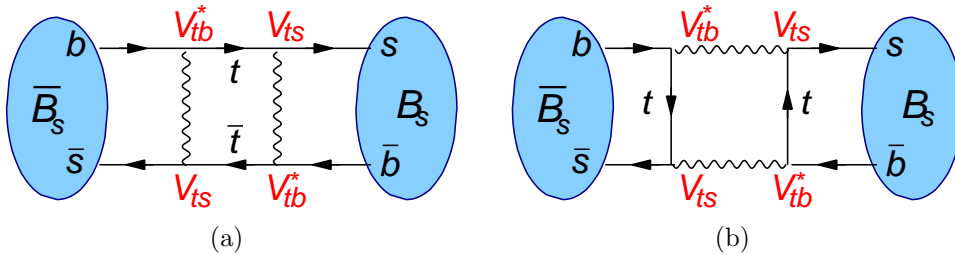


Figure 1.3: Dominant diagrams for  $B_s - \bar{B}_s$  mixing.

with  $|p|^2 + |q|^2 = 1$ . The difference in mass and decay rate is defined as

$$\begin{aligned}\Delta M &= M_H - M_L \\ \Delta\Gamma &= \Gamma_L - \Gamma_H,\end{aligned}$$

such that  $\Delta M$  is positive by definition. The sign of  $\Delta\Gamma$  is determined experimentally. Similarly, the average mass and decay time are

$$\begin{aligned}\Gamma &= \frac{\Gamma_H + \Gamma_L}{2}, \text{ and} \\ M &= \frac{M_L + M_H}{2}.\end{aligned}$$

Solving the for the eigenvalues of Equation 1.18 one finds the relation between the ratio  $q/p$  and the off-diagonal matrix elements,  $M_{12}$  and  $\Gamma_{12}$ :

$$\frac{q}{p} = -\frac{\Delta M + \frac{i}{2}\Delta\Gamma}{2M_{12} - i\Gamma_{12}} = -\frac{2M_{12}^* - i\Gamma_{12}^*}{\Delta M + \frac{i}{2}\Delta\Gamma} \quad (1.21)$$

The amplitudes for a decay in a final state  $f$  are  $A_f = \langle f|B_s\rangle$  and  $\bar{A}_f = \langle f|\bar{B}_s\rangle$ . The weak mixing phase  $\Phi$  is defined as:

$$\Phi = -\text{arg}\left(\frac{q\bar{A}_f}{pA_f}\right), \quad (1.22)$$

If New Physics is assumed to affect only  $M_{12}$  and not  $\Gamma_{12}$ , its contribution to  $\Delta B = 2$  transitions can be parameterized in a model independent manner by introducing the complex factor  $\Delta_s$  [25]:

$$M_{12}^{\text{tot}} = M_{12}^{\text{SM}}\Delta_s = M_{12}^{\text{SM}}|\Delta_s|e^{i\phi_s^\Delta}. \quad (1.23)$$

The phase  $\Phi$  can then be expressed, as a function of its Standard Model value and the New Physics parameter,  $\phi_s^\Delta$ :

$$\Phi = \Phi^{\text{SM}} + \phi_s^\Delta, \quad (1.24)$$

where:

$$\Phi^{\text{SM}} = 2\text{arg}(V_{ts}^*V_{tb}) - 2\text{arg}(V_{cb}V_{cs}^*) + \delta^{\text{Penguins}}. \quad (1.25)$$

When the Standard Model penguins are neglected,  $\delta^{\text{Penguins}} = 0$ , the Standard Model phase becomes:

$$\Phi^{\text{SM}} = -2\beta_s, \quad (1.26)$$

where  $\beta_s$  is defined in Equation 1.10.

### 1.2.2 $CP$ violation in the $B$ meson system

In the  $B$  meson system,  $CP$  violation can appear in the following places:

- **$CP$  violation in mixing** is observed if the oscillation probability of  $B_s \rightarrow \bar{B}_s$  differs from the probability of  $\bar{B}_s \rightarrow B_s$ . This is the case when  $|q/p| \neq 1$ , the  $CP$  eigenstates will differ from the mass eigenstates ( $B_L$  and  $B_H$ ).  $CP$  violation in mixing is predicted to be very small ( $< 10^{-3}$ ) [15] both in the  $B_d$  and the  $B_s$  system. This implies that  $|q/p| \sim 1$  and that  $B_H$  and  $B_L$  are almost exact  $CP$  eigenstates.
- **$CP$  violation in decay** is observed if the amplitude of a  $B_s$  decaying to a final state  $f$  differs from the amplitude of the  $\bar{B}_s$  decaying to the final state  $\bar{f}$ . This is the case when  $|A_f/\bar{A}_{\bar{f}}| \neq 1$ .  $CP$  violation in decay has been observed in the  $B_d$  system by the Belle [26] and BaBar [27] experiments. It has been measured, e. g., in the  $B_d \rightarrow K^+\pi^-$  decay. This  $CP$  violation is caused by large interference between the tree and penguin contributions to the decay.
- **$CP$  violation in the interference between mixing and decay** appears in neutral  $B$  decays when there is a phase difference between  $q/p$  (mixing) and  $\bar{A}_f/A_f$  (decay). The  $CP$  violation in the interference is a large effect in the  $B_d$  and  $B_s$  meson system. This type of  $CP$  violation has been the main focus of experimental investigations.

The  $CP$  violation in the mixing is negligible in both the  $B_d$  and the  $B_s$  system. For decays that are dominated by a single phase, so that the  $CP$  violation in decay is also negligible, a measured  $CP$  asymmetry from the interference between mixing and decay can be cleanly interpreted in terms of purely electroweak parameters.

## 1.3 Signatures of New Physics in the beauty system

This section introduces three of the most promising probes for New Physics in the  $B$  meson system which are accessible at the LHCb experiment. The discussed channels decay to “ $\mu^+\mu^- X$ ” in the final state, the trigger selection developed in Chapter 4 and 5 is written to optimally select these decays. Other key measurements of LHCb, as radiative decays or the precise determination of the  $CKM$  angle  $\gamma$  are not discussed here.

This section first discusses the theoretical background of the analysis to measure the  $CP$  violating phase  $\Phi_s$ . Next, it discusses the rare decay  $B_s \rightarrow \mu^+\mu^-$  whose branching fraction is predicted to be strongly enhanced in many New Physics scenarios. This section concludes with a description of the  $B_d \rightarrow K^{*0}\mu^+\mu^-$  decay whose angular structure has a high sensitivity to New Physics.

### 1.3.1 CP violation in the $B_s$ system

In this section, the quantities necessary to measure  $CP$  violation in the decay mode  $B_s \rightarrow J/\psi(\mu^+\mu^-)\phi(KK)$  are presented. A more complete discussion can be found in [28]. The  $B_s$  meson can decay either directly or first oscillate to a  $\bar{B}_s$ , which then decays. The interference gives sensitivity to the observation of a  $CP$  violating phase  $\Phi_s$ , see Equation 1.22. In the Standard Model, this phase is predicted to be equal to  $-2\beta_s^1$ , with

$$-2\beta_s = -0.0360_{-0.0016}^{+0.0020} \text{ rad} \quad [15]. \quad (1.27)$$

$\Phi_s$  is one of the  $CP$  observables with the smallest theoretical uncertainty in the Standard Model and New Physics could significantly modify this prediction.

The decay  $B_s \rightarrow J/\psi\phi$  is a pseudo-scalar to vector-vector decay. Due to total angular momentum conservation, the observed final state is a superposition of three possible states with relative orbital angular momentum between the vector mesons,  $\ell = 0, 1, 2$ . The  $CP$ -eigenvalue of the observed final state depends on  $\ell$ . An angular analysis allows to disentangle on a statistical basis the  $CP$ -odd and  $CP$ -even components. The extraction of  $\Phi_s$  thus requires a time and angular dependent measurement of the decay rates of  $B_s$  and  $\bar{B}_s$ .

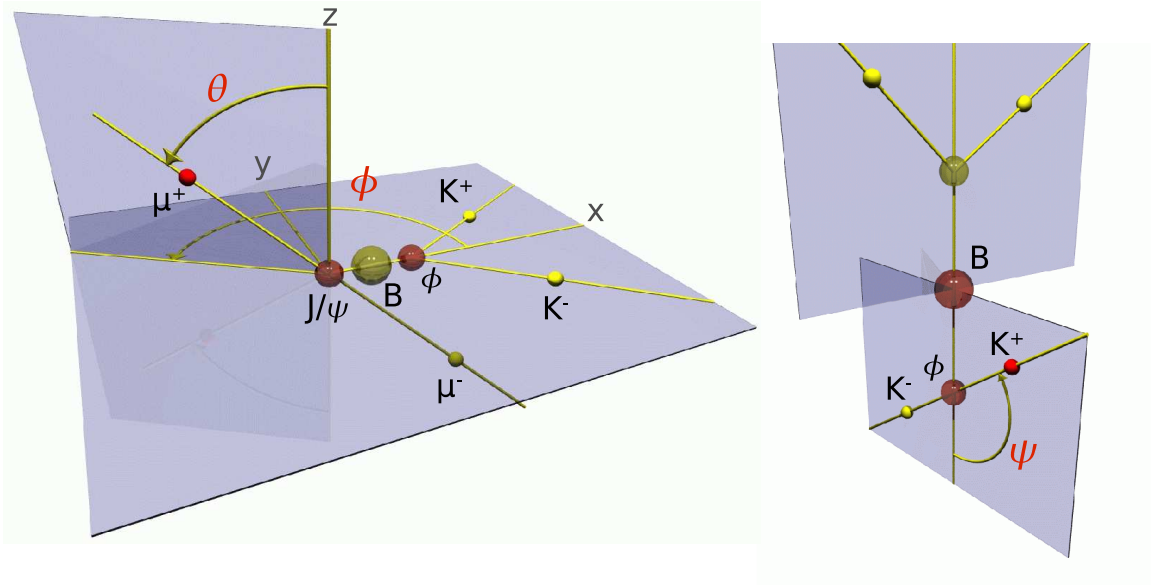


**Figure 1.4:** Definition of transversity angles:  $\theta$  is the angle formed by the positive muon ( $\mu^+$ ) in the  $J/\psi$  rest frame and the  $z$  axis. The angle  $\varphi$  of  $\mu^+$  is the azimuthal angle in the same frame.  $\psi$  is the polar angle between the  $x'$  axis and the decaying  $K^+$  in the  $\phi$  meson rest frame. Figure from [29].

The angular distribution is expressed in the transversity base in which the three angles  $\Omega = \{\theta, \varphi, \psi\}$  are defined. The definition of these angles is given in Figure 1.4 (figure from [29]). In the coordinate system of the  $J/\psi$  rest frame (where the  $\phi$  and  $B_s$  meson move in the  $x$  direction, the  $z$  axis is perpendicular to the decay plane

<sup>1</sup>This assumes that the penguin contributions are negligible.

of  $\phi \rightarrow K^+K^-$ , and  $p_y(K^+) \geq 0$ ), the transversity polar and azimuthal angles ( $\theta, \varphi$ ) describe the direction of the  $\mu^+$ . In the rest frame of the  $\phi$  meson, the angle  $\psi$  is the angle between the  $K^+$  momentum vector and the negative of the  $J/\psi$  momentum vector.

The differential decay rate for the  $B_s \rightarrow J/\psi\phi$  decay is given by the following expression:

$$\frac{d^4\Gamma(B_s \rightarrow J/\psi\phi)}{dt d\cos\theta d\varphi d\cos\psi} \equiv \frac{d^4\Gamma}{dt d\Omega} \propto \sum_{k=1}^6 h_k(t) f_k(\Omega), \quad (1.28)$$

where the components  $h_k$  and  $f_k$  of the sum are defined in Table 1.4. In case of the  $\bar{B}_s$ , the time evolution is given by the conjugate of the functions  $\bar{h}_k(t)$  and the angular terms remain the same. The time dependent coefficients  $h_k(t)$  are functions of the three polarization amplitudes  $A_i(t)$ . A detailed discussion can be found in [29].

**Table 1.4:** Definition of the functions  $h_k(t)$  and  $f_k(\theta, \psi, \varphi)$  as used in Equation 1.28. The functions  $h_k(t)$  are defined in Equations 1.29-1.34.

$k$	$h_k(t)$	$f_k(\theta, \psi, \varphi)$
1	$ A_0(t) ^2$	$2 \cos^2 \psi (1 - \sin^2 \theta \cos^2 \varphi)$
2	$ A_{  }(t) ^2$	$\sin^2 \psi (1 - \sin^2 \theta \sin^2 \varphi)$
3	$ A_{\perp}(t) ^2$	$\sin^2 \psi \sin^2 \theta$
4	$\Im\{A_{  }^*(t)A_{\perp}(t)\}$	$-\sin^2 \psi \sin 2\theta \sin \varphi$
5	$\Re\{A_0^*(t)A_{  }(t)\}$	$\frac{1}{\sqrt{2}} \sin 2\psi \sin^2 \theta \sin 2\varphi$
6	$\Im\{A_0^*(t)A_{\perp}(t)\}$	$\frac{1}{\sqrt{2}} \sin 2\psi \sin 2\theta \cos \varphi$

The time dependent amplitude terms of  $A_i(t)$  are defined as:

$$|A_0(t)|^2 = \frac{|A_0(0)|^2}{2} [(1 + \cos \Phi_s) e^{-\Gamma_L t} + (1 - \cos \Phi_s) e^{-\Gamma_H t} + 2e^{-\Gamma t} \sin(\Delta m t) \sin \Phi_s], \quad (1.29)$$

$$|A_{||}(t)|^2 = \frac{|A_{||}(0)|^2}{2} [(1 + \cos \Phi_s) e^{-\Gamma_L t} + (1 - \cos \Phi_s) e^{-\Gamma_H t} + 2e^{-\Gamma t} \sin(\Delta m t) \sin \Phi_s], \quad (1.30)$$

$$|A_{\perp}(t)|^2 = \frac{|A_{\perp}(0)|^2}{2} [(1 - \cos \Phi_s) e^{-\Gamma_L t} + (1 + \cos \Phi_s) e^{-\Gamma_H t} - 2e^{-\Gamma t} \sin(\Delta m t) \sin \Phi_s], \quad (1.31)$$

$$\begin{aligned} \text{Im}(A_{||}^*(t)A_{\perp}(t)) &= +|A_{||}(0)||A_{\perp}(0)| [e^{-\Gamma t} (\sin \delta_{||} \cos(\Delta m t) - \cos \delta_{||} \sin(\Delta m t) \cos \Phi_s) \\ &\quad - \frac{1}{2} (e^{-\Gamma_H t} - e^{-\Gamma_L t}) \cos \delta_{||} \sin \Phi_s], \end{aligned} \quad (1.32)$$

$$\begin{aligned} \text{Re}(A_0^*(t)A_{||}(t)) &= \frac{1}{2} |A_0(0)||A_{||}(0)| \cos(\delta_{\perp} - \delta_{||}) [(1 + \cos \Phi_s) e^{-\Gamma_L t} + (1 - \cos \Phi_s) e^{-\Gamma_H t} \\ &\quad + 2e^{-\Gamma t} \sin(\Delta m t) \sin \Phi_s], \end{aligned} \quad (1.33)$$

$$\begin{aligned} \text{Im}(A_0^*(t)A_{\perp}(t)) &= +|A_0(0)||A_{\perp}(0)| [e^{-\Gamma t} (\sin \delta_{\perp} \cos(\Delta m t) - \cos \delta_{\perp} \sin(\Delta m t) \cos \Phi_s) \\ &\quad - \frac{1}{2} (e^{-\Gamma_H t} - e^{-\Gamma_L t}) \cos \delta_{\perp} \sin \Phi_s]. \end{aligned} \quad (1.34)$$

Equations 1.29–Equation 1.34 contain information concerning the mass eigenstates which to good approximation are also  $CP$  eigenstates. The angular information separates the  $CP$  eigenstates and thus  $\Gamma_L$  and  $\Gamma_H$  can be determined.

The weak mixing phase  $\Phi_s$  can be extracted from several terms, but for values around the SM value the sensitivity from the  $\cos(\Phi_s)$  terms is poor and all the information comes from the  $\sin(\Phi_s)$  terms. The interference terms the Equations 1.29–1.31 and 1.33 are all multiplied by  $\sin(\Delta m_s t)$  and hence information on  $\Phi_s$  is mainly obtained from observation of the amplitude of the sinusoid in the time distribution. These terms have opposite sign for  $B_s$  and  $\bar{B}_s$  and if untagged events are used then almost complete cancellation of the  $\sin(\Phi_s)$  information occurs. The analysis, therefore, benefits significantly from flavor tagging, where the  $B_s - \bar{B}_s$  oscillation is resolved. If  $\Phi_s$  is large, as indicated by the Tevatron analyses, an untagged analysis also has a good sensitivity.

### Current experimental status

Both the CDF and DØ collaborations have recently presented results of tagged analyses of  $B_s \rightarrow J/\psi\phi$  decays [30–32]. By the end of run 2, assuming an integrated luminosity of  $\mathcal{L} = 9 \text{ fb}^{-1}$  for both CDF and DØ and simple scaling with  $1/\sqrt{\mathcal{L}_{\text{int}}}$ , the combined Tevatron sensitivity to  $\Phi_s$  is expected to be  $\sim 0.13 \text{ rad}$ .

An analysis of the New Physics contribution to the measured phase  $\Phi_s$  can be done in a model independent way (see Equation 1.23 and [25]). This analysis has been done with the newest CDF and DØ data, it is summarized in Figure 1.5. The central value in the complex  $\Delta_s$  plane shows a  $1.9\sigma$  discrepancy with respect to the standard model value. One of the main goals of the LHCb experiment is to clarify if this discrepancy is a statistical fluctuation or a first sign of physics beyond the Standard Model.

### 1.3.2 Rare decays

The rare decay  $B_s \rightarrow \mu^+\mu^-$  implies a flavor changing neutral current transition which is forbidden at tree level in the Standard Model (SM). The lowest order contributions in the SM involve weak penguin loops and weak box diagrams that are  $CKM$  suppressed. An example of a lowest order SM contribution is given in Figure 1.6 (a) (figure from [33]). The box diagram with two  $W$  bosons is suppressed by a factor  $M_W^2/m_t^2$  with respect to the Z-penguin diagram.

Since the  $B_s$  meson is a pseudoscalar, the transition results into an  $\ell = 0$  state, the electromagnetic penguin loop is forbidden. The two leptons are either both right handed or both left handed leading to an additional helicity suppression (proportional to  $m(\mu)/m(B_s)$ ). Thus, the branching fraction expected from the SM are tiny:

$$\mathcal{BR} = (3.86 \pm 0.15) \times \frac{\tau_{B_s}}{1.527 \text{ ps}} \frac{|V_{ts}|^2}{0.0408} \frac{f_{B_s}}{240 \text{ MeV}} \times 10^{-9}, \quad [34] \quad (1.35)$$

with the following quantities factored out:  $\tau_{B_s}$ , the  $B_s$  meson lifetime, the dependence on the decay constant  $f_{B_s}$ , which has sizable theoretical uncertainties, and the  $CKM$  matrix element  $V_{ts}$ , which is well measured [34].

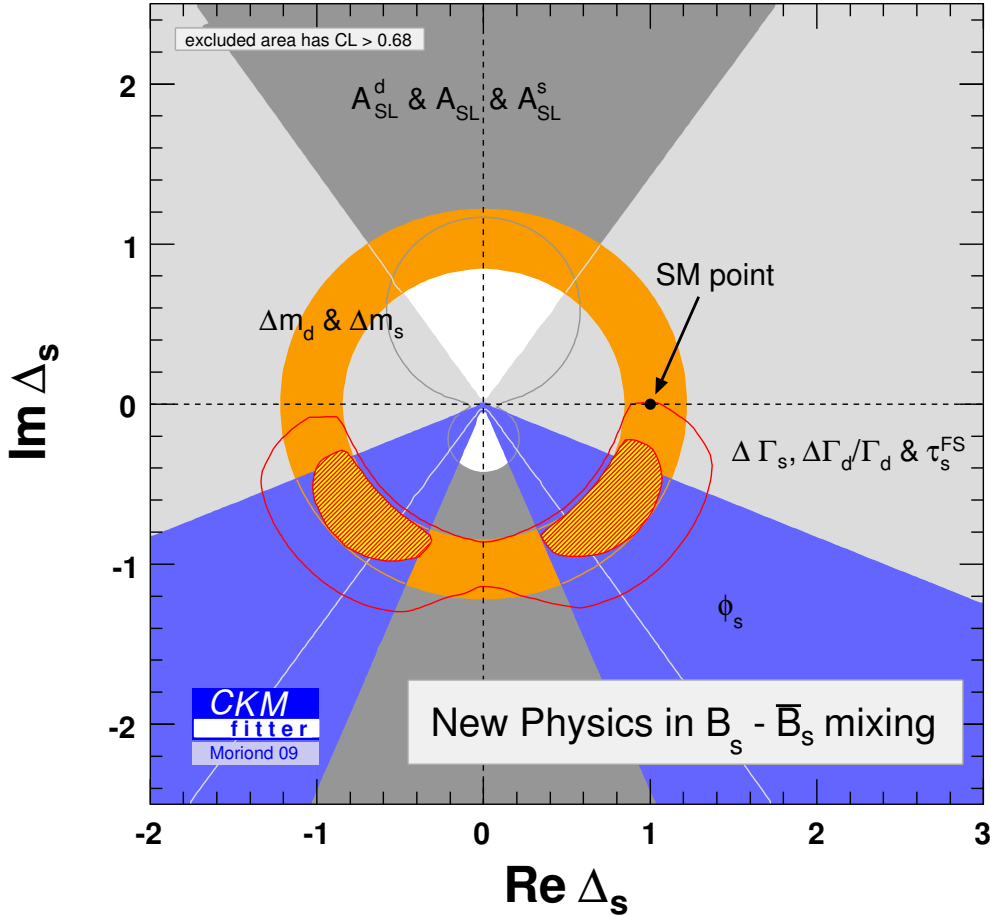


**Figure 1.5:** Constraints on New Physics in the  $(Re(\Delta_s), Im(\Delta_s))$  plane (see Equation 1.23) including the current CDF and  $D\bar{O}$  measurements. The red shaded area corresponds to the  $1\sigma$  contour, the red lines to the  $2\sigma$  contour. A  $1.9\sigma$  deviation is obtained for the two-dimensional SM hypothesis:  $Re(\Delta_s) = 1, Im(\Delta_s) = 0$ . (Figure from [22].)

The helicity suppression factor of  $m_\mu/m_{B_s}$  makes the  $B_s \rightarrow \mu^+\mu^-$  decay sensitive to physics with new scalar or pseudoscalar interactions. This feature makes  $B_s \rightarrow \mu^+\mu^-$  highly interesting to probe models with an extended Higgs sector [35].

The generic Minimal Supersymmetric Model (MSSM) contains many new sources of flavor violation in addition to the Yukawa couplings. Usually, the hypothesis of *Minimal Flavor Violation* (MFV) is introduced to restrict the sources of flavor violation to the Yukawa couplings, as in the Standard Model. In the MFV-MSSM, there are two Higgs doublets which involve flavor changing neutral current Yukawa couplings to the heavy neutral Higgs Bosons  $A^0$  and  $H^0$  [34]. In this model, the  $B_s \rightarrow \mu^+\mu^-$  branching ratio could, in principle, exceed the Standard Model value by a factor of  $10^3$ . It scales as:

$$\mathcal{BR}(B_s \rightarrow \mu^+\mu^-)_{SUSY} \propto \frac{m_{B_s}^2 m_\mu^2 \tan^6(\beta)}{M_{A^0}^4}, \quad [34] \quad (1.36)$$

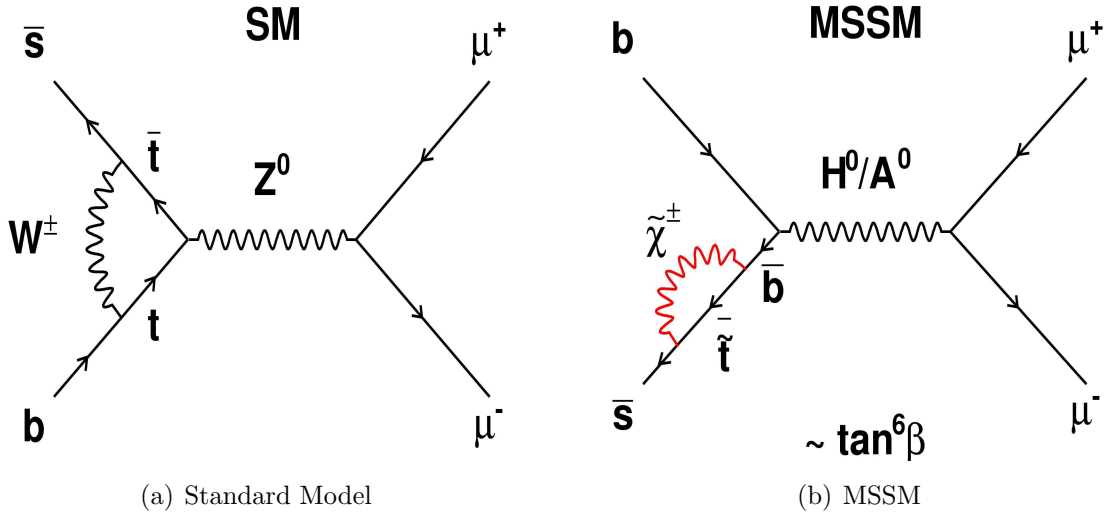


**Figure 1.6:** Examples of Feynman diagrams contributing to the decay  $B_s \rightarrow \mu^+ \mu^-$ . (a) in the Standard Model and (b) in the Minimal Supersymmetric Model (figure from [33]).

where  $\tan(\beta)$  is the ratio of the vacuum expectation values acquired by  $H_u$  and  $H_d$ , the Higgs doublets which couple to up-type and down-type fermions respectively [36]. Thus, the current experimental upper limit from the Tevatron [37, 38], which is larger than the SM branching ratio by a factor of 25, already severely cuts into the parameter space of the MSSM.

Equally interesting as the  $B_s \rightarrow \mu^+ \mu^-$  decay are other  $B_q \rightarrow \ell^+ \ell^-$  decays with  $q = d$  or  $s$  and  $\ell = e, \mu$  or  $\tau$ . Furthermore, these decays are related to each other in a simple way in the Standard model, but not necessarily in models of New Physics. The decay  $B_d \rightarrow \mu^+ \mu^-$  is also well accessible by the LHCb experiment. Its branching ratio,  $\mathcal{BR}(B_d \rightarrow \mu^+ \mu^-)$  is approximately an order of magnitude lower than  $\mathcal{BR}(B_s \rightarrow \mu^+ \mu^-)$  due to the additional  $CKM$  suppression  $\sim V_{td}/V_{ts}$ . Decays to other leptons are experimentally harder accessible than  $B_s \rightarrow \mu^+ \mu^-$  with the clear signature of two muons in the final state.

### 1.3.3 Electroweak penguin decays

In the Standard Model, the electroweak penguin decays  $b \rightarrow s \ell^+ \ell^-$  are only induced at the one loop level which leads to small branching fractions and thus a rather high sensitivity to contributions from physics beyond the Standard Model. The decay  $B_d \rightarrow K^{*0} \mu^+ \mu^-$  is experimentally best accessible due to the clear dimuon signature. The lowest order Feynman diagrams in the Standard Model are shown in Figure 1.7.

A large number of observables can be constructed from the angular distributions of the decay [39]. As main criteria, these observables have to be theoretically clean and experimentally, they have to be measurable with good precision. The differential  $B_d \rightarrow K^{*0} \mu^+ \mu^-$  decay distribution can be written as:

$$\frac{d^4 \Gamma_{B_d}}{dq^2 d\theta_L d\theta_K d\phi} = \frac{9}{32\pi} I(q^2, \theta_L, \theta_K, \phi) \sin \theta_L \sin \theta_K, \quad (1.37)$$

where  $q^2$  is the invariant mass of the muon pair and the three angles  $\theta_L$ ,  $\theta_K$  and  $\phi$  are defined in Figure 1.8. The function  $I(q^2, \theta_L, \theta_K, \phi)$ , which is defined in [40], contains the  $K^{*0}$  spin amplitudes.

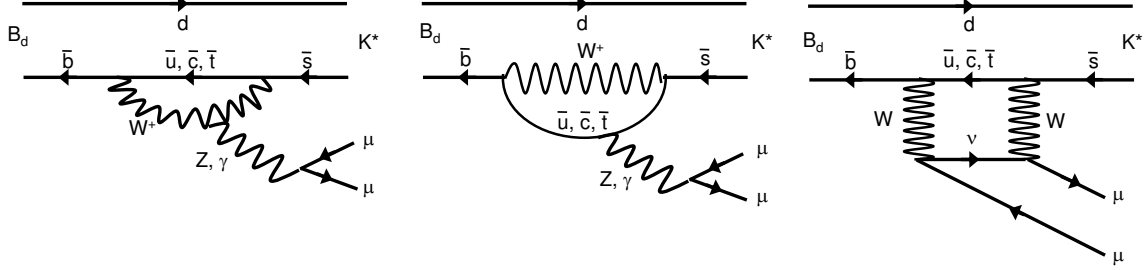


**Figure 1.7:** Lowest order Standard Model Feynman diagrams for the  $B_d \rightarrow K^{*0} \mu^+ \mu^-$  decay. (Figure taken from [41])

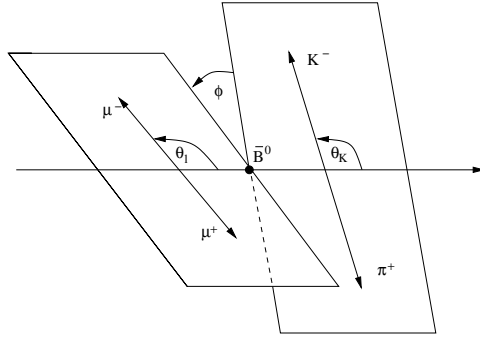


**Figure 1.8:** Angles used to describe the decay  $B_d \rightarrow K^{*0} \mu^+ \mu^-$ .  $\theta_L$  is the angle between the  $\mu^-$  and the  $\bar{B}_d$  in the  $\mu^+ \mu^-$  rest frame.  $\theta_K$  is the angle between the  $K^-$  and the  $\bar{B}_d$  in the  $K^{*0}$  rest frame.  $\phi$  is the angle between the  $\mu^- \mu^+$  and  $K^{*0}$  decay planes. (Figure taken from [41])

The angle  $\theta_L$  between the  $\mu^-$  and the negative flight direction of the  $B_d$  in the dimuon rest frame is particularly important to determine the forward backward asymmetry,  $A_{FB}$ ,

$$A_{FB} = \frac{\int_0^1 \frac{\partial^2 \Gamma}{\partial q^2 \partial \cos \theta_L} d \cos \theta_L - \int_{-1}^0 \frac{\partial^2 \Gamma}{\partial q^2 \partial \cos \theta_L} d \cos \theta_L}{\int_0^1 \frac{\partial^2 \Gamma}{\partial q^2 \partial \cos \theta_L} d \cos \theta_L + \int_{-1}^0 \frac{\partial^2 \Gamma}{\partial q^2 \partial \cos \theta_L} d \cos \theta_L}, \quad (1.38)$$

where,  $\frac{\partial^2 \Gamma}{\partial q^2 \partial \cos \theta_L}$  denotes the partial decay distribution [41]. The point where  $A_{FB}$  crosses the  $q^2$  axis is of particular interest as the main theoretical error coming from the  $B \rightarrow K^{*0}$  form factors cancel in this point at leading order [40].

## 1.4 $B$ production at the LHC

The calculation of the  $B$  meson production cross section in pp-collisions at the LHC is a challenging theoretical problem due to the non-perturbative QCD effects as well as the fact that the proton is a composite particle. The dominant production mechanism for heavy quarks in pp-interactions is the fusion process of gluons and partons ( $gg$  and  $q\bar{q}$ ). Figure 1.9, taken from [42], shows the leading order Feynman diagrams of these processes. The production cross sections for heavy flavor pairs have been calculated up to next-to-leading order [43].

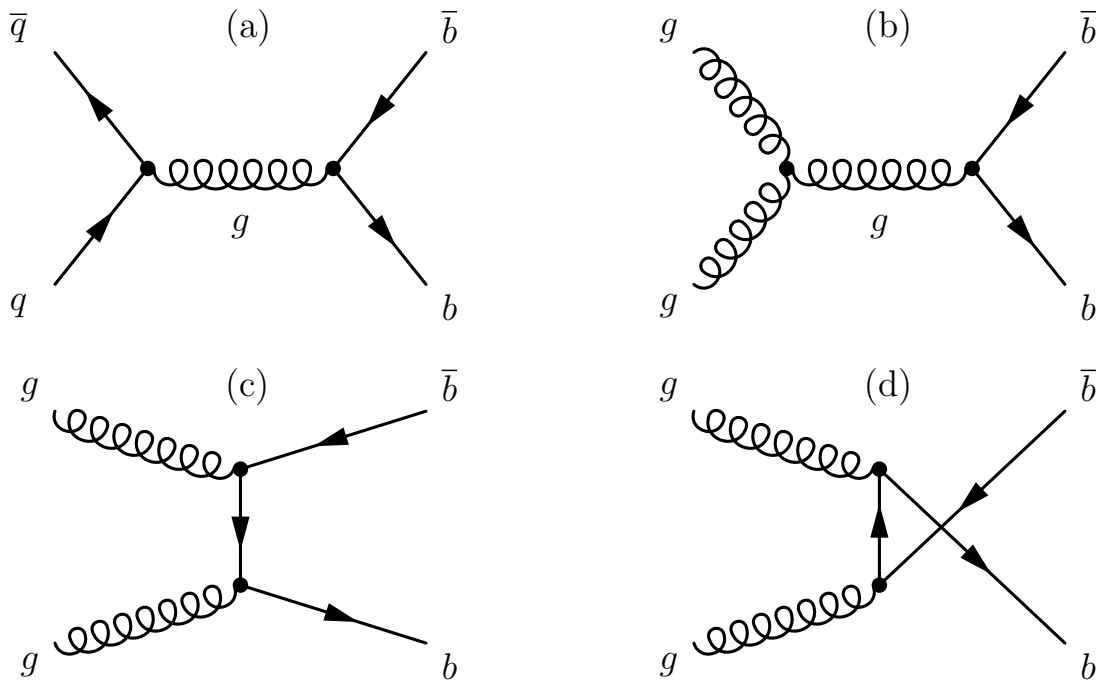


**Figure 1.9:** Leading order contributions to the production of heavy quarks at the LHC. (Figure from [42].)

The cross sections used are summarized in Figure 1.10, taken from [44]. An extrapolation to 14 TeV gives 102.9 mb for the total cross section and  $698 \mu\text{b}$  for the  $b\bar{b}$  production cross section [44]. There are higher order diagrams influencing the  $b\bar{b}$  cross section, whose contribution cannot be neglected. Due to these non negligible corrections, which are not taken into account, the predicted production cross section has large uncertainties [44]. Due to the large uncertainties, LHCb uses the conservative convention:

$$\sigma_{b\bar{b}} = 500 \mu\text{b} \quad (1.39)$$

to estimate event yields. The total number of inelastic collisions over a given period of

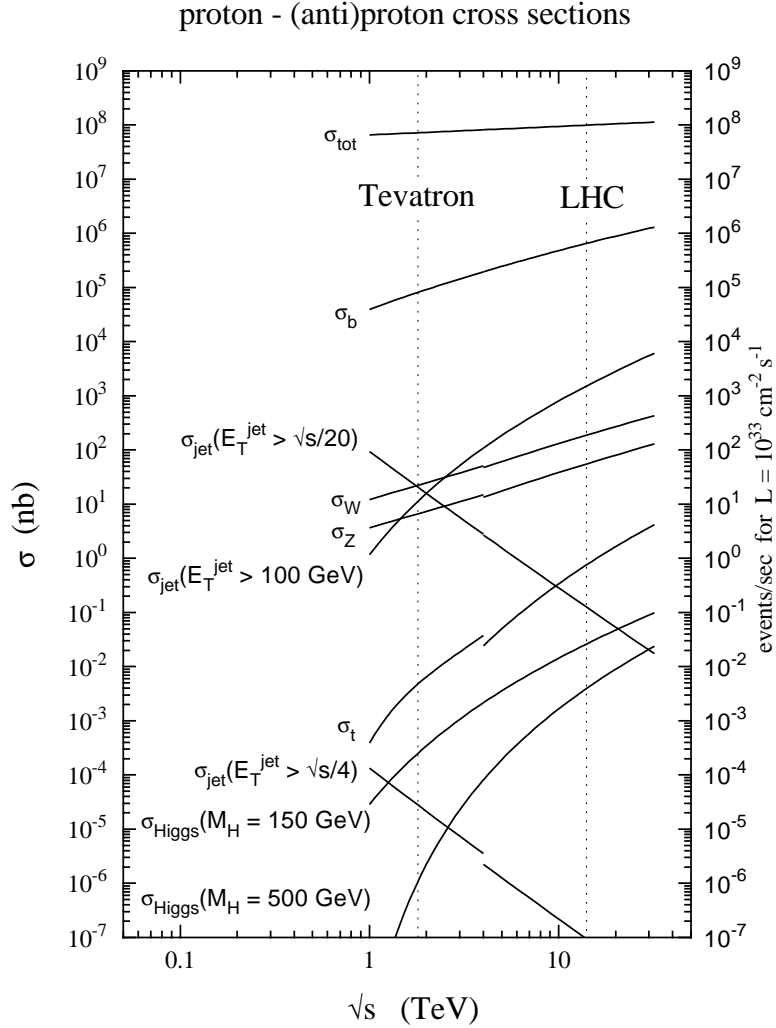


**Figure 1.10:** Cross sections for hard scattering versus  $\sqrt{s}$ . At  $\sqrt{s} = 14 \text{ TeV}$ , the cross sections are:  $\sigma_{tot} = 102.9 \text{ mb}$  and  $\sigma_{pp \rightarrow b\bar{b}} = 698 \mu\text{b}$ . The curves for lower values of  $\sqrt{s}$  are for  $p\bar{p}$  collisions, as at the Tevatron, while the curves for higher values of  $\sqrt{s}$  are for  $pp$ -collisions, as at the LHC. Figure taken from [44].

time can be written as

$$N = \sigma_{inel} \int L dt, \quad (1.40)$$

where  $\sigma_{inel}$  is the inelastic cross section and  $L$  is the instantaneous luminosity. In one second of running at the nominal LHCb luminosity of  $2 \cdot 10^{32} \text{ cm}^{-2} \text{ s}^{-1}$ , this gives an expected number of 100 000  $b\bar{b}$  pairs, in one year of running ( $10^7 \text{ s}$ ), this corresponds to  $1 \times 10^{12}$   $b\bar{b}$  pairs. This high  $B$  production rate enables to study  $CP$  violation in channels with low branching fractions ( $10^{-4} - 10^{-9}$ ).

Although the expected number of  $B$  events depends on  $\sigma_{b\bar{b}}$ , the actual value is not important in a precision measurement of the  $CP$  asymmetry. However, the error on the measured asymmetry depends on the number of reconstructed  $B$ -decays. More important, especially for the trigger, is the ratio  $\sigma_{b\bar{b}}/\sigma_{inel}$ , which basically determines

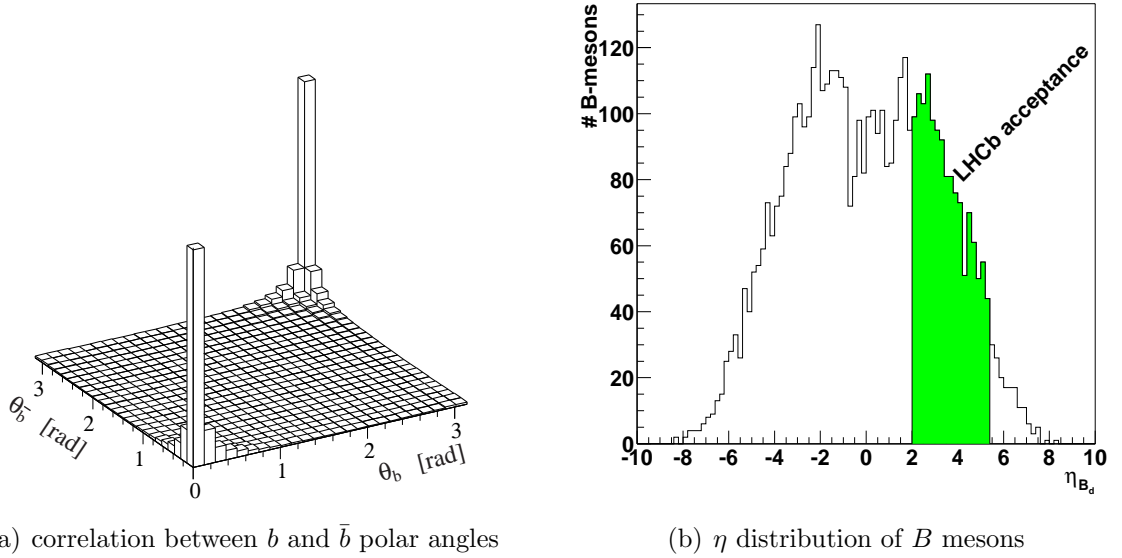


**Figure 1.11:** (a) Simulated correlation between the polar angle  $\theta$  of a  $B$  and an anti  $B$  meson simultaneously produced in an proton proton interaction. (b) Pseudorapidity distribution of the  $B$  mesons. The single arm spectrometer LHCb covers about 25% of the  $\eta$  spectrum of the produced  $B$  mesons. (Figure from [45].)

the ratio of signal over background before selection. About one in every 150 pp-collisions is a  $b\bar{b}$  pair.

Figure 1.11 (a) shows that the production angles of the two produced  $B$  mesons have a strong positive correlation. In addition, the figure shows that the  $B$  meson production is peaked at small (around zero) and high (around  $\pi$ ) polar angles, i. e., along the beam axis. The fact that both  $B$  mesons are produced in the same forward region has led to the single arm forward geometry of the LHCb spectrometer, see Chapter 2.

The pseudo-rapidity ( $\eta$ ) of the  $B$  mesons is defined as

$$\eta = -\log\left(\tan\frac{\theta}{2}\right), \quad (1.41)$$

where  $\theta$  is the polar angle. In Figure 1.11 (b),  $\eta$  is shown for the generated  $B$  mesons which are produced in 14 TeV collisions. The green part of Figure 1.11 (b) is roughly equal to the LHCb acceptance. Of all produced  $B$  mesons, about 25% are within the acceptance of the detector while only 8% of the total polar angle is covered.

# Chapter 2

## The LHC*b* experiment

The Large Hadron Collider (LHC) is a 14 TeV proton-proton collider located at CERN in Geneva. After a short pilot run in 2008, it will start to deliver proton beams in autumn 2009.

The proton bunches cross with a rate of 40 MHz. The rate of inelastic pp-collisions is dependent on how strongly the beams are focused, i. e., on the instantaneous luminosity. Figure 2.1 shows the probabilities for single and multiple proton-proton collisions as a function of the luminosity. In a dedicated study [46], the nominal luminosity for LHC*b* was found to be  $2 \cdot 10^{32} \text{ cm}^{-2} \text{ s}^{-1}$ , the maximal luminosity  $5 \cdot 10^{32} \text{ cm}^{-2} \text{ s}^{-1}$ . This range leaves some freedom to the final choice of luminosity. At the nominal luminosity, about 45 % of the bunch crossings lead to an elastic or inelastic proton-proton interaction. The rate of visible interactions, i. e., interactions with at least five tracks in the acceptance of the detector, is 14 MHz. The integrated luminosity in one year of running ( $10^7 \text{ s}$ ) at nominal luminosity is  $\mathcal{L} = 2 \text{ fb}^{-1}$ .

At the LHC, the two  $B$  mesons produced in the primary proton-proton collision are likely to fly in the same forward or backward cone, see Section 1.4. The LHC*b* detector

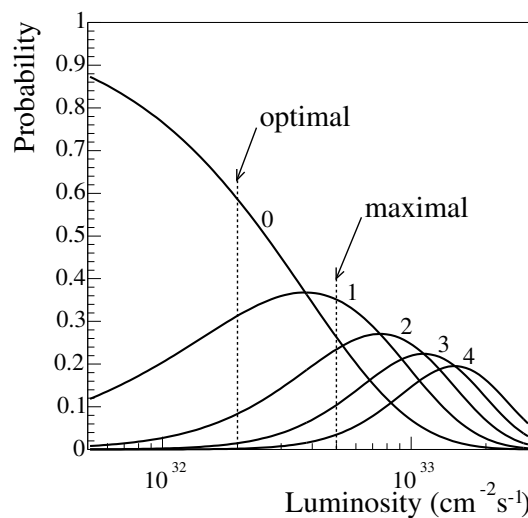


**Figure 2.1:** Probability of the different number of interactions as a function of the instantaneous luminosity. The nominal and maximal envisaged LHC*b* luminosities are indicated. (Figure from [47].)

is therefore designed as single arm, forward spectrometer having a large acceptance for  $B$  events, about 25%. The detector, whose layout is shown in Fig. 2.2, covers an acceptance of  $10 - 300$  mrad in the bending plane of the magnet ( $x$ -direction) and  $10 - 250$  mrad in the non-bending plane ( $y$ -direction). In the following sections, each of the subdetectors is described. They are categorized as follows:

- **Tracking detectors:** Vertex Locator (Velo), Trigger Tracker (TT), Inner Tracker (IT) and Outer Tracker (OT).
- **PID detectors:** First and second Cherenkov detectors (RICH 1 and RICH 2). The main purpose of the Cherenkov detectors is the separation between  $K^\pm$  and  $\pi^\pm$  over a wide momentum range. The reconstruction of the Cherenkov rings is very time consuming and is therefore not used in the trigger.
- **Calorimeter system:** The scintillating Pad Detector (SPD) and the Pre-shower detector followed by the main calorimeters: The electromagnetic (ECal) and hadronic (HCal) calorimeter.
- **Muon stations:** Five stations,  $M_1 - M_5$ , the first in front of the calorimeter system and the remaining four behind it.

The focus will be put in the following on the subdetectors relevant for this work. The two RICH detectors are omitted.

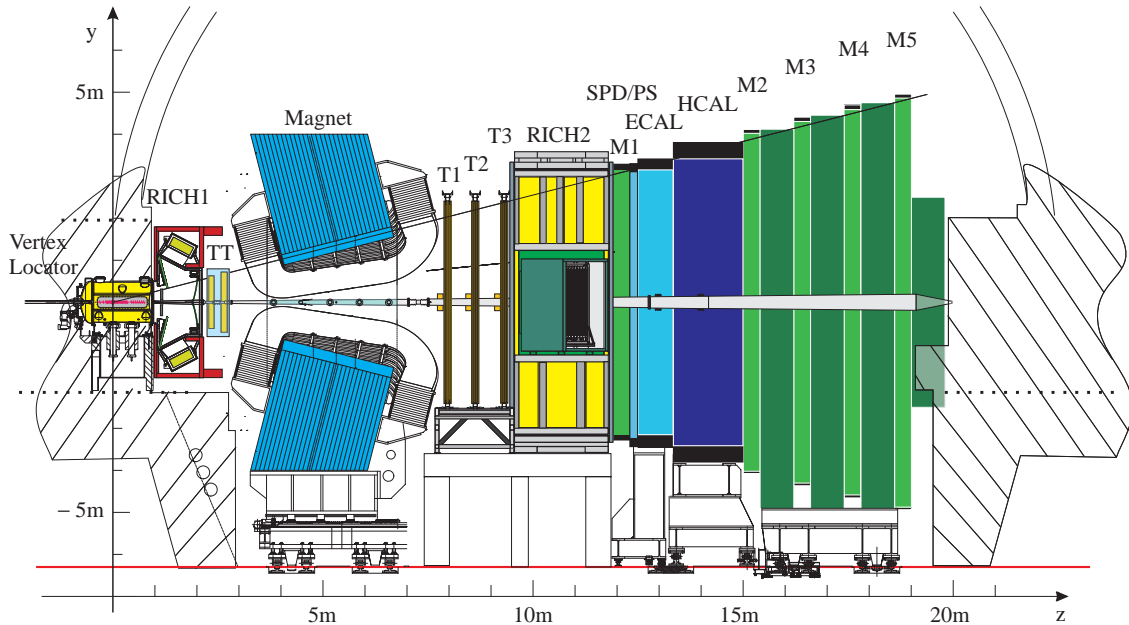


**Figure 2.2:** LHC*b* detector layout, showing the Vertex Locator (Velo), the dipole magnet, the two RICH detectors, the four tracking stations TT, T1-T3 (T-Stations), the Scintillating Pad Detector (SPD), Preshower (PS), Electromagnetic (ECal) and Hadronic (HCal) calorimeters and the five muon stations  $M_1 - M_5$ . (Figure from [47].)

## 2.1 Tracking System

Charged particles are bent in the magnetic field of the main dipole magnet [48]. Their momentum is measured from the deflection of the particle trajectories. The bending strength of the magnet is determined by the integrated magnetic field, which is

$$\int Bdl = 4.2 \text{ Tm}. \quad (2.1)$$

The magnetic field is designed such that it is large in  $y$  direction and small in  $x$  and  $z$  direction. This bends particles moving in  $z$  direction in the  $(x-z)$  plane (bending plane). The strength of the main component of the field ( $B_y$ ) along the  $z$  axis is shown in Figure 2.3 (a), the position of the tracking detectors are indicated by dashed lines.

The basic idea of the tracking system is sketched in Figure 2.3 (b): The magnetic field which bends all charged particles is located in the central part of the detector. The tracking detectors are placed in essentially field free areas which makes it possible to reconstruct tracks as straight lines. The bending of the magnet can to first order be approximated as a single kick at the center of the magnet, the track as the combination of two straight lines. The momentum of the particle is inversely proportional to the difference of the track slope in the Velo and the track slope in the T-Stations (“momentum kick” method). If only the T-Station part of the track is available, an estimate of the particle momentum can be made with the assumption that the particle originates from the primary interaction point. This *momentum kick* method is widely used in this thesis.

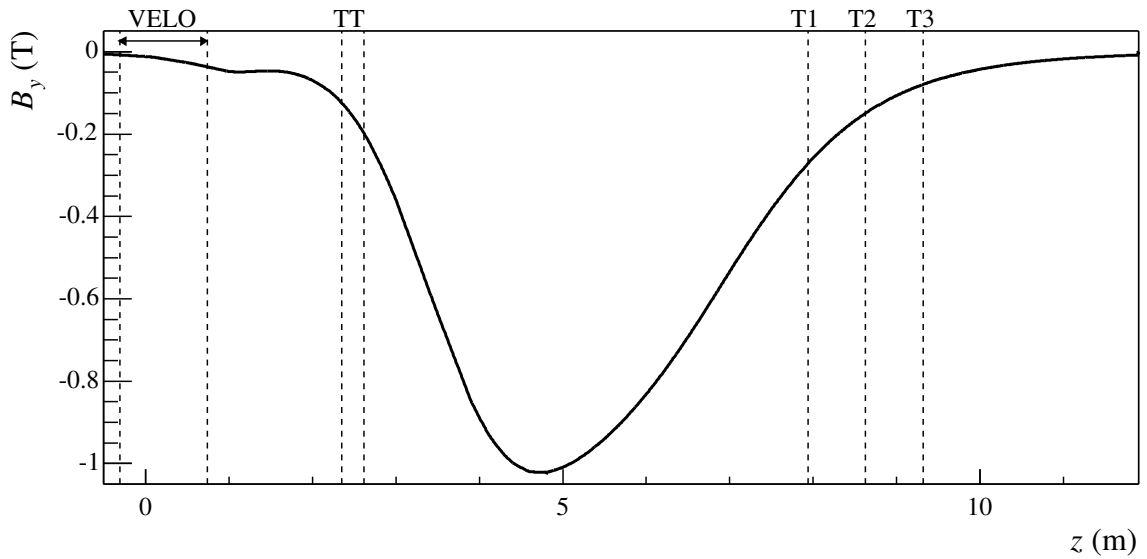
The quality of this approximation can be seen in Figure 2.3 (a): In the Velo, the fringe field is very low ( $B_y < 0.05 \text{ T}$ ) whereas in the first station of the main tracker it has about 30% of its maximal value. This leads to significant corrections to the straight line approximation in the T-Stations and the single kick approach, see Section 2.1.6.

### 2.1.1 Vertex Locator

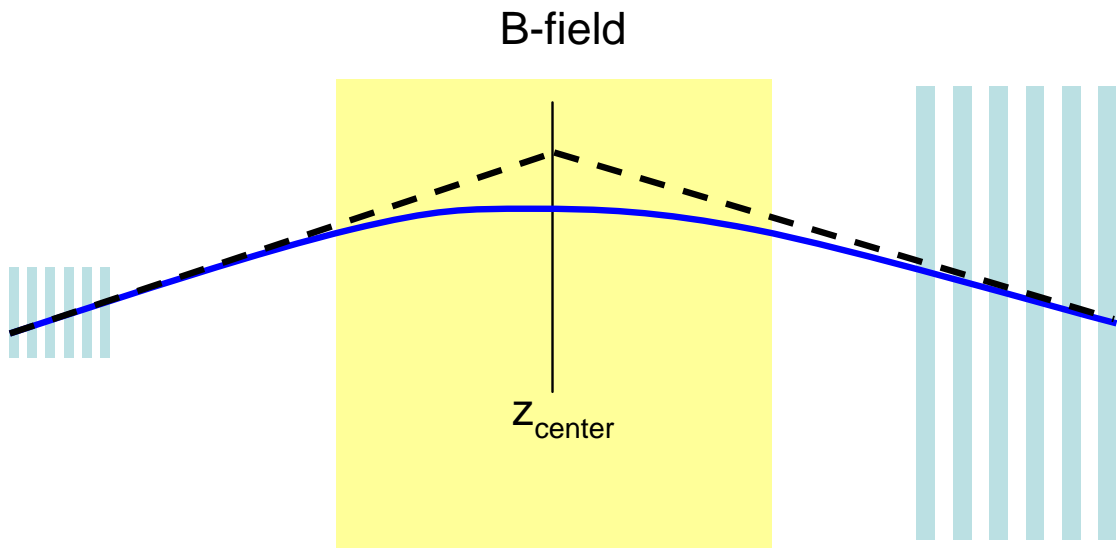
The Vertex Locator (Velo) [47, 49, 50] is built of 21 stations positioned around the interaction region as shown in Figure 2.4. Two types of silicon sensors are used: one measures the  $r$ -coordinate with circular strips centered around the beam axis, the other measures the  $\phi$ -coordinate with straight, radial strips, see Figure 2.5. The half disk sensors are arranged in pairs of  $r$  and  $\phi$ -sensors, mounted back to back.

The  $r - \phi$  geometry directly gives a projection in the  $(r-z)$  plane by using only  $r$ -measurements. In this projection, forward going tracks with a high impact parameter ( $IP$ ) with respect to the production vertex are easily identified. The trigger exploits this idea by first reconstructing all tracks in the  $(r-z)$  projection, before reconstructing only the ones with a large  $IP$  in three dimensions.

The  $300 \mu\text{m}$  thick sensors are based on single sided  $n + n$  technology. The particle flux is highest close to the beam axis and decreases away from the beam. The pitch of the sensors is therefore increasing from  $35.5 \mu\text{m}$  in the innermost strips ( $\phi$ -sensors,  $40 \mu\text{m}$  for  $r$ -sensors) to  $96.6 \mu\text{m}$  ( $101.6 \mu\text{m}$ ) in the outer strips to provide a homogeneous occupancy throughout the sensors. The average occupancy per channel is well below 1%.



(a) dominant component of the magnetic field



(b) principal idea of the tracking system and the “momentum kick” method

**Figure 2.3:** (a) The dominant component of the magnetic field ( $B_y$ ) along the  $z$ -axis. The tracking detectors are indicated, figure taken from [47]. (b) Concept of the tracking system: the tracking detectors (blue bars) measure the tracks outside the magnetic field as straight lines, the bending of the magnet is approximated as a kick in the center.

The sensitive area of the sensors starts at 8 mm from the beam axis such that the first measurement on the track is as close to the primary vertex as possible. The shorter the extrapolation of a track from its first measurement to the interaction region, the smaller is the error on the reconstructed position of the vertex. To protect the Velo sensors during beam injection, the Velo detector halves can be moved away from the

beam in horizontal direction.

The sensors are separated from the primary beam vacuum by a thin aluminium foil (RF foil) which prevents gas exchange between the Velo sensors and the ultra high vacuum of the LHC beam and shields the Velo electronics against radio frequency pickup from the beams. In stable running conditions (Velo closed), the RF foil has a clearance of 5 mm from the beam line.

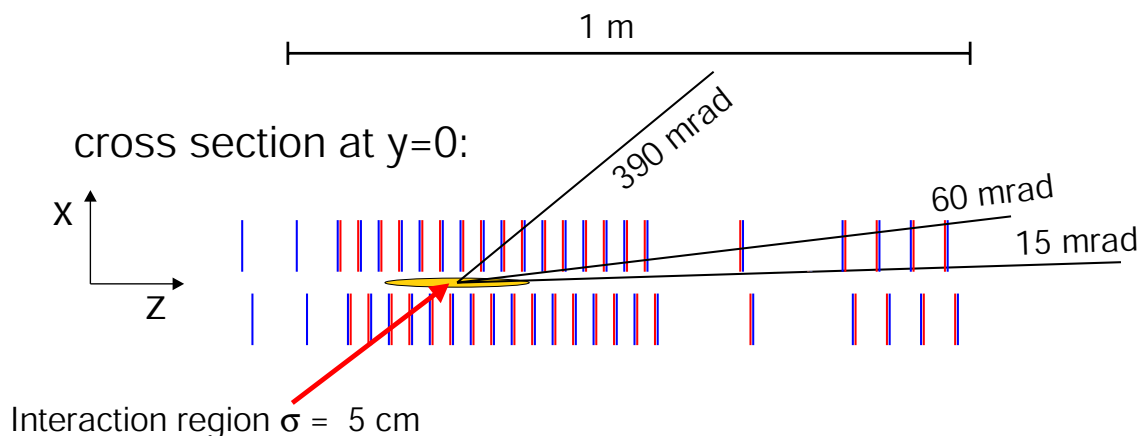


**Figure 2.4:** Setup of Velo modules around the interaction region, figure taken from [47].

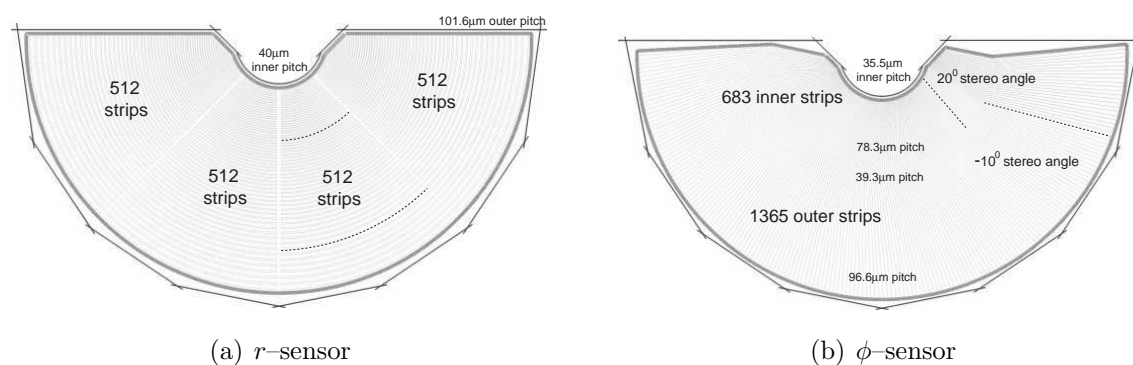


**Figure 2.5:** Sketch illustrating the  $r - \phi$  geometry of the Velo sensors. The different regions on the sensors are indicated with their pitch. Figure taken from [47].

### 2.1.2 Trigger Tracker

The Trigger Tracker (TT) [47] is located directly in front of the magnet, it consists of two stations separated by a distance of 27 cm. Each station of the TT has two layers of silicon strip detectors covering the full acceptance, see Figure 2.6. The strips in the four layers are arranged in  $(x, u)$  and  $(v, x)$  layers, corresponding to angles with the vertical  $y$  axis of  $(0^\circ, -5^\circ)$  and  $(5^\circ, 0^\circ)$ . The stereo angle allows the reconstruction of tracks in three dimensions. The vertical orientation of the strips is chosen to obtain a

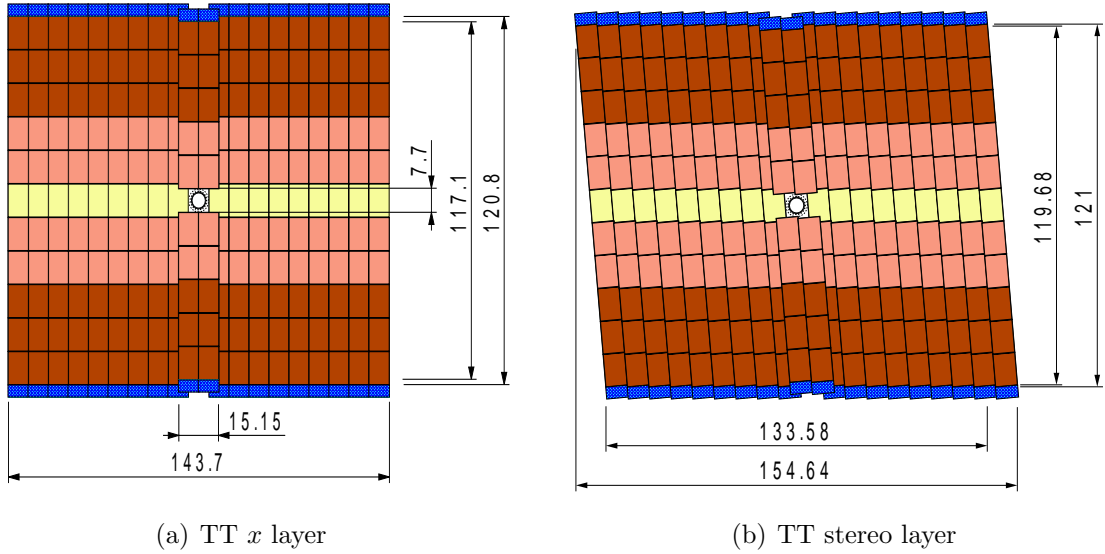


**Figure 2.6:** Layout of the Trigger Tracker: (a)  $x$  layer and (b) stereo layer. The different colors indicate the different sensor readout. Dimensions in the figure given in cm. (Figure taken from [47].)

better resolution in the bending plane of the magnet and therefore a better precision on the measured momentum.

A layer is built of sensors with the dimensions of  $11\text{ cm} \times 7.8\text{ cm}$ . In total, the detector covers an area of  $8.4\text{ m}^2$ . The silicon sensors have a thickness of  $500\text{ }\mu\text{m}$ , the strip pitch is  $183\text{ }\mu\text{m}$ . Depending on their distance from the beam pipe, the strips of three or four neighboring sensors are connected such that they share a single readout. This results in a spatial resolution of about  $50\text{ }\mu\text{m}$  [47].

### 2.1.3 Inner Tracker

The Inner Tracker (IT) [51] covers the innermost region of the T-Stations which receives the highest flux of charged particles. The IT is placed around the beam pipe in a cross shape, see Figure 2.7. The IT covers approximately 2% of the  $6\text{ m} \times 5\text{ m}$  acceptance of the T-Stations, but it measures about 20% of the particle flux. Each station has layers arranged in a  $(x, u, v, x)$  configuration, similar to the TT.

Two types of silicon  $p^+$  on  $n$  sensors of different thickness, but otherwise identical design are used in the IT. The single sensors, which are  $320\text{ }\mu\text{m}$  thick, are placed above and below the beam pipe. The double sensors, which are  $410\text{ }\mu\text{m}$  thick, are placed at the sides of the beam pipe. The two types were chosen to ensure sufficiently high signal to noise ratios for each module type while minimizing the material budget of the detector. The strip pitch is  $198\text{ }\mu\text{m}$  resulting in a resolution of approximately  $50\text{ }\mu\text{m}$  [47]. The maximal occupancy in the IT is below 2%.

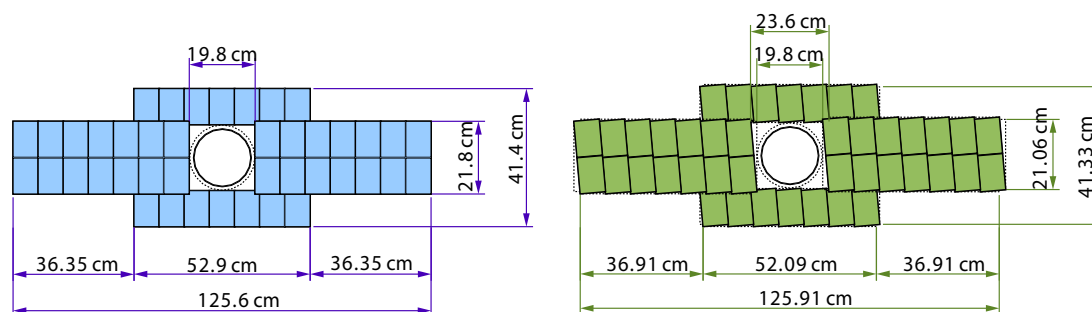


**Figure 2.7:** Layout of an Inner Tracker  $x$  and  $u$  layer with the silicon sensors in the cross shaped configuration. In the middle, a cross section of the beam pipe is drawn. (Figure from [21].)

### 2.1.4 Outer Tracker

The Outer Tracker (OT) [52] covers the large region outside the acceptance of the Inner Tracker, see Figure 2.8 (a). Charged particles are detected in the OT with gas filled straw tubes serving as drift cells. The gas mixture to operate the OT is  $Ar(70\%)/CO_2(30\%)$ .

The inner diameter of the straws is 5 mm and the pitch between two straws is 5.25 mm. At the center of the straw is a  $24\ \mu m$  thick gold coated tungsten wire which operates as anode. Wire locators are placed every 80 cm to keep the wires at their nominal position. The cathode cell wall consists of two foils: the inner windings are made of a  $40\ \mu m$  thick carbon doped polymer foil (Kapton-XC) and the outer windings are made of a  $25\ \mu m$  Kapton-XC foil with a  $12.5\ \mu m$  aluminium coating. The straws are fixed in a module between two panels which form a stiff, gas-tight box.

The front-end electronics measure pulses that appear on the anode wire above a

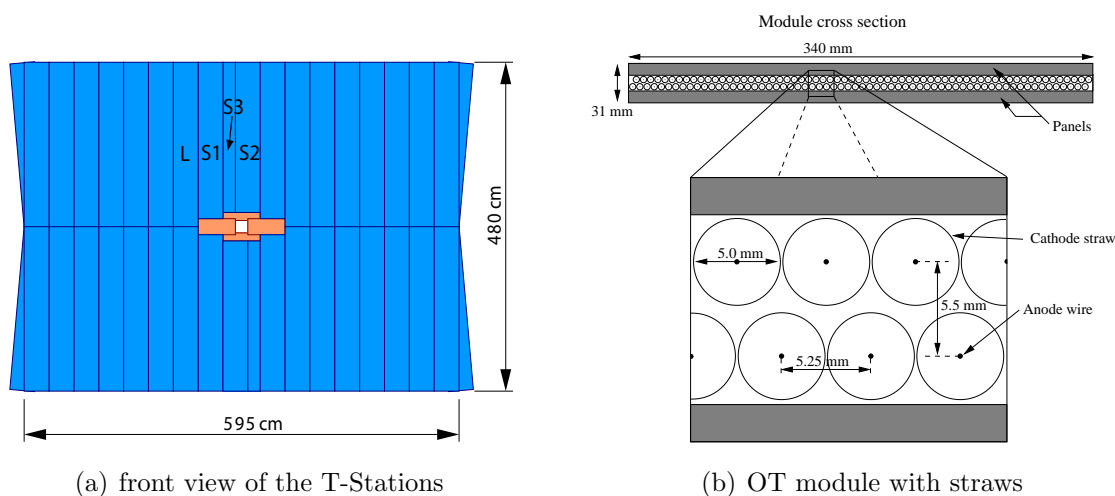


**Figure 2.8:** Outer tracker: (a) Front view of an OT station. The four boxes in the center depict the IT. (b) Cross section of an OT module (128 straws). A small region containing a few straws is magnified. (Figure from [21].)

threshold. The time difference between the measurement and the reference given by the bunch clock of the LHC is related to the drift distance of the primary electrons in the straws. To include the maximum drift time and signal delays, i. e., due to the signal propagation time on the wire or in the electronics, the read out window of the OT is open for three consecutive bunch crossings (75 ns). The average cell efficiency is 98 %, the spatial resolution of the OT is better than 200  $\mu\text{m}$  [53].

The modules are arranged in the same  $(x, u, v, x)$  topology as the IT and the TT. All three stations are of equal size, which is determined by the requirement that the last station is still in the acceptance of  $300 \text{ mrad} \times 250 \text{ mrad}$  in  $x \times y$  direction. The straws are arranged as double layers in modules. Each module contains 128 straws staggered in two monolayers of 64 straws. The arrangement of the straws in a module is sketched in Figure 2.8 (b). The 8 innermost modules of each layer are smaller, they are arranged around the IT. The innermost modules contain 64 straws in a double layer. The use of light materials is important for the minimization of scattering and hadronic interactions. The total radiation length of the OT is below 10%.

### 2.1.5 Tracking strategy and performance

The first step in the track reconstruction is the pattern recognition or track finding, where the correct hits belonging to one track are searched for. The number of reconstructed ghost tracks, i. e., tracks with many wrong hits, should be kept to a minimum. A track is called a ghost if less than 70 % of the hits on the track originate from the same generated particle. For example, a real track in the Velo which is matched to a real track in the T-Stations but from a different particle is called a ghost track. The tracks are classified in different types, depending on their trajectory in the LHC***b*** spectrometer. They are sketched in Figure 2.9 and can be described as follows:

- **Long tracks** are the best quality physics tracks of LHC***b***. They traverse the complete tracking system from the Velo to the T-Stations.
- **Upstream tracks** are only reconstructed in the Velo and TT-Stations. They are bent out of the acceptance in the dipole magnet. Although their momentum resolution is reduced, they can be used in some  $B$  decay analyses.
- **Downstream tracks** are only reconstructed in the TT and T-Stations. They allow the reconstruction of  $K_S^0$  decays outside of the Velo acceptance.
- **Velo tracks** traverse only the Velo. They allow a precise determination of the primary vertex as they have typically a large polar angle.
- **T-tracks** are only reconstructed in the T-Stations.

The aim of the pattern recognition is to find for each particle the best possible track, i. e., the track which uses measurements in all subdetectors the particle crossed. To get the maximum number of long tracks, two redundant reconstruction algorithms are used, called “forward tracking” and “track matching”. As many tracks will be reconstructed by both algorithms, a *clone killing* algorithm will clean up duplications (tracks are called “clones” if they share at least 70 % of their hits). Both algorithms start with standalone Velo tracks, therefore this algorithm will be described first:

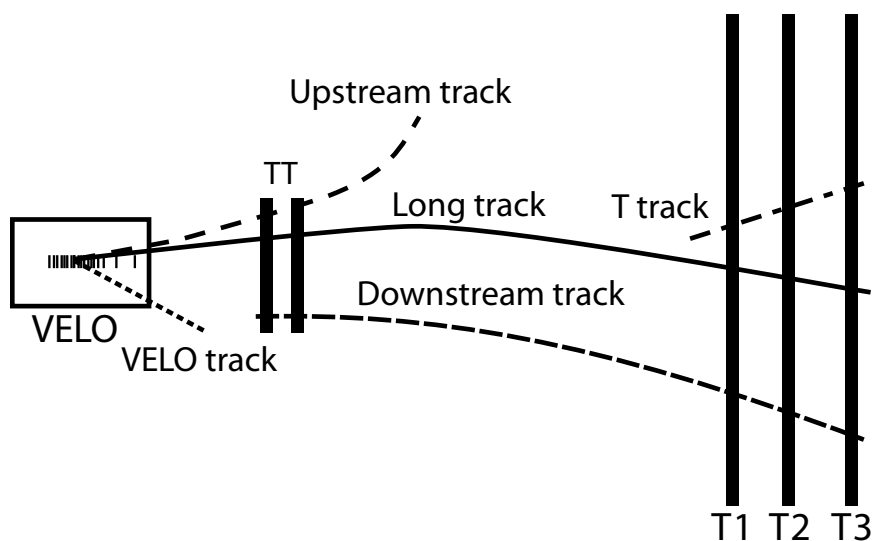


**Figure 2.9:** Sketch of the five different track types in the LHC $b$  track reconstruction. (Figure from [47].)

- Standalone Velo tracking:** The magnetic field in the Velo is sufficiently low, the tracks can be reconstructed as straight lines. The algorithm [54] starts with trajectories in the  $(r-z)$  plane. These tracks are called Velo 2D tracks. The priority is to have a high efficiency and a low ghost rate. The Velo 2D tracks are then extended to 3D tracks by adding hits from the Velo  $\phi$ -sensors. Both Velo 2D and 3D track finding algorithms assume that the tracks originate from the same vertex. The resulting track segments serve as seed for the other track finding algorithms.
- Forward tracking:** This algorithm [55] starts from the Velo tracks and uses them as seeds to find continuations in the T-Stations. The algorithm is based on the idea that a single hit in the T-Stations together with the Velo track segment define the complete trajectory of the track. The trajectory is parameterized by a second order polynomial in  $y$  and a third order polynomial in  $x$ . Further T-Station hits in a window around the expected position are picked up. The candidates with the most hits are selected and their hits are assigned to the track. Finally, a likelihood is calculated to confirm the correct tracks and discard wrongly reconstructed combinations (*ghosts*). Hits in TT are picked up if they are close enough to a track through Velo and T station hits.
- Track matching** In the track matching, standalone Velo tracks are matched to standalone T-Station tracks. The T-Station track finding algorithms are described in detail in Section 4.3.1. The T-track and the Velo track are matched by extrapolating both track segments to the bending plane of the magnet and evaluating quality criteria as the position in the bending plane or the change of the track slope. TT hits close to the resulting tracks are added afterwards.

The Velo and T-tracks that are not used as part of either long, upstream or downstream tracks are defined to be of type Velo and T-track respectively. The tracking strategy is described in more detail in reference [56].

### Tracking performance summary

The tracks reconstructed by the different algorithms presented above are fitted using a Kalman Filter based track fit, see Section 5.1.1. Duplicate tracks are then removed by a *clone killing* algorithm [57], the final performance is evaluated on these cleaned tracks. The accuracy of the estimated track parameters are determined by the track fit. Their value at the location of the vertex is an important measure of the LHCb track reconstruction performance as they are directly used to reconstruct and select  $B$  decays.

*Long tracks* are the most accurately measured tracks in LHCb. Dependent on the track momentum, the relative momentum resolution is between 0.35 % and 0.55 %, as shown in Figure 2.10 (a). The rise of the momentum resolution towards low momenta is caused by the decrease in hit purity [21]. Another important measure for the performance of the tracking system is the impact parameter ( $IP$ ) with respect to the true Monte Carlo vertex. The  $IP$  resolution rises linearly with  $1/p_T$ , as shown in Figure 2.10 (b). It is measured with a resolution down to  $14 \mu\text{m}$ .

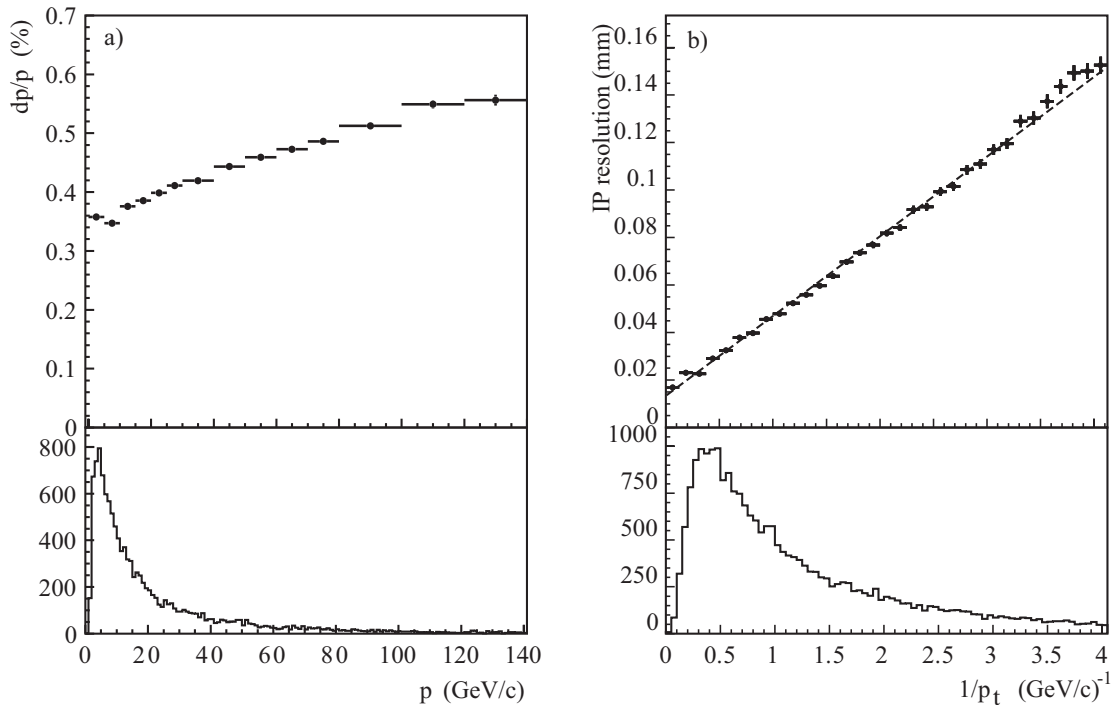


**Figure 2.10:** Resolution of the reconstructed track parameters at the production vertex of the track: (a) momentum resolution as a function of track momentum, (b) impact parameter resolution as a function of  $1/p_T$ . For comparison, the momentum and inverse  $p_T$  spectra are shown at the lower part of the plots. (Figure from [47].)

### 2.1.6 Fast momentum estimation

The momentum of the particle can be calculated from a track reconstructed in the main tracker and the assumption that the particle originated from the nominal interaction point. This fast estimate of the momentum can be used in the trigger without applying a time consuming track fit.

An ideal magnet would act as a thin lens such that the track outside the magnet could be described as two straight lines which intersect in the middle of the magnet. In LHC*b*, there are some fringe fields outside the magnet volume, which cover the first tracking station (T1) with about 30 % of the maximal field, see Figure 2.3. Therefore, a higher order polynomial has to be used to parameterize the track. A cubical parameterization has turned out to describe the best the path of the track through the remaining field behind the magnet [55]. To calculate the momentum, first the extrapolated intersection of the track with the origin,  $x_0$ , is calculated as

$$x_0 = x - t_x \cdot z, \quad (2.2)$$

where  $x$ ,  $z$  and  $t_x$  are the position and slope coordinates from the track. The track momentum is then calculated from a parameterization to  $x_0$  and the track directions  $t_x$  and  $t_y$ :

$$p = \frac{a_0 + a_1 \times t_x^2 + a_2 \times t_y^2 + a_3 \times x_0^2}{x_0}, \quad (2.3)$$

where the parameters  $a_0 - a_3$  are determined from a generator level study [55, 58]. This fast calculation of the T-track momentum has a relative precision between 2 % and 4 % and takes less than 20  $\mu$ s per track.

## 2.2 Calorimeter system

The main purpose of the calorimeter system [59] is to identify electrons, photons and hadrons and to provide measurements of their energy and position. Besides its use in the offline analysis, this information is the basis of the hardware trigger, therefore it has to be provided with sufficient selectivity in a very short time. To differentiate between electrons and photons, the shower detection is longitudinally segmented, it consists of four elements, as sketched in Figure 2.11:

- a single layer Scintillating Pad Detector (SPD) to differentiate between charged and neutral particles,
- a Pre-Shower Detector (PS) which is located after a 12 mm lead wall,
- an electromagnetic calorimeter (ECAL) and
- a hadronic calorimeter (HCal).

The calorimeter acceptance is 300 mrad horizontally and 250 mrad vertically, matching the acceptance of the tracking system.

Through their interaction with the calorimeter material, incident particles produce a cascade of secondary particles which are finally absorbed. This cascade is called

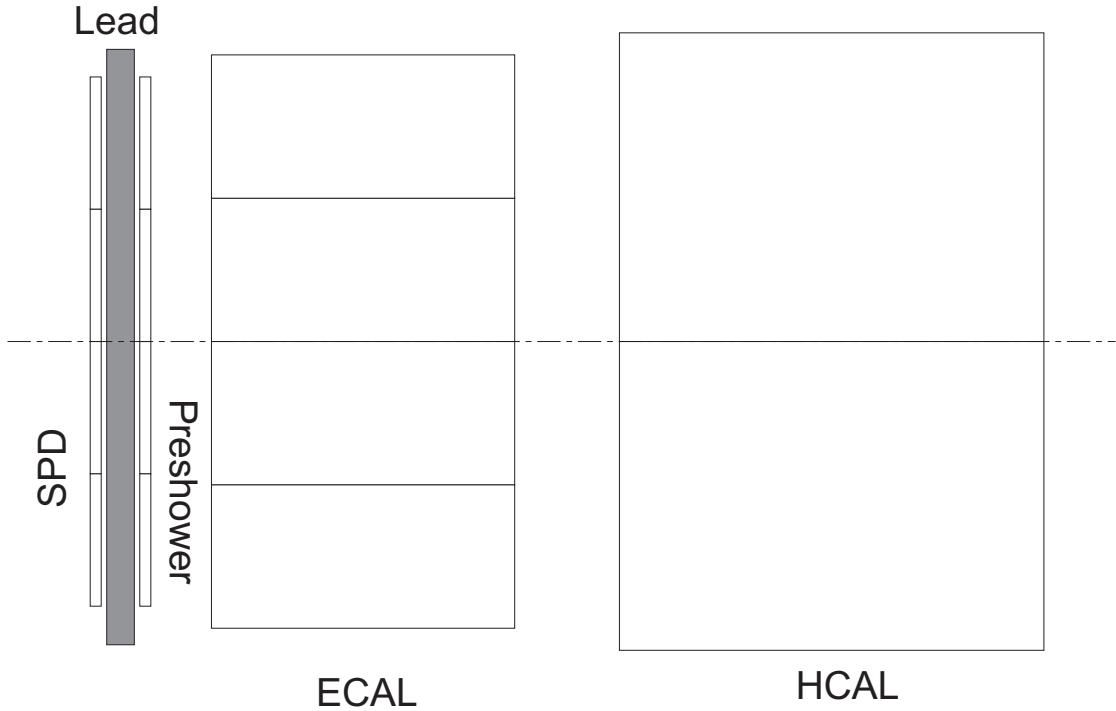


**Figure 2.11:** Schematic side view of the calorimeter system. (Figure from [60].)

shower. The ionizations induced by this particle shower produces scintillation light in the active detector material. The total amount of scintillation light produced by the shower is proportional to the deposited energy. The LHC*b* calorimeters are sampling calorimeters, i. e., they are constructed of a sequence of layers of passive absorbing material alternated by active detection layers.

### 2.2.1 Preshower and Scintillating Pad Detector

The SPD and PS provide information of the electromagnetic shower development to give an initial particle identification of the ECal. First, charged particles are detected in the SPD where neutral ones leave no signal. In this way, electrons can be distinguished from photons.

Between the SPD and the PS, a 12 mm thick lead wall initiates an electromagnetic shower. Since hadronic showers start later, the pre-shower detector is used to discriminate electromagnetic showers from hadronic showers.

Both detection planes of the SPD and PS consist of 15 mm thick scintillation pads. The scintillation light is collected in each pad by a wavelength shifting fiber and directed to photomultipliers outside of the acceptance. The total thickness in  $z$  of the SPD/PS system is 180 mm. The  $z$  position and the lateral segmentation of the PS and SPD are summarized in Table 2.1. The PS and SPD have the same lateral dimensions as the ECal.

**Table 2.1:** Position, depth and dimensions of the four components of the calorimeter system [47]. The SPD, PS and ECal have the same segmentation, the HCal segmentation is significantly coarser.

	$z$ position (mm)	depth $X_0 / \lambda$	segmentation (mm <sup>2</sup> )		
			inner part	middle part	outer part
SPD	12 300	2/0.1			
PS	12 400		40.4 × 40.4	60.6 × 60.6	121.2 × 121.2
ECal	12 500	25/1.1			
HCal	13 330	−/5.6	131.3 × 131.3	–	262.6 × 262.6

### 2.2.2 Electromagnetic Calorimeter

The electromagnetic calorimeter is constructed in shashlik technology, i. e., a sampling structure of 66 alternating layers of 2 mm lead and 4 mm thick scintillator plates. This fulfills the needs in terms of a modest energy resolution, fast time response and a good radiation hardness. The ECal depth accounts for 25 electromagnetic interaction lengths ( $X_0$ ) and 1.1 hadronic interaction lengths ( $\lambda$ ), its design energy resolution is

$$\sigma(E)/E = 10\%/\sqrt{E} \oplus 1.5\% \quad (2.4)$$

with the energy  $E$  is expressed in GeV and  $\oplus$  means addition in quadrature.

The geometrical dimensions of the ECal are summarized in Table 2.1. The front view of an quarter of the ECal is sketched in Figure 2.12 (a).

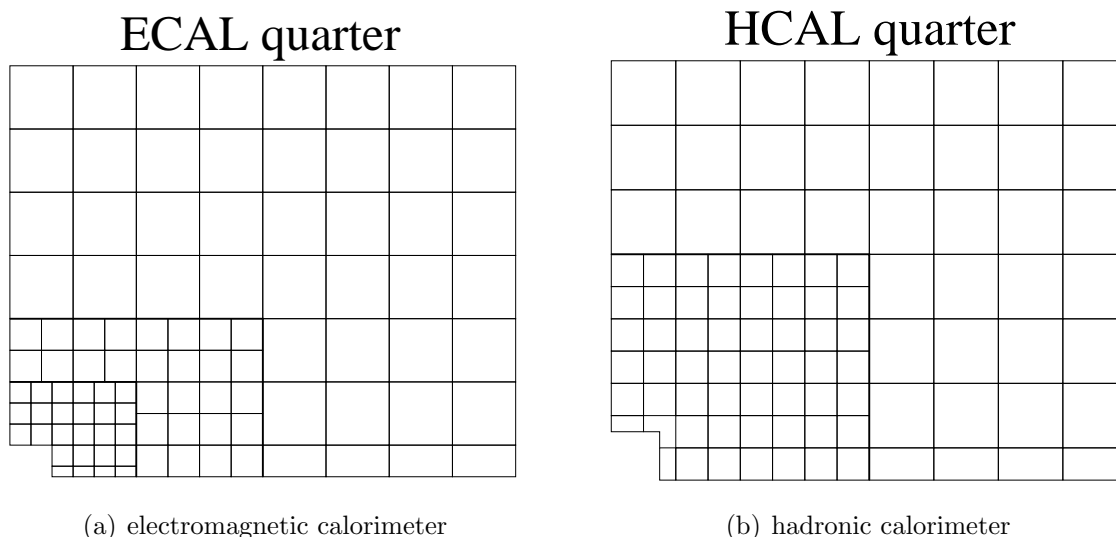


**Figure 2.12:** Front view of an (a) ECal and (b) HCal quarter showing the lateral segmentation. Each square in the ECal represents 16 pads, in the HCal 4 pads. The PS and SPD detectors have the same segmentation as the ECal. (Figure from [59].)

### 2.2.3 Hadronic Calorimeter

The hadronic calorimeter is a sampling device made from iron absorbers and scintillating tiles as active material. The scintillating tiles are oriented to run parallel to the beam axis. In the lateral direction, the tiles are interspersed with 1 cm of iron and in longitudinal direction the length of the tiles and iron spacers correspond to the hadron interaction length in steel. The HCal is segmented transversely into square cells of size 131.3 mm<sup>2</sup> (inner region) and 262.6 mm<sup>2</sup> (outer region). Readout cells of different size are defined by grouping together different sets of fibers onto one photomultiplier tube. The total depth of the HCal accounts for  $5.6 \lambda$ , its energy resolution is

$$\sigma(E)/E = 80 \% / \sqrt{E} \oplus 10 \% , \quad (2.5)$$

with the energy  $E$  in GeV.

The geometrical dimensions of the HCal are summarized in Table 2.1. The front view of a quarter of the HCal is sketched in Figure 2.12 (b). The HCal cells are projective to the ECal cells.

## 2.3 Muon system

The muon system [61] consists of five stations. The first station ( $M_1$ ) is located in front of the calorimeter system to improve the momentum measurement, whereas the other stations ( $M_2 - M_5$ ) are located directly behind the hadronic calorimeter, as shown in Figure 2.13 (a). The inner and outer angular acceptances of the muon system are 20 mrad (16 mrad) and 306 mrad (258 mrad) in the bending (non-bending) plane respectively. This results in an acceptance of about 20 % for muons from inclusive  $b$  semileptonic decays. The stations  $M_2 - M_5$  are separated by 80 cm thick iron filters, corresponding to a total of 20 interaction lengths. The minimum momentum of a muon to cross the five stations is approximately 6 GeV.

A pad readout structure provides binary space point measurements of the muon tracks, allowing fast track finding in the hardware trigger. Each station is divided in four regions with different pad granularity, see Figure 2.13 (b). The granularity of each region is adjusted to the expected particle flux. The regions and their pads increase in size from  $M_1$  to  $M_5$  so that they are mutually projective towards the interaction point. The dimensions of the pads decrease towards the inner regions such that their hit occupancy stays roughly constant. In addition, their size in  $x$  is smaller than that in  $y$ , giving a more accurate momentum measurement. The pad dimensions are summarized in Table 2.2.

The muon stations are instrumented with multi-wire proportional chambers (MWPC) [62], which fulfill both the requirement from the trigger to collect the signal within 20 ns and the requirement for radiation hardness. The required granularity is obtained by grouping anode wires and the cathode pads of the MWPCs. In the innermost region of the first muon station, where the particle density will be higher, triple-GEM detectors [63] are used.

The muon stations are used in the L0 trigger which requires hits in all five muon stations, see Section 3.1.1. To unambiguously identify the bunch crossing, the time

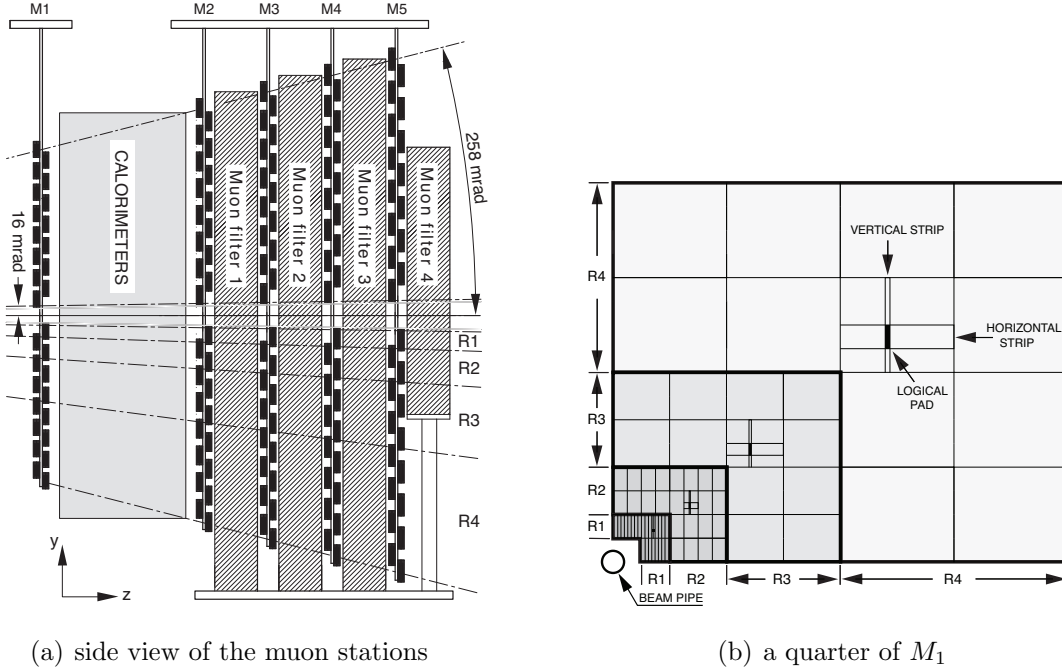


**Figure 2.13:** Muon System: (a) Side view. (b) Front view of one muon station quadrant showing the partitioning into sectors. The intersection of a horizontal and a vertical strip defines a logical pad (see text). (Figures from [47].)

window must be smaller than 25 ns. The necessary time resolution is ensured by a fast gas mixture and an optimized charge-collection geometry both for the MWPC and the GEM detectors. Depending on station, the chambers are composed of two or four gas gaps connected with a logical OR. In stations  $M_2 - M_5$  the MWPCs are composed of four gas gaps arranged in two sensitive layers with independent readout. In station  $M_1$  the chambers have only two gas gaps to minimize the material in front of the electromagnetic calorimeter. In region one of  $M_1$  two superimposed GEM chambers connected in OR are used.

**Table 2.2:** Position and dimensions of the five muon stations [47]. Rows R1–R4: granularity of the different regions of the muon detector. Given are the  $x \times y$  pad dimensions in  $\text{mm}^2$  and the  $z$  positions in mm.

(mm)	$M_1$	$M_2$	$M_3$	$M_4$	$M_5$
$z$	1 210	1 527	1 647	1 767	1 887
R1	10×25	6.3×31	6.7×34	29×36	31×39
R2	20×50	12.5×63	13.5×68	58×73	62×77
R3	40×100	25×125	27×135	116×145	124×155
R4	80×200	50×250	54×270	231×290	248×309

### 2.3.1 Standalone muon track reconstruction

In the offline reconstruction the tracks traversing the spectrometer are extrapolated to the muon stations and a search for muon hits in a region of interest is done [64]. For the online reconstruction, a standalone muon track search is implemented [65]. Standalone muon tracks, called “muon segments” (abbreviated as  $\mu$ -seg) are reconstructed with the following algorithm:

Hits in the last muon station ( $M_5$ ) are taken as seeds, the algorithm extrapolates a partial segment ( $M_5 - M_{i+1}$ ) to station  $M_i$ . When hits in all stations  $M_5 - M_2$  are found, a muon track, called *muon segment*, is created. The first muon station  $M_1$ , located in front of the calorimeters, is not used because of its high occupancy. The standalone muon track reconstruction takes about 0.2 ms. These *muon segments* will be used for the muon trigger implementation in Chapter 4 and Chapter 5.

## 2.4 Monte Carlo simulation

The LHCb experiment uses a detailed simulation and reconstruction program where most parameters are tuned to test-beam results or measurements taken from cosmic events.

The simulation of an event resulting from a proton–proton collision is based on the Monte Carlo technique [66]. These generated Monte Carlo (MC) events are treated completely analogous to real events. Thus, the same reconstruction software which will be used on real data is already used on the generated events. In absence of real data, the MC data is the only way to simulate the performance of the LHCb experiment.

To investigate the trigger performance, a number of events from proton–proton collisions is simulated as they are expected to be produced at the LHC. These events are commonly referred to as “minimum bias” events, as they would be recorded when the trigger is put in a mode that randomly selects events without bias.

In the simulation studies in this thesis, two event types are distinguished: *minimum bias* events and *signal* events. The latter are events that are only generated in a specific decay channel. To evaluate the trigger performance, the signal events accepted by the trigger are normalized to events that are selected by the respective analysis channel (*offline selected*). The trigger selection efficiency, which is commonly used in this thesis, is thus defined as:

$$\text{trigger efficiency} = \frac{\text{offline selected events that pass the trigger}}{\text{offline selected events}}. \quad (2.6)$$

This reflects the basic philosophy of the trigger development: the trigger aims to reconstruct the events selected by the different analyses and aims to modify the acceptances in the observables as little as possible. It is, however, not intended to reconstruct signal events which are not selected by the respective analysis. These events are treated as background.

### 2.4.1 Framework and applications

The LHCb software framework is described in detail in [67], it is only briefly described here. It is implemented within the object orientated framework of GAUDI [68]. The

framework is written in `C++` and consists of services that allow sharing of basic functionality such as job steering, message logging, data access and analysis. All studies performed in this thesis are done within the *Data Challenge 06* framework. The software versions used are `DaVinci v20r3`, `Rec v5r12` and `Hlt v4r3`.

## 2.4.2 Generated events

The events are generated by simulating the pp-collision using the external program `Pythia v6.2` [69]. The decay of  $B$  hadrons is controlled by another external program: `EvtGen` [70]. Both programs are steered by the `GAUDI` application called `Gauss` [71]. The evolution of the particles in the detector is simulated by the `GEANT4` package [72], which is also controlled by `Gauss`. An important service in the `GAUDI` framework is the material service [73], it deals with all aspects of the detector like its geometry description, alignment and calibration.

The datasets used in this thesis are summarized in Table 2.3. The algorithm tuning in Chapter 4 is done with simulated events whereas the trigger implementation in Chapter 5 and the physics studies in Chapter 6 are done with events which are accepted by the respective analysis (“offline selected” events). The analysis used for the selection is given in the section where it is used. For the trigger tuning and performance evaluation, a set of *benchmark channels* which contain the *offline selected* events are provided to the trigger group, they are described in Reference [74]. To save processing power, the `LHCb` simulation is limited to a region of 400 mrad around the beam pipe (the `LHCb` acceptance is 300 mrad). The generator level cut efficiency describes the fraction of all generated events which lie inside this region.

**Table 2.3:** Simulated datasets used in this work. The given number of events correspond to the number of generated events. The last four data samples are *offline selected* events, which have passed the selection criteria of the respective analysis, see [74].

type	# events	dataset
minimum bias	$4.8 \times 10^6$	DC06/L0-v1-lumi2-minbias
$B_s \rightarrow J/\psi(\mu^+\mu^-)\phi(KK)$	$1 \times 10^6$	DC06/phys-v4-lumi2-Bs-JPsiPhi,mm=CPV,DecProdCut
$B_d \rightarrow J/\psi(\mu^+\mu^-)K^{*0}(K\pi)$	10 000	DC06/phys-lumi2-Bd-JPsiKst,mm,DecProdCut
$B^+ \rightarrow J/\psi(\mu^+\mu^-)K^+$	10 000	DC06/phys-lumi2-Bd-JPsiKst,mm,DecProdCut
$B_s \rightarrow J/\psi(e^+e^-)\phi(KK)$	10 000	DC06/phys-lumi2-Bs-JPsiPhi,ee=CPV,DecProdCut
$B_d \rightarrow \pi^+\pi^-$	100 000	DC06/phys-lumi2-Bd-PiPi=CPV,DecProdCut
$B_s \rightarrow \mu^+\mu^-$	1 000	selected trigger benchmark channels [74]
$B_d \rightarrow K^{*0}\mu^+\mu^-$	1 000	selected trigger benchmark channels [74]
$B_s \rightarrow D_s^-\pi^+$	1 000	selected trigger benchmark channels [74]
$B_s \rightarrow \phi\phi$	1 000	selected trigger benchmark channels [74]



# Chapter 3

## The LHCb trigger system

This chapter gives a general overview of the LHCb trigger system. First, the L0 hardware trigger is discussed and then an overview of the software trigger will be given. Fast track reconstruction algorithms for the software trigger and the software trigger for muons and hadrons are studied in Chapter 4 and 5. A performance overview of the complete trigger chain will be given in Section 5.5.

Throughout this thesis, the trigger performance will be evaluated in terms of *trigger efficiency* and *minimum bias rate*. The *trigger efficiency*, as introduced in Section 2.4, is the relative efficiency to trigger events which are selected by the respective analysis. The *minimum bias rate* is the rate at which minimum bias events (see Section 2.4) are accepted by the respective trigger stage.

### 3.1 The L0 hardware trigger

The LHC bunch crossing frequency is 40 MHz, of which the LHCb detector at nominal luminosity will see events with at least one visible interaction<sup>1</sup> at a rate of 14 MHz, see Chapter 2. The purpose of the L0 trigger [60] is to reduce the rate to 1.1 MHz with which the entire detector will be read out. The L0 trigger reconstructs and selects particles with high transverse momentum in the muon chambers or with high transverse energy in the calorimeter system. It also provides the possibility to veto events which are particularly busy or which have multiple primary vertices. The total latency of the L0 trigger is 4  $\mu$ s, while the latency of the hardware algorithms in the calorimeter and muon detectors is 1  $\mu$ s. In the following, the subsystems of the L0 trigger will be discussed.

#### 3.1.1 The hardware muon trigger

The L0 muon trigger [60] looks for muon tracks with a high transverse momentum ( $p_T$ ). The track finding algorithm applied in the hardware searches for hits on a straight line through the five stations, giving a high purity muon identification, details of the algorithm are described in Figure 3.1. The expected relative transverse momentum

---

<sup>1</sup>A visible interaction is defined as an interaction which leaves at least five tracks in the acceptance of the spectrometer.

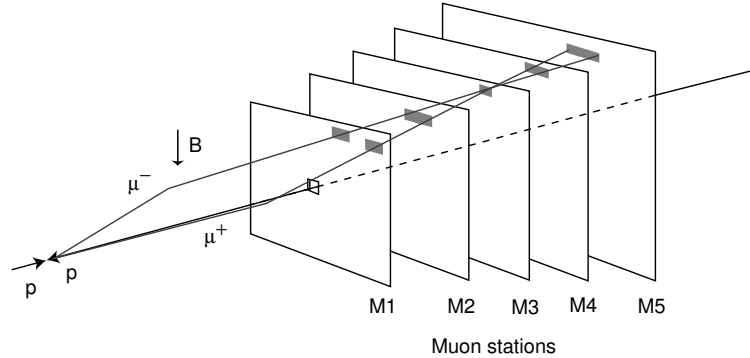


**Figure 3.1:** Track finding by the L0 muon trigger. For each logical-pad hit in  $M_3$ , hits are sought in  $M_2$ ,  $M_4$  and  $M_5$ , in a field of interest (highlighted) around a line projecting to the interaction region. When hits are found in the four stations, an extrapolation to  $M_1$  is made from the hits in  $M_2$  and  $M_3$ , and the  $M_1$  hit closest to the extrapolation point is selected. The track direction indicated by the hits in  $M_1$  and  $M_2$  is used in the  $p_T$  measurement for the trigger, assuming a particle from the interaction point and a single kick from the magnet. In the example shown,  $\mu^+$  and  $\mu^-$  cross the same pad in  $M_3$ . (Figure from [60].)

resolution of the L0 muon trigger is 30 %, as shown in Figure 3.2 (a). The two muon tracks with the highest  $p_T$  are selected for each quadrant of the muon stations. This results in up to eight muon candidates. The L0 muon trigger has two selections:

- **Single muon:** The single muon trigger requires a candidate with a minimum  $p_T$  of 1.3 GeV. At a minimum bias rate of 205 kHz, on average 1.1 candidates (as shown in Figure 3.2 (b)) are selected.
- **Dimuon:** The dimuon trigger requires two candidates with  $|p_T(1)| + |p_T(2)| > 1.5$  GeV. On simulated minimum bias data, it selects on average 1.2 vertices at a rate of 44 kHz.

The signal efficiencies and minimum bias rates are summarized in Table 3.1. The signal efficiency of the single muon trigger is 91.8 % for  $B_s \rightarrow J/\psi\phi$  events. For the dimuon trigger, the efficiency is only 65.6 % as many of the  $J/\psi \rightarrow \mu\mu$  decays have only one muon with sufficiently high transverse momentum. In addition, the trigger reconstruction puts strict requirements on the number of hits on the muon track [60], which limits the efficiency if two online muons are required.

### 3.1.2 The hardware calorimeter trigger

The Level-0 calorimeter trigger searches for particles with a high transverse energy deposit ( $E_T$ ) in the calorimeters. It provides candidates for charged hadrons, electrons, photons and neutral pions. The transverse energy is measured in the electromagnetic and hadronic calorimeter (ECal and HCal). As the expected showers of  $e^\pm$ ,  $\gamma$  and single hadrons are relatively narrow, a zone of two-by-two calorimeter cells is used, large enough to contain most of the energy and small enough to avoid overlaps between

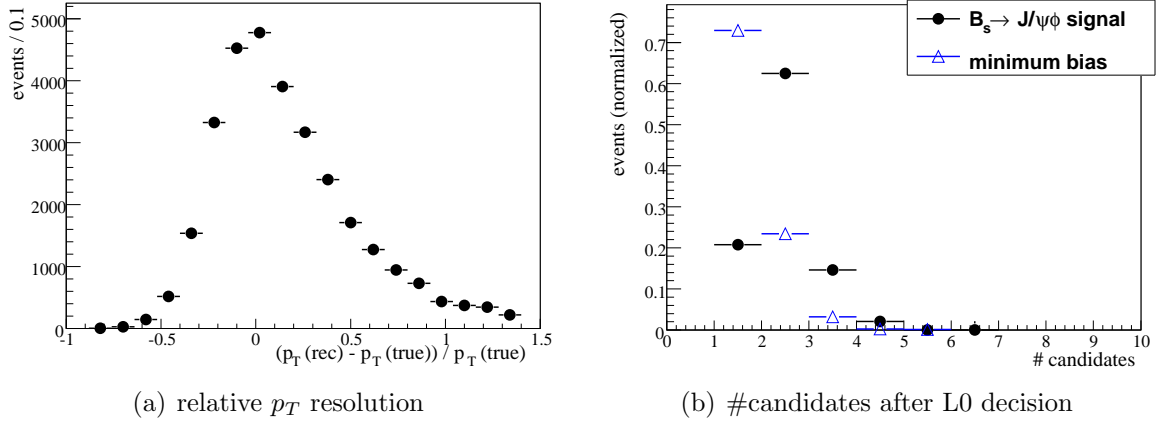


**Figure 3.2:** (a) Transverse momentum resolution of the L0 trigger candidates. The resolution (core Gaussian) is determined to be 30%. (b) Number of L0 muon trigger candidates for signal (histogram, mean: 2.1) and minimum bias (points, mean: 1.1).

**Table 3.1:** Expected L0 muon trigger minimum bias rate and efficiency. The efficiencies are measured on events which have passed the offline selection of the respective channel.

channel	L0- $\mu$	L0-di $\mu$	total
minimum bias	205 kHz	44 kHz	226 kHz
$B_s \rightarrow J/\psi\phi$	91.8 %	65.6 %	93.9 %
$B_s \rightarrow \mu^+\mu^-$	97 %	77.3 %	97.1 %
$B_d \rightarrow K^{*0}\mu^+\mu^-$	84.8 %	56.9 %	86.3 %
$B_d \rightarrow D^*\mu^+\nu_\mu$	73.5 %	15.8 %	74.3 %

different particles [59]. In case of a hadronic shower, the energy deposited in the ECal in front of the HCal is added to the candidate. For each of the candidates, the total  $E_T$  is computed. The properties of the showers together with the scintillating pad detector (SPD) and pre-shower detector (PS) information provide a first particle hypothesis. For each particle type, only the candidate with the highest  $E_T$  is kept.

### Hadronic candidates

A L0 hadron trigger is issued if the transverse energy of a cluster of hadronic type is above 3.5 GeV. This leads to a minimum bias rate of about 600 kHz.

The hardware trigger efficiency for hadronic channels is summarized in Table 3.2, it lies between 50% for two prong decays (e.g.,  $B_{(s)}^0 \rightarrow h^+h^-$ ) and 34% for four prong decays (e.g.,  $B_s \rightarrow \phi\phi$ ). This is the main source of inefficiency in the hadronic channels. This rather low efficiency comes from the similarity between signal and background events and the necessity to require tight cuts to reduce the rate.

**Table 3.2:** Expected L0 hadron trigger minimum bias rate and efficiency. The efficiencies are measured on events which have passed the offline selection of the respective channel.

channel	efficiency / rate
minimum bias	600 kHz
$B_{(s)}^0 \rightarrow h^+h^-$	50 %
$B_s \rightarrow D_s^- \pi^+$	44 %
$B_s \rightarrow \phi\phi$	34 %

### Electron, photon and $\pi^0$ candidates

The L0 electromagnetic trigger combines the information of the electromagnetic calorimeter (ECal), the pre-shower detector and the scintillating pad detector in front of the calorimeters (SPD), see Section 2.2 for details. An electron candidate is an ECal cluster with sufficient transverse energy ( $E_T > 2.6$  GeV) and measurements in the pre-shower and SPD. A photon candidate is a cluster with  $E_T > 2.3$  GeV and pre-shower but no SPD measurement. The L0 also selects  $\pi^0$  candidates, but they are currently not used in the LHC*b* trigger sequence. The above requirements reduce the minimum bias rate to 200 kHz and select signal events (e. g.,  $B_d \rightarrow K^{*0}\gamma$ ) with efficiencies of about 70 %.

### 3.1.3 Global event veto

The global event veto is a requirement on global quantities to veto high multiplicity events or those with multiple primary vertices selected from the pile-up veto. This veto system is a component of the Velo, it is made of two silicon planes, positioned upstream of the nominal interaction point. The pile-up veto provides a rejection of events with multiple proton-proton collisions through the reconstruction of all primary vertices in the event.

The cuts the total transverse energy deposit in the calorimeters, the multiplicity of the SPD detector and the pile-up information on the number of tracks in a second primary vertex (see Table 3.3) are used to select events with mostly one primary vertex. The average number of primary vertices at nominal luminosity is reduced from 1.4 to 1.1. The events that pass the veto are simpler to reconstruct and analyze, they are also less CPU time consuming to be treated in the trigger.

**Table 3.3:** Summary of the requirements of the global event veto.

Quantity	Value
Tracks in 2nd vertex	3
Pile-Up multiplicity	112 hits
SPD multiplicity	280 hits
Total ET	5 GeV

## 3.2 Online farm

After the hardware trigger decision, at a rate of 1 MHz, the full detector is read out into the Event Filter Farm (EFF) [75, 76], where the LHC*b* software trigger operates. The readout scheme, which is summarized in Figure 3.3, proceeds as follows: A positive L0 trigger decision is sent to the *Trigger and Fast Control* which sends it back to the front-end electronics of all the subdetectors. They pick up the information of the relevant events from buffers and send them through the readout network to the Event Filter Farm. The network is built of commercial gigabit Ethernet components and allows a maximum throughput of 50 Gbytes/s.

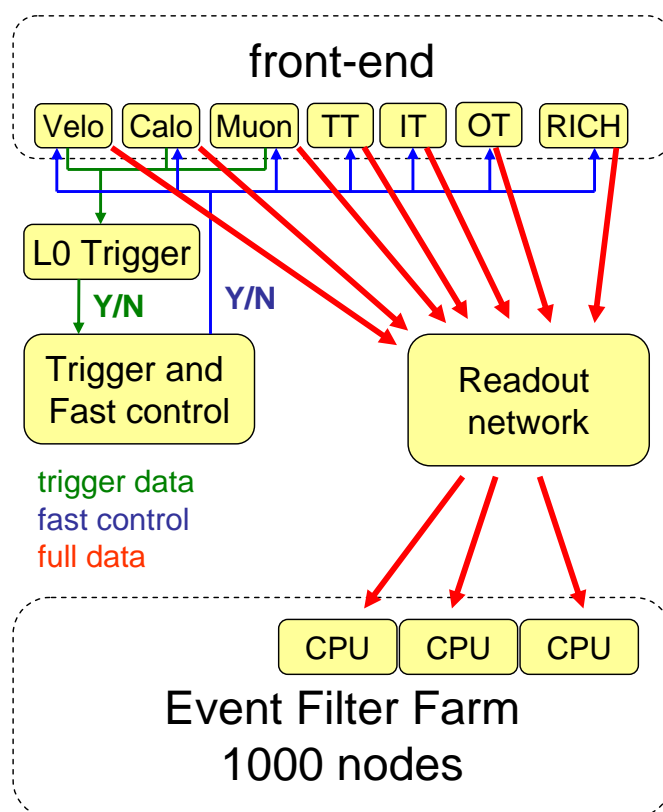


**Figure 3.3:** General structure of the detector readout: The L0 Trigger gives a (positive) signal to the Trigger and Fast Control which gives a signal to the front-end electronic of the subdetectors. The whole data is then read out via the readout network to the Event Filter Farm, on which the High Level Trigger runs.

The CPU farm is constructed from general purpose CPUs. The system is designed to be scalable to be able to adapt quickly to the actual needs. In its nominal size, the EFF consists of 1000 16-core computing nodes. This size of the Event Filter Farm defines the CPU time available for the software trigger: At an input rate of 1 MHz, the software trigger algorithms have 16 ms to process a single event on one CPU. The CPU usage of the algorithms which are evaluated in this thesis is measured on PCs with 2.2 GHz-64 bit processors, using standard LHC*b* compilation options. It is conservative to assume that the EFF will consist of CPUs of this type.

By the end of 2009, 35 % of the CPUs for the EFF will be deployed. The additional nodes will be acquired only when the rate of LHC collisions requires it, in order to obtain the most performing equipment within the available budget.

### 3.3 High level software trigger

The second and last trigger level of LHC*b*, the High Level Trigger (HLT), is a C++ software application which runs on the Event Filter Farm at a rate of 1.1 MHz on events accepted by the hardware trigger. In the HLT, the full event information is available. The size and computational power of the EFF determines the algorithms that can be run in the HLT. Ideally, one would want to run the full offline reconstruction and selection of the  $B$  candidates, but using the computing capacities of the online farm, this is not possible.

The high level trigger is divided into two levels, as sketched in Figure 3.4, named HLT1 and HLT2. The HLT1 aims at a large reduction of the background rate ( about a factor 30), performing a partial reconstruction of the event. It uses objects from the L0 trigger as seeds to define a region of interest where the reconstruction of particles is performed. This reduces the CPU time needed for decoding and pattern recognition algorithms. At the HLT1 output rate of  $\sim 30$  kHz, the HLT2 algorithms perform a full reconstruction of the events, which is as close as possible to the offline reconstruction. Several inclusive sections of  $B$  candidates are performed to reduce the rate to the final trigger output rate of 2 kHz.

Both the tracking and the vertexing in the software trigger achieve a precision comparable to what is obtained offline. E.g., for tracks traversing the whole tracking

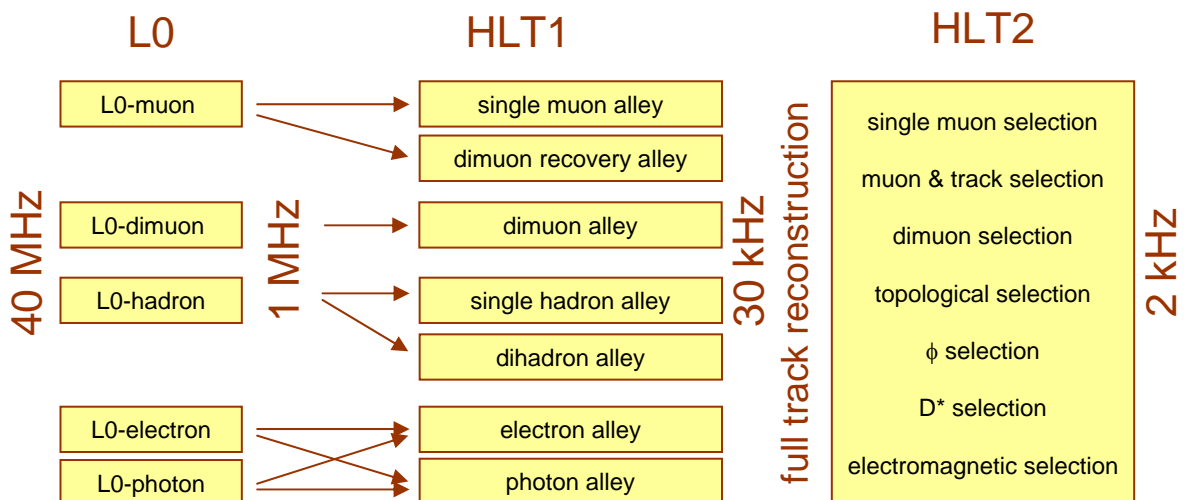


**Figure 3.4:** Overview of the LHC*b* trigger system. The HLT1 *alleys* are executed dependent on the L0 trigger type. The HLT2 selections are run for every event accepted by the previous level, independent of L0 and HLT1.

system (long tracks, see Section 2.1.5) which are fitted with a simplified track fit, a relative momentum resolution of  $\sigma_p/p \sim 0.54\%$  is obtained. The offline precision for tracks of the same momentum range is  $\sigma_p/p \sim 0.50\%$ , see also Section 5.1.

### 3.3.1 First software trigger level: Confirmation of the hardware trigger

The first level of the software trigger, HLT1, reduces the minimum bias rate from the 1.1 MHz output of the L0 trigger to about 30 kHz. It applies different sequences of algorithms, called *alleys*, dependent on the decision issued by the L0 trigger. The strategy is to confirm or discard the track assumption of the L0 trigger candidates by adding information from a tracking subdetector and applying requirements on the transverse momentum ( $p_T$ ) and the impact parameter ( $IP$ ) with respect to the primary vertex (see Figure 3.5). This step is called “L0 confirmation”. The main advantage of this scheme is that only a small number of tracks need to be reconstructed. There are currently two alternative possibilities to confirm a L0 candidate:

- with tracks from the main tracking detector (T-Stations), which is discussed in Chapter 4,
- with tracks from the vertex locator (Velo) which is described later in this section.

The two different schemes allow to set up redundant trigger selections. Currently, the Velo confirmation is used in the hadron alley and the T-Station confirmation is used in

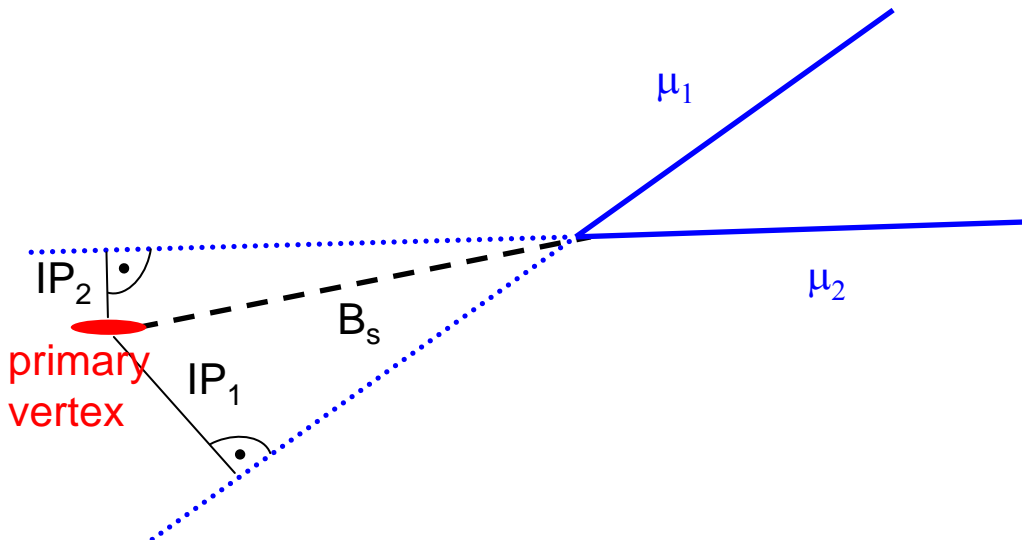


**Figure 3.5:** Determination of the impact parameter: The  $B$  meson decays at a displaced vertex into two muons. The distance of closest approach of the muon trajectory to the primary vertex is defined as the *impact parameter* of the muon with respect to the primary vertex.

the hadron (redundant to the Velo confirmation), muon and electromagnetic alley. In each implementation the algorithm which performs best on data is used.

A charged high  $p_T$  particle selected by the L0 which is confirmed by either the T-Stations or the Velo is then extended to a *long track* which passes the whole LHCb spectrometer. Further requirements on the long track quality and addition of further information is discussed for the individual implementations in the following.

For some alleys, the confirmation of the L0 object is complemented with the search of an additional track to give a better discrimination between  $B$ -decay products and background. The reconstruction of all alleys is similar.

In the following, the generic reconstruction algorithms are discussed and then the specific details of the different alleys. While the alleys are passed independently, care has been taken to avoid the double reconstruction of the same track or vertex and to save precious CPU time. For the same reason, each alley is aborted if one of the requirements is not passed by any suitable candidate.

The following confirmation alleys are currently implemented in HLT1: a *hadron alley*, a *muon alley* a second *alley* which constructs dimuons with only one L0 triggered candidate (“muon & track”) and an *electromagnetic alley*.

### Hadron alley

If the L0 trigger decision was issued by a hadronic cluster with an transverse energy above 3.5 GeV, the event is processed by the HLT1 hadron alley. Both redundant possibilities of confirming the L0 decision as discussed above are implemented. The two strategies show comparable performance on simulated data. The “T-Confirmation” with the main tracker is discussed in Section 5.2, the “Velo-Confirmation” with the vertex detector in the following.

The **Velo-Confirmation** starts with the reconstruction of 2D tracks in the  $(r, z)$  plane using only the Velo  $r$ -sensors, see Section 2.1.1. The pattern recognition algorithm searches for tracks originated from the beam line, this reduces the number of initial valid combinations of hits used as seeds to search for tracks. These tracks are then used to reconstruct the 2D primary vertices of the proton-proton interactions. The precision of these vertices is comparable with the one obtained with the offline tracks (17  $\mu\text{m}$  in  $x, y$  and 68  $\mu\text{m}$  in  $z$  [77]). The Velo 2D track reconstruction is very fast, it takes about 1 ms for all Velo 2D tracks.

The 2D tracks are then matched to the L0 candidates. In first approximation the effect of the magnet can be considered as a change in the slope of the track depending on its momentum. The matching method is based on a  $\chi^2$  quantity computed from the difference of the slope of the  $(r, z)$  velo track and the slope computed from L0 candidate. Only the candidates with a sufficiently low  $\chi^2$  are then reconstructed as 3D-track in the Velo, which is much more time consuming than the 2D track reconstruction. A similar matching with the 3D-Velo track is performed. A L0 trigger candidate which has a matched Velo track with sufficiently low  $\chi^2$  is considered to be confirmed by the Velo. The details of this method are described in reference [78].

The candidates in the confirmation are required to have a minimum impact parameter ( $IP > 0.1$  mm) and transverse momentum ( $p_T > 2.5$  GeV). This reduces the output

rate of the L0 confirmation to  $\sim 30$  kHz. On these confirmed hadrons, two trigger selections are performed:

- **Single hadron:** The single hadron selection imposes a harder cut on the  $p_T$  of the L0 confirmed track ( $p_T > 5$  GeV). This gives a robust trigger line, because the efficiency is only based on one track, but the efficiency is limited ( $\sim 20\%$ ) due to the hard selection criteria. Most of the events that pass the single hadron line, also pass the dihadron line.
- **Dihadron:** A search in the Velo is performed for tracks forming a good vertex with the confirmed L0 candidate. If such a track is found, it is then confirmed in the main tracker and the trigger selection is issued on the two track system. In this dihadron line, the companion track is required to have a significant impact parameter ( $IP_2 > 0.1$  mm) and a transverse momentum above a threshold ( $p_{T2} > 1$  GeV). The secondary vertex must be separated from the primary one and the momentum vector of the combined two tracks must point to primary vertex.

Both selections include a final part, where the track is fitted with a fast Kalman Filter based track fit, see Section 5.2.2. This step rejects badly reconstructed tracks and ghosts (pattern recognition artifacts that can not be associated to a unique particle in the Monte Carlo). In total, the hadron alley accepts about 5 kHz of minimum bias events, and the efficiency for L0 and offline selected events is 66% for  $B_{(s)}^0 \rightarrow h^+h^-$  and 52% for  $B_s \rightarrow D_s^-h^+$ . A detailed discussion of the HLT1 hadron alley can be found in Section 5.2.

### Muon alley

The HLT1 muon alley [79] is separated in two selections: a **lifetime biased selection**, which uses the impact parameter (see Figure 3.5) and secondary vertex separation to discriminate between signal and minimum bias events. This, however, modifies the  $B$  meson lifetime distribution. Secondly a **lifetime unbiased selection** where care has been taken not to select on any requirement which is correlated with the  $B$ -meson lifetime. To reduce the trigger rate, the selection criteria on the other variables are harder than in the biased selection.

The muon alley is subdivided into a single and a dimuon line. In both cases, the candidates in the muon chambers are confirmed in the main tracker (see Section 5.3 for a detailed discussion) and then extended to long tracks. The selections can be summarized as follows:

- **Single muon:** This line selects a L0 muon candidate which is confirmed to a *long track*. For the lifetime biased selection, the candidate track has to fulfill requirements on the transverse momentum ( $p_T > 1.3$  GeV) and on the impact parameter of the muon candidate with respect to its closest primary vertex ( $IP > 0.08$  mm). For the lifetime unbiased selection, there is only a higher requirement on the transverse momentum ( $p_T > 6$  GeV).

- **Dimuon:** This line starts either from a L0 dimuon trigger or from a confirmed L0 single muon candidate and adds a standalone muon track, see Section 2.3.1. The second line increases the efficiency for lower  $p_T$  dimuon candidates. In both cases, the candidates are confirmed to *long tracks* and the selection is done on the dimuon vertex (the two muon candidates have to be closer than 0.5 mm). The following criteria have to be fulfilled: for the lifetime biased selection, the tracks have to satisfy an impact parameter ( $IP > 0.15$  mm) and a soft invariant mass ( $m_{\mu\mu} > 0.5$  GeV) criteria. For the lifetime unbiased selection, a hard requirement on the invariant mass of the candidate dimuon vertex has to be fulfilled ( $m_{\mu\mu} > 2.5$  GeV).

The complete output of the muon alley is fitted with a fast track fit. The quality of the fit ( $\chi^2$ ) is used to reject bad quality tracks (ghosts) and to improve the muon identification, see Section 5.3.3. The complete muon alley selects events at a minimum bias rate of about 17 kHz with efficiencies between 80 % and 95 % on L0 triggered, offline selected events, see Section 5.3.4 for a detailed discussion.

### Muon & track alley

An alternative to the dimuon alley is the “muon & track” alley [80], which is more robust than the dimuon alley with respect to inefficiencies in the L0 hardware muon finding. It starts with a L0 triggered, confirmed single muon and adds a track forming a good vertex (distance smaller than 0.4 mm). The difference with respect to the dimuon selection is that no muon hits are required for the second track. To control the rate, the final selection is made on the secondary vertex separation ( $\Delta z > 1.5$  mm) and on the invariant mass of the two-track system ( $m_{\mu+track} > 1$  GeV). The *Muon & track alley* accepts minimum bias events with a rate of 6 kHz and select semileptonic  $B$  decays with an efficiency of 85 %– 90 %.

### Electromagnetic alley

The HLT1 electromagnetic alley [81] is dedicated to  $B$  meson decays containing a  $\gamma$  or a  $e^\pm$  in the final state. As the L0 classification of the particle as electron or photon does not always match the true type of the particle, the electron confirmation is also started for a L0 photon decision and vice versa.

To select photons, a search in the T-Stations is started for a track which matches to the electromagnetic cluster, see Section 4.1.2. If no track is found, the photon is considered as confirmed. A dedicated procedure for the removal of merged  $\pi^0$  is used [81, 82]. To the confirmed photon, two tracks with an sufficiently large impact parameter ( $IP > 0.15$  mm) which are close enough (distance  $< 0.2$  mm) are added. The HLT1 photon line selects L0 triggered signal events with an efficiency of about 70 % and reduces the background rate to 4 kHz.

To select electrons, three parallel lines are defined:

- a single electron line,
- a dielectron line with impact parameter requirements and

- a lifetime unbiased dielectron line.

The electron selections, which at present are only as prototype available, use the L0 confirmation with the T-Stations (see Chapter 4) to confirm the track assumption for the cluster in the electromagnetic calorimeter. Typical efficiencies for  $B_s \rightarrow J/\psi(e^+e^-)\phi(KK)$  are 75 % for the lifetime biased selection and 60 % for the lifetime unbiased selection. It is planned to construct also a HLT1  $\pi^0$  selection in the electromagnetic alley.

### 3.3.2 Second software trigger level: Final selections

On the output of HLT1, the second level of the software trigger, HLT2, is executed. It first performs a full event reconstruction using the forward tracking algorithm (see Section 2.1.5). The HLT2 input rate is approximately 30 kHz, depending on the CPU performance of the reconstruction software and the final size of the online farm. The HLT2 selections reduce the rate to 2 kHz, which is the final output rate of the LHC*b* trigger system.

The main difference between the HLT2 and the HLT1 selections is the different track reconstruction: in HLT1, a very limited number of candidates is reconstructed in regions of interest. In contrast to this, in HLT2, all tracks are reconstructed. In principle, one would want to use the full offline reconstruction, but due to CPU time constraints, only a fast version of the offline reconstruction is run. The HLT2 tracks differ from the offline reconstructed tracks in three points:

- In the offline reconstruction, the standalone T-Station track finding (see Section 2.1.5) is done additionally to the forward track search. This increases the reconstruction efficiency per track by 1.5 %. For timing reasons, it is not done online<sup>2</sup>.
- To clean up tracks which have been reconstructed multiple times, a clone killing algorithm is run offline. No such algorithm is run so far in HLT2.
- Finally, the offline tracks are fitted using a Kalman Filter based track fit. In HLT2, a fast track fit (see Section 5.1.2) is used. This leads to slightly less precise parameter estimate of the tracks.

Two final selections are applied: inclusive and exclusive. The exclusive selections, where a particular  $B$  decay is fully reconstructed, are specifically designed to provide the highest possible efficiency for fully reconstructed  $B$  decays of interest. As the selections require the full decay chain to be reconstructed, they suffer more from inefficiencies and imperfect calibrations in the online event reconstruction. Therefore, in the first phase of LHC running, only the inclusive selections will be used [84] and only those are discussed here. In HLT2, currently six inclusive trigger selections are foreseen which share the 2 kHz output rate.

---

<sup>2</sup>It is currently being discussed in the trigger group if the T-Station track finding can be included in the HLT2 reconstruction chain, see e. g. [83].

### Single muon selection

The single muon inclusive trigger [85] provides a high purity  $B \rightarrow \mu X$  sample that can be used to understand possible correlations of the tagging and the trigger. It provides a very large sample of events triggered independently of the B-decay “opposite” to the muon. To discriminate the large background from prompt muons, the single muon has to be required to come from a separated vertex.

This trigger is probably the simplest and most robust trigger in HLT2. The single muon trigger selects tracks which are matched to muon station hits with sufficient  $p_T$  (3 – 5 GeV) and  $IP$  (0.1 – 0.5 mm). The single muon inclusive trigger will contribute several hundred hertz to the final trigger output.

### Dimuon selection

The HLT2 inclusive dimuon selection is discussed in detail in Section 5.4. Two tracks which are identified as muons are combined to a common vertex. Two possible selections can be made:

- **lifetime biased selection:** In this selection, the muons are required to have an impact parameter with respect to their closest primary vertex ( $IP$ ). No requirement on the muons  $p_T$  and only a very low requirement on the dimuon invariant mass ( $m_{\mu\mu} > 0.5$  GeV) are made to control the rate.
- **lifetime unbiased selection:** In this selection, the rate is controlled by a rather hard requirement on the dimuon invariant mass ( $m_{\mu\mu} > 3$  GeV) and an requirement on the individual muons  $p_T$  (0.5 GeV). No selection criteria correlated with the  $B$ -meson lifetime is used.

The HLT2 dimuon selection is used for the core physics channels  $b \rightarrow J/\psi X$ ,  $B_s \rightarrow \mu^+ \mu^-$  and  $B_d \rightarrow K^{*0} \mu^+ \mu^-$ , they are selected with an efficiency of  $\sim 95\%$ . The contribution to the final output rate is of the order of 500 Hz, details can be found in Section 5.4.

### HLT2 muon & track selection:

A robust alternative to the dimuon selection is the *HLT2 muon & track* selection [85]. To one reconstructed muon, a second track (without the requirement of muon hits) is added. This selection is more robust than the dimuon selection because only one online muon is required. To control the rate, the selection has to be made on  $p_T$  (2 – 5 GeV) and  $IP$  (0.05 – 0.5 mm).

### Topological trigger selection

The topological trigger [86] selects  $B$  decays into charged hadron final states. It searches for two, three and four track combinations in a wide mass window (between 4 and 6 GeV) and is constructed such, that it triggers the signal even if one of the final state tracks is not reconstructed. This provides robustness if the online track reconstruction shows some inefficiencies. The track combinations are required to have a sufficient transverse momentum ( $p_T > 2.5$  GeV) and their vertex has to be separated from the

closest primary vertex (flight distance  $\chi^2$  larger than 100). The topological trigger selects hadronic events with an efficiency of about 80% at a rate of 800 Hz.

### $\phi$ selection

The HLT2  $\phi$  selection [87] aims to reconstruct the  $\phi \rightarrow K^+K^-$  decay. To reject the large background from wrongly reconstructed pions, it uses the PID information from the Cherenkov detectors (RICH). As the calculation of RICH rings is very time consuming, the rate is first reduced by a preselection of a separated two track vertex.

At a rate of about 1 kHz, a fast RICH particle identification algorithm [88] is used to identify kaons. The inclusive  $\phi$  selection accepts  $B$  decays with a  $\phi$  in the final state with an efficiency of about 60% and contributes to the final output rate about 200 Hz [89].

### Inclusive electromagnetic selection

The HLT2 radiative selection is currently under development. It will select electron, photon and  $\pi^0$  candidates.

The total output rate of the LHCb trigger system is 2 kHz. The bandwidth given to the individual selections will be tuned depending on the core physics channels they select [74].



# Chapter 4

## Fast track reconstruction

In this thesis, an algorithm to confirm the high  $p_T$  charged particle selected by the hardware trigger (L0) has been developed. This algorithm will be used in the *L0 confirmation* phase of the software trigger (HLT1). It needs to be extremely fast as the HLT1 input rate is 1 MHz. The total time budget of the online farm (see Section 3.2) to execute the complete software trigger algorithms of HLT1 and HLT2 is 16 ms per event at this input rate. The aim of the *L0 confirmation* algorithm developed in this chapter is to use only a minor part of this CPU time.

A track candidate in the T-Stations is searched for to confirm or discard the track assumption of the L0 object. The algorithm for this track confirmation (T-Confirmation) proceeds as follows:

- **Seed Creation:** From each L0 trigger candidate a track seed is created. Information from the seeding subdetector (electromagnetic-, hadronic calorimeter or muon stations) is used to form a track hypothesis consisting of information on the position, direction and momentum and their associated covariance matrix.
- **Hit Preparation:** Only hits in a search window consistent with the track hypothesis of a given seed are decoded.
- **Track finding:** The track finding is only performed on the limited number of hits in the search window. The standard offline track reconstruction algorithm is modified to be fast enough for the trigger application. Already at early steps of the track finding, the slopes and positions of potential track candidates are compared to the initial seed information.

This chapter describes the three steps of the track confirmation algorithm in detail for the confirmation of muon, electron and hadron candidates, followed by a summary of the performance.

### 4.1 Seed preparation

If a particle is produced in the primary interaction region, the position and direction at any point in the LHCb spectrometer, including the region after the dipole magnet,

determine the unique path of flight of the particle. In case the direction is not known, it can be reconstructed from the momentum. A region in the main tracker can therefore be determined which the particle have to cross in order to come from the primary vertex and fire the L0 trigger. This region defines a window for the track search. The size of the search window is then parameterized dependent on the properties of the L0 candidate.

The position, direction and momentum together with the parameterized uncertainties of the region of interest define a track hypothesis. To check the consistency of hits in the T-Stations with the track hypothesis, the hit position is required to agree with the estimate within a multiple of the parameterized uncertainty  $\sigma_{RMS}$ . This is done in  $x$  and  $y$ -direction. In the pattern recognition, it is furthermore checked if the slope in the  $(x-z)$  and  $(y-z)$  plane ( $t_x$  and  $t_y$  respectively) of a track candidate agrees within a multiple of the measured uncertainty of the slope with the hypothesis. To simplify the notation of the search window size, a vector  $(n_x, n_{tx}, n_y, n_{ty})$  will be used which symbolizes  $n_x$  times the parameterized resolution ( $\sigma_{RMS}(x)$ ) in  $x$  direction,  $n_{tx}$  times  $\sigma_{RMS}(t_x)$ , etc. The size of  $(n_x, n_{tx}, n_y, n_{ty})$  has to be tuned for the different use cases in the trigger. This tuning will be discussed in Chapter 5. For the rest of this chapter, the optimal values from the next chapter are taken to evaluate the performance.

In the following, the determination of position, direction and the parameterization of the search window size is studied for L0 candidates from the muon chambers, the electromagnetic and the hadronic calorimeter.

### 4.1.1 Muons

The muon stations are divided in four regions with different granularity (see Section 2.3), the finest region (R1) is closest to the beam with the highest particle density. The precision of the muon candidate thus depends on the region of the muon chambers the particle passed. Therefore, the resolution of the muon track hypothesis is determined separately for the four muon regions.

In HLT1, there are two types of muon seeds for the track confirmation, candidates from the hardware trigger (L0- $\mu$ ) and standalone muon tracks ( $\mu$ -seg), see Section 2.3.1. The tracks from the standalone algorithm can recover possible inefficiencies in the hardware trigger algorithm:

- **L0- $\mu$ :** muon candidates from the L0 trigger, which are high  $p_T$  muon tracks. The reconstruction of muon candidates in the hardware trigger is discussed in Section 3.1.1. The momentum is reconstructed from the kick in the magnetic field and has a relative resolution of  $\sigma_p/p \approx 30\%$ .
- **$\mu$ -seg:** the second type of muon seeds are muon segments, straight line tracks created by the standalone muon track reconstruction algorithm described in Section 2.3.1. This algorithm reconstructs also tracks with a lower momentum and does not use the first muon station in front of the calorimeter ( $M_1$ ) because of its high occupancy. These tracks have a momentum resolution of  $\sigma_p/p \approx 35\%$ .

The generator level momentum spectrum for both types of muon candidates is shown in Figure 4.1 (a). The L0- $\mu$  have an average momentum of 35 GeV, mainly a

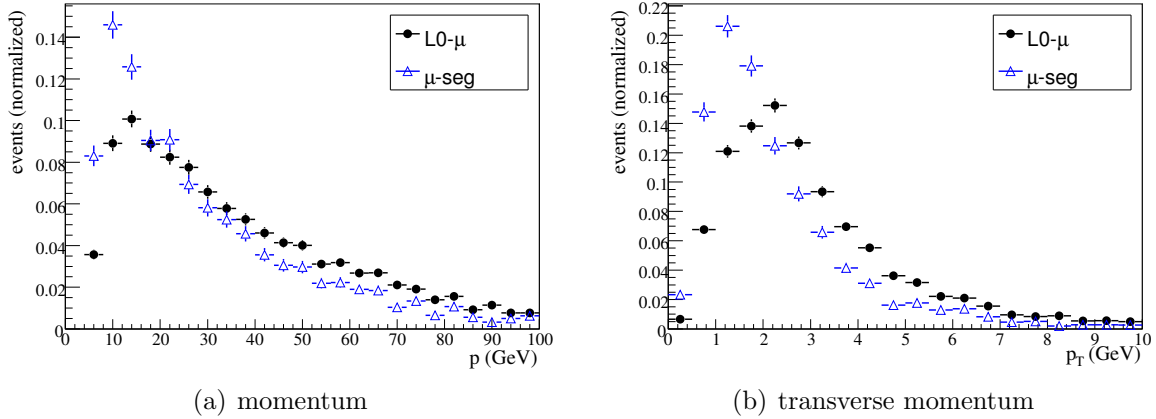


**Figure 4.1:** Momentum and transverse momentum distribution for muon candidates from the L0 trigger (L0- $\mu$ ) and from the standalone muon track reconstruction ( $\mu$ -seg). The distributions are normalized to unit area.

result of the transverse momentum requirement of 1.3 GeV applied in the hardware trigger. The muon segments have a lower average momentum, 28 GeV. The transverse momentum spectra of muons selected by both algorithms is shown in Figure 4.1 (b). For L0- $\mu$ , the cut of the hardware trigger of 1.3 GeV is seen, washed out due to the limited L0 resolution. It can be seen that the  $\mu$ -seg tracks cover the  $p_T$  spectrum for lower values. In this chapter, the resolution and performance of the T-Confirmation for these two different seed types is studied.

### Track search window

To create a seed for the track search, the position measurement of the first muon station after the calorimeters,  $M_2$ , is used. As the magnetic field in the ( $y$ - $z$ ) plane is negligible, the direction,  $t_y$ , is calculated from the slope between the measurement in  $M_2$  and the origin. For the direction in the ( $x$ - $z$ ) plane (magnet bending plane,  $t_x$ ), the difference between the hits in  $M_1$  and  $M_2$  ( $M_2$  and  $M_3$ ) is taken for L0- $\mu$  and  $\mu$ -seg respectively:

$$\text{L0-}\mu : \quad t_x = \frac{x_{M_2} - x_{M_1}}{z_{M_2} - z_{M_1}}, \quad t_y = \frac{y_{M_2}}{z_{M_2}}, \quad (4.1)$$

$$\mu\text{-seg} : \quad t_x = \frac{x_{M_3} - x_{M_2}}{z_{M_3} - z_{M_2}}, \quad t_y = \frac{y_{M_2}}{z_{M_2}}, \quad (4.2)$$

where  $x_{M_i}$ ,  $y_{M_i}$  and  $z_{M_i}$  are the coordinates of the measurement in the muon station  $M_i$ . To estimate the resolution of the track hypothesis, for the T-Station track finding, the muon seed is extrapolated to T3. It is compared to the position of the same particle on generator level. The width of their difference is a measure for the resolution of the track hypothesis.

Figures 4.2 (a, b) show the resolution in  $x$  direction for the innermost (finest) and outermost (coarsest) region of the Muon stations. Not only the position, but the slope  $t_x$  in the ( $x$ - $z$ ) plane (and  $t_y$  in the ( $y$ - $z$ ) plane) as well can be used to restrict the track search.

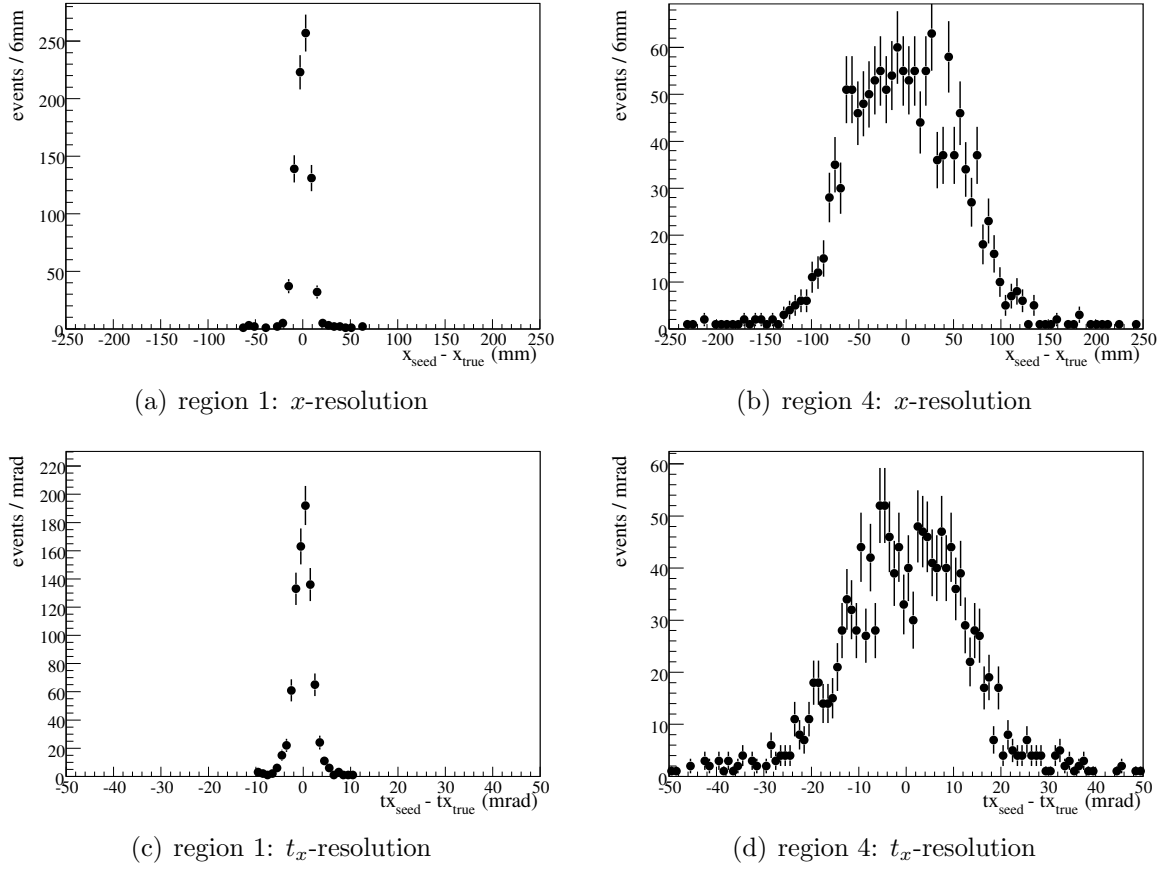


**Figure 4.2:** Resolution of the L0- $\mu$  muon track hypothesis in T3. Shown is the resolution in  $x$ -direction and slope ( $t_x$ ) for muon tracks from the region with the finest and coarsest granularity.

**Table 4.1:** Resolution of the muon track hypothesis at T3. The resolutions are given for L0- $\mu$  (with  $M_1$  hits) and muon segment tracks ( $\mu$ -seg, without  $M_1$  hits). The L0- $\mu$  have a better resolution because the muon station in front of the calorimeters compensates the effect of multiple scattering.

	Region 1		Region 2		Region 3		Region 4	
	L0- $\mu$	$\mu$ -seg						
$x$ [mm]	8	45	15	80	29	120	54	200
$y$ [mm]	8	10	12	15	22	30	48	61
$t_x$ [mrad]	3	7	4	13	7	20	13	32
$t_y$ [mrad]	4	3	6	5	8	6	10	8

Figures 4.2 (c, d) show the slope resolution of the track hypothesis at T3 for the same two muon regions. The RMS values of the resolutions in  $x$ ,  $y$ ,  $t_x$ ,  $t_y$  are summarized in Table 4.1. The resolution of a L0- $\mu$  is generally better than for a  $\mu$ -seg track because the higher average momentum makes the effect of multiple scattering less important. In addition, the measurements of  $M_1$  improve the resolution because the multiple scattering in the calorimeter can be compensated.

### 4.1.2 Electrons and photons

Similar to the muon stations, the electromagnetic calorimeter (ECal) is divided in regions with the readout granularity decreasing to the outside of the detector. The three regions are called: inner part, middle part and outer part.

The L0 electron candidate consists of a four cell cluster in the ECal. The center of gravity of the two-by-two cluster is calculated by the L0 preprocessor, see Section 3.1.2. The calculated position in relative coordinates of a cell, as a function of the true position of the MC particle is shown in Figure 4.3 (a). An S-shaped deformation from the ideal straight line is clearly visible. This degrades the resolution. In order to improve the position measurement, the shape is parameterized with a tangent as a function of the relative position inside the cell. Using this function, the measured position is corrected. Fig. 4.3 (b) shows the corrected relative position versus the true position of the cluster. The deformation is removed. Table 4.2 summarizes the position resolution of the uncorrected and corrected two by two clusters in the ECal. The improvement due to the S-shape correction is clearly visible.

To provide a track hypothesis from the ECal cluster, the particle direction has to be determined. The curvature of a particle in the magnetic field is inverse-proportional to its momentum, which can be approximated by the cluster energy. The curvature can

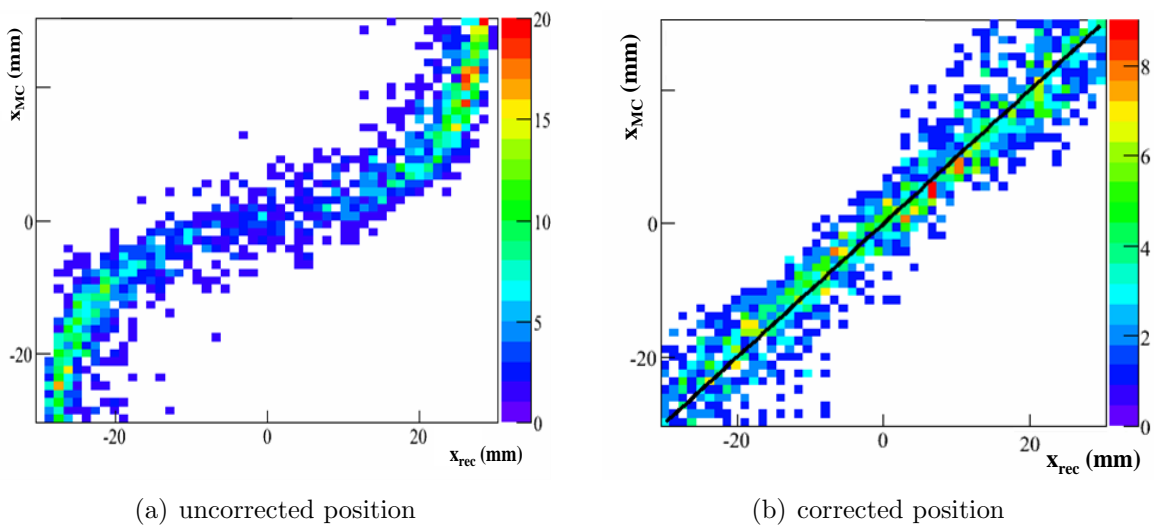


**Figure 4.3:** True position versus reconstructed position in relative coordinates of a cell in the middle part of the ECal. (a) Barycenter calculated from the two-by-two cluster. (b) Position after the correction for the S-shape.

**Table 4.2:** Resolution of the electron track hypothesis at the ECal. Uncorrected denotes the barycenter of the two-by-two cluster, corrected shows the improved resolution after the S-shape correction.

		ECal inner	ECal middle	ECal outer
uncorrected (mm)	x	5.4	8.8	21
	y	5.5	9.4	21.5
corrected (mm)	x	2.8	5.0	13
	y	3.0	5.0	13

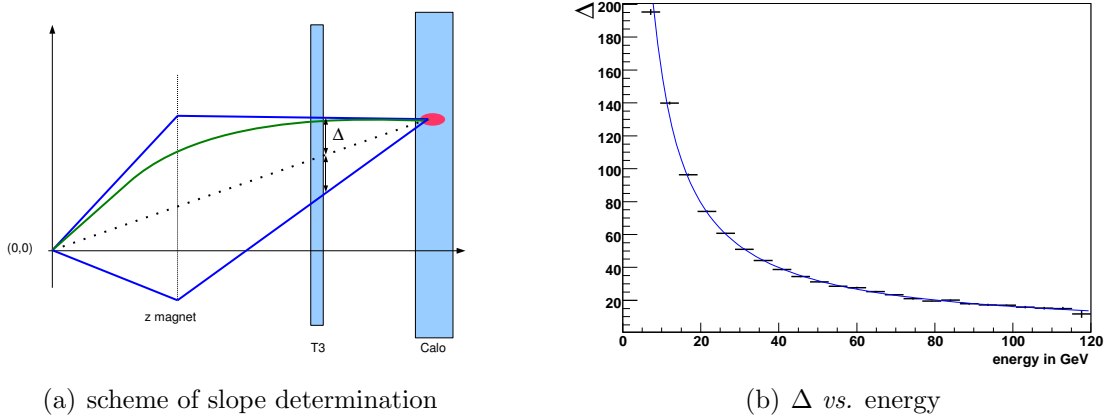
therefore be approximated from the energy deposit in the calorimeter. The influence of the field is parameterized as a single kick at the center of the magnet. Fig. 4.4 (a) sketches the idea: The difference between the curved particle path (green) and the straight line to the origin (black, dotted) is called  $\Delta$ . The track hypothesis can now be approximated by two straight lines (blue) from the cluster to the focal plane. Of course, two track hypotheses have to be made for the two charge assumptions.

Fig. 4.4 (b) shows the measured values of the distance  $\Delta$  as a function of the cluster energy for electrons in minimum bias events. The function:

$$\Delta = \frac{\alpha}{E_{cluster}} \quad (4.3)$$

is fitted to the data, where  $\alpha$  denotes the proportionality constant. The assumption that the curvature and cluster energy are inversely proportional works well.

From this parameterization, two directions can be assigned to the ECal cluster yielding to an estimate of the position and slope at the tracking stations. As the charge



**Figure 4.4:** (a) Momentum kick method to determine the direction for a cluster (see text for a explanation) and (b) the parameterization of  $\Delta$  as a function of the cluster energy. A  $1/E$  function has been fitted to the data.

**Table 4.3:** Resolution of the electron track hypothesis extrapolated to T3.

	ECal inner	ECal middle	ECal outer
$x$ (mm)	3.5	5.5	15
$y$ (mm)	5	7	12
$t_x$ (mrad)	3	3	8
$t_y$ (mrad)	5	7	8

of the particle is unknown, two search windows for both charge assumptions have to be opened. The parameterization of the particle trajectory between T3 and T1 is as described in Section 4.1.4. The resolution of the track hypothesis at T3 is summarized in Table 4.3.

### 4.1.3 Hadrons

The hadronic calorimeter (HCal) is divided in two regions, inner part and outer part, the granularity of the outer part is coarser by a factor of two.

The L0 hadron candidate is a four cell cluster in the hadronic calorimeter. The position of the barycenter of the cluster is calculated in a similar way as for the ECal seed. A S-shaped bias in the reconstructed versus true cluster position is observed. However, the granularity of the HCal has shown to be too coarse to correct this bias.

In order to utilize the better resolution of the electromagnetic calorimeter in front of the HCal, the beginning of the hadronic shower in the ECal is used. Therefore, the barycenter is extrapolated to the ECal, using a straight line to the origin. In the ECal, the hits of three-by-three cells around the extrapolated cluster position are processed. In these nine cells, a search for an energy deposit is initiated. The cell center is required to be no further than one cell size (in both  $x$  and  $y$  direction) from the extrapolated shower position, giving a maximum of four active cells, see Fig. 4.5. If more than two of these carry energy, the cluster position is determined from the ECal. This gives a

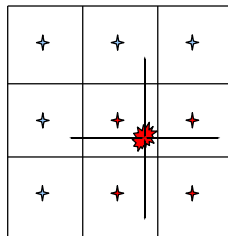


**Figure 4.5:** Sketch of the three-by-three ECal cells in front of the HCal. The red star is the cluster position extrapolated from the HCal. The four arrows show the distance of 1 cell size from the extrapolation. All 9 ECal cells shown are decoded. For the position measurement, only the four lower right cells are used since their center lies within  $\pm 1$  cell size of the extrapolation.

total of five different regions of granularity of the calorimeters: HCal+ECal with three regions and the inner and outer part of the HCal.

The hit preparation of the ECal and HCal to refine the position measurement takes about 0.4 ms. It has to be seen on data if the advantage of the better position measurement (smaller search windows and hence faster track reconstruction) overcompensates the extra time spent. In the current simulation, the time saved in the track reconstruction exactly balances the extra decoding time. Hence, the simpler algorithm without the calorimeter decoding is used.

Analogously to the ECal seed preparation, the dependence between cluster energy and curvature in the B field is used to calculate the direction of flight from the calorimeter cluster. Two different parameterizations are used, dependent whether enough energy is deposited in the electromagnetic calorimeter or not. The offset  $\Delta$  is parameterized as a function of the HCal energy only for the first case and as a function of both HCal and ECal energy for the latter. The resolution for the five regions is summarized in table 4.4.

**Table 4.4:** Resolution of the hadron track hypothesis at T3. The first three columns describe the case when the ECal in front of the HCal is usable for position determination. If the calorimeter are not decoded, only the last two columns are relevant.

	HCal	HCal	HCal	HCal inner	HCal outer
	ECal inner	ECal middle	ECal outer		
$x$ (mm)	30	31	61	31	100
$y$ (mm)	26	29	44	26	51
$t_x$ (mrad)	17	13	16	15	21
$t_y$ (mrad)	10	8	18	11	34

#### 4.1.4 Seed extrapolation

The extrapolation of the seed information for the track search is done in two steps, assuming that the particle originates from the nominal interaction point:

- first, the seed is extrapolated linearly from the L0 seeding subdetector (muon stations, ECal or HCal) to T3. This is possible as the magnetic field after the T-Stations is negligible (see Figure 2.3).
- inside the T-Stations, the magnetic field is non-negligible. Therefore, the seed information is transported using a parabola in  $x$ -direction and straight line in  $y$ -direction. The curvature  $m_x$  of the parabola is inverse proportional to the momentum of the particle and can be parameterized (using generator level information, analogously to Figure 4.4) as:

$$m_x = \frac{q}{p} \frac{1}{42.0}. \quad (4.4)$$

Using this two step extrapolation of the seed information, it can be decided for each individual hit if it is consistent with the seed information. This is used in the hit decoding and the track finding steps discussed in the following.

## 4.2 Hit preparation in the search window

It is impossible to process all detector information at the HLT1 input rate of 1.1 MHz. For example, to provide all  $\sim 3800$  hits in the full Inner Tracker (IT) and Outer Tracker (OT) to the track finding algorithms takes about 5 ms per event<sup>1</sup>, clearly too slow for this application. Therefore, only the detector information is processed which lies inside the region of interest which is calculated according to the seed preparation, Section 4.1. To avoid the time intense loops over several thousands of hits, the hit preparation is done in two steps: first, the detector data is processed to a data object which contains only the channel ID and, for the OT, the drift time information (“data decoding”). In the second step, the data objects used by the pattern recognition algorithms are created (“hit creation”). They contain the geometry information and drift distances including calibration and alignment.

### Data decoding

Only the detector data in the region of interest defined by the L0 candidate is processed: If the region of interest overlaps with the acceptance of the Inner Tracker, the whole data from the IT is decoded. Because this decoding is already very fast ( $\sim 0.1$  ms), it is not further subdivided.

If the region of interest overlaps with the acceptance of the OT, it is checked which half-module (see Section 2.1.4) overlaps with it. The OT consists of 432 such half modules, independent read out units providing the data of 128 channels. To avoid time intensive use of the geometry database, the module geometry is saved to memory before the event processing starts. Half modules which overlap with the region of interest are decoded to fast hit containers. This procedure reduces the number of half modules which have to be processed by a factor of five to ten, depending on the precision of the seeding L0 candidate. This reduces the average number of hits which are processed from  $\approx 3800$  to 500-1000. The number of hits is not reduced by the same factor as the number of modules because most hits are located in the few innermost modules.

### Hit creation

Among the decoded hits, those consistent with the track hypothesis are selected. The data objects used by the pattern recognition algorithms are created. The average number of hits which are finally created is shown in Table 4.5 for the different use cases in HLT1 together with the complete time for data decoding and hit creation. As an example, the number of hits created for the single muon confirmation is shown in Figure 4.6 (a) together with the total number of T-Station hits in the event. Instead of an average of 3800 hits per event, only 270 hits have to be accessed for track finding.

---

<sup>1</sup>The CPU time given here is the time for complete hit preparation and for the selection of hits which lie in the search window.

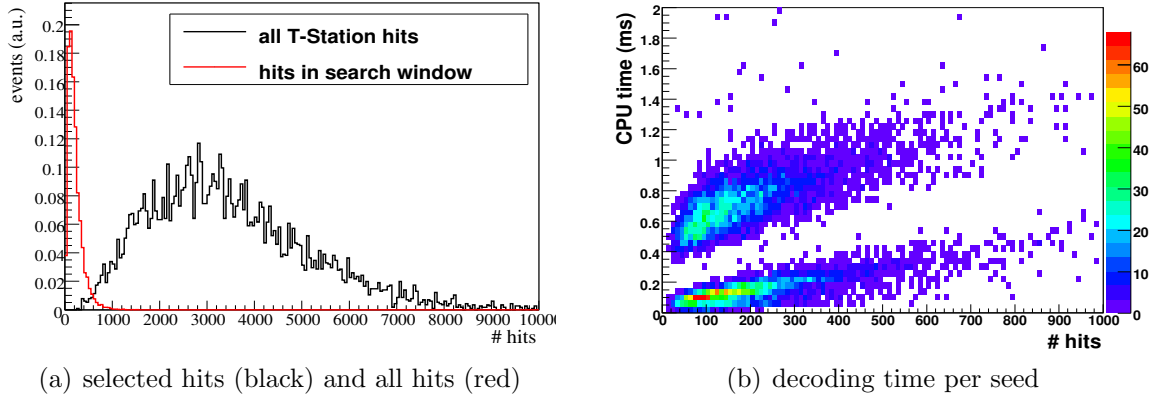


**Figure 4.6:** Hit Preparation in the *single muon alley*: (a) The black histogram shows the number of T-Station hits per event (mean: 3800), the red histogram shows the number of hits which agree with the track hypothesis (mean: 270), normalized to unit area. (b) The complete hit preparation time per seed as a function of the number of hits in the search window (mean decoding time: 0.7 ms per seed). The shape of the decoding time is discussed in the text.

Figure 4.6 (b) shows the complete time for data decoding and hit creation as a function of the number of selected hits in the single muon confirmation, the mean decoding time is 0.7 ms. It rises linearly with the number of hits. The decoding time shows two separate regions. The higher decoding time is needed for the first track in the event where the data decoding has to be done, this explains the offset of 0.4 ms. As most of the tracks occupy the innermost modules, the second track confirmation in an event profits from the already decoded data. Its decoding time now lies around 0.15 ms (no offset).

**Table 4.5:** Average number of hits consistent with the track hypothesis for the different use-cases in the track confirmation. The CPU time for module decoding and hit creation is also given. The search window sizes for this table are taken from the optimization presented in Chapter 5. For the electron and hadron case, both track hypothesis are added in the table.

	muon		electron	hadron
	L0- $\mu$	$\mu$ -seg		
#modules	80	110	40	100
#hits	270	800	100	540
decoding time (ms)	0.7	1.0	0.5	0.8

The two step procedure which is presented here gives a significant improvement from 5 ms hit preparation and selection time to 0.5 – 0.8 ms for the decoding and creation of hits on demand. This procedure is implemented in the standard LHCb track reconstruction framework and is used by all HLT1 applications.

## 4.3 Track finding

The track reconstruction is performed in each search window separately on the corresponding selection of hits. Currently, two offline algorithms for standalone T-Station track finding in the complete Inner and Outer Tracker are competing: `TsaSeeding` [90, 91] and `PatSeeding` [92]. Both algorithms show comparable results on the simulation and dependent on their performance on data, the standard LHCb T-Station pattern recognition algorithm will be chosen.

In close collaboration with the authors, both algorithms have been modified for the HLT1 track finding. They have been modified to profit most from the known information on position and direction from the hardware trigger candidate (see Section 4.1). As both algorithms follow the same principal idea, first the basic pattern recognition idea will be discussed and then the modifications made for the trigger usage are highlighted. Finally, the performances of both restricted track finding algorithms are compared.

### 4.3.1 Principles of T-Station track finding

The algorithm searches for tracks first in the  $(x-z)$  projection, then a consistent track segment in the  $(y-z)$  projection is searched for to construct a full 3D track. The track search is done separately for the inner tracker (IT) and outer tracker (OT) with a similar general strategy. In the following, only the reconstruction in the OT will be described which is more challenging due to the relatively big cell size (an OT straw has 5 mm diameter with a length of 2.5 m) and the drift time ambiguity each measurement has; from a measurement of the drift time, it is not clear on which side of the anode the particle passed.

The search for track candidates in the  $(x-z)$  projection proceeds as follows: First, every possible line is constructed between hits in the  $x$ -layers of T1 and T3. Each of these lines is processed separately as starting point for the track candidate search. The slope of this line ( $s_x$ ) is required to be consistent with tracks from the interaction region. Now, all measurements with a  $x$ -position within 1 cm of this line are selected (see Figure 4.7), the OT drift time is not taken into account.

As second step, a hit in T2 which was selected in the previous step is chosen. Due to the non-negligible fringe field, a parabola is then constructed from the hits in T1, T2 and T3. Around this parabola, a second, tighter window is opened. At this point, the drift time ambiguities are resolved. There are in total eight possibilities to construct a parabola out of three hits with a two fold ambiguity each. For each combination, the number of measurements falling in the tighter window is counted, the combination with the most hits is chosen (see Figure 4.8). The procedure explained above is repeated with all  $x$ -hits in T2.

To clean up the track candidates, the parabola is re-fitted and the drift time ambiguities can change if they improve the  $\chi^2$  of the fit. If the worst hit is more than  $3\cdot\sigma$  away from the parabola, it is removed. Before the candidates are passed to the stereo hit search, they are required to pass another set of selection criteria (e. g., on  $t_x$  or on the number of hits).

The stereo search uses the  $(x-z)$  track candidate and searches for stereo hits which overlap in  $x$ -direction, see Figure 4.9. Using the  $x$ -position of the  $(x-z)$  candidate,

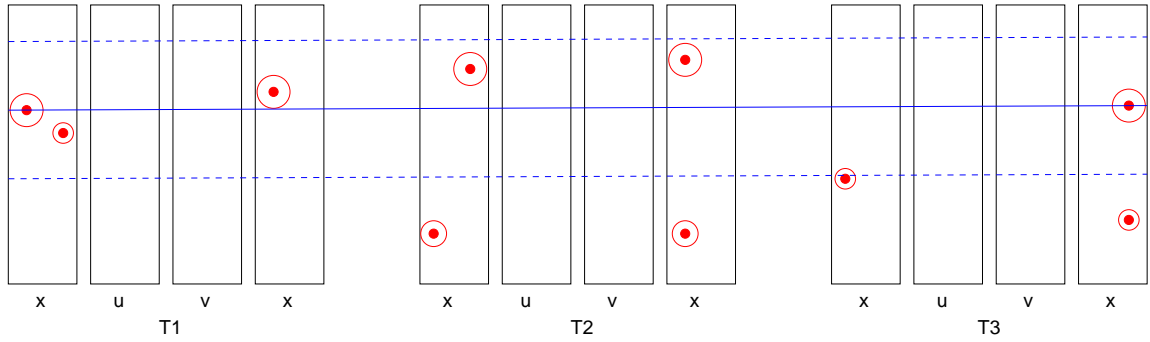


**Figure 4.7:** First search window in the  $(x-z)$  plane for the OT. The anode wires are indicated with a solid red dot, the circles are the corresponding drift distances calculated from the measured drift times. A straight line is constructed from two  $x$ -measurements in T1 and T3. All measurements inside a 1 cm search windows are further used by the algorithm. (Figure from [93].)

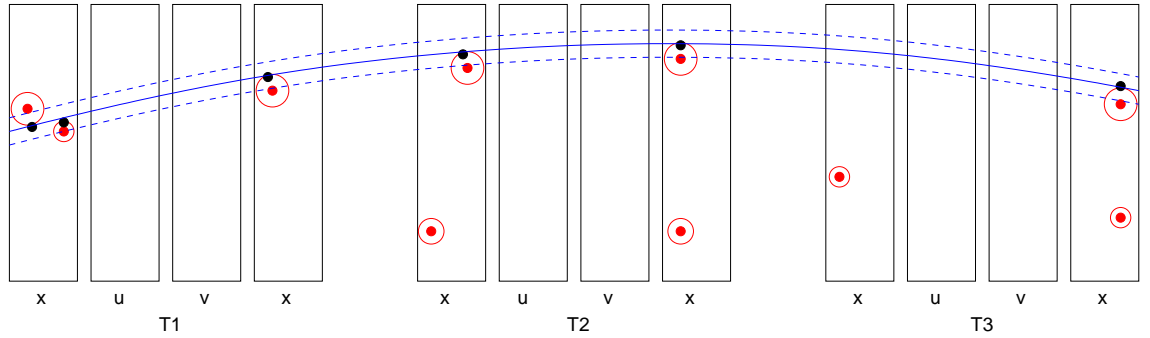


**Figure 4.8:** Curved search window in the  $(x-z)$  plane for the OT: A measurement in T2 is selected. To resolve of the drift time ambiguities, eight parabolas are constructed for the different combinations of the drift radii from the three selected measurements. The measurements (black dots) inside a tighter window around the parabola (dashed line) are counted, the parabola with the most measurements is chosen. (Figure from [93].)

a  $y$ -position is estimated for each stereo measurement. The stereo track candidate search is performed analogously to the  $(x-z)$  search, however, the track candidate is approximated by a straight line due to the negligible curvature in  $y$ -direction. Additional uncertainties from the conversion from the stereo coordinates to  $y$  are taken into account. Ambiguities are solved as in the  $x$ -search, the combination with the most measurements is kept. As additional constraint, the candidate slope ( $s_y$ ) is required to roughly point to the origin. At this stage, the candidate is again required to satisfy some criteria, e. g., on a minimum number of hits.

The number of candidates found at this stage by far exceeds the number of real particles leaving tracks in the detector: The algorithm finds several track candidates per particle and as well a significant amount of candidates do not belong to any particle. To select only the best candidates, a quality criterion is introduced. This criterion differs for the two pattern recognition algorithms available and will be discussed in the respective section. The track candidates are sorted by decreasing quality and the

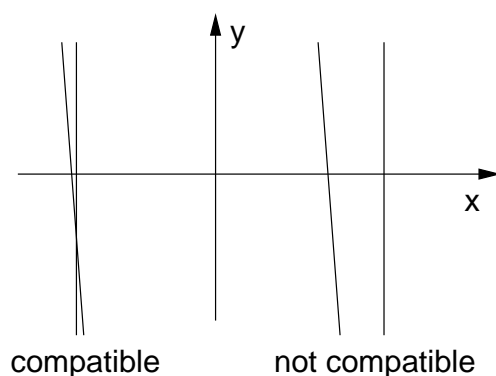


**Figure 4.9:** Selection of matching hits for the stereo search. Hits in the Outer Tracker straws in  $x$  and stereo layers are compatible if they overlap in the  $(x-y)$  projection (left) and incompatible if they do not (right). (Figure from [93].)

algorithm only selects the best ones. It is furthermore checked that the candidates do not share too many measurements with other selected candidates.

### 4.3.2 Algorithm tuning for trigger tracking

Before the track search is started, it is checked if a minimal number of hits lies within the track hypothesis: If the track hypothesis overlaps with the IT, 7 out of 12 hits are required. Otherwise, 14 out of the maximum of 24 hits in the OT are required to start the track finding. These very loose requirements are 100 % efficient and ensure that no unnecessary track search is started.

The search windows opened by two different track hypotheses may overlap such that the same track may be reconstructed twice. This is especially important in the case of calorimeter seeded track search, where two search windows are opened for the two charge assumptions. To avoid the same track being reconstructed a second time (“a clone”), it is checked for tracks which agree in their  $x$  and  $y$ -position both in T1 and T3 better than  $10\ \mu\text{m}$ . This very hard cut only removes tracks with identical hit content and has no cost in efficiency.

#### Tuning of the TsaSeeding algorithm

In the  $x$ -search of TsaSeeding algorithm [90, 91], pairs of hits in the first and last stations are used to define a straight line in the  $(x-z)$  plane, which is later replaced by a parabola. Instead of the generic criterion applied in the TsaSeeding algorithm to restrict the slope  $s_x$  between the two hits ( $|s_x| < 0.8$ ), the slope between the pair is required here to agree within  $n$ -times the  $\text{RMS}(t_x)$  of the extrapolated slope from the L0 candidate. This reduces the number of track candidates at the earliest stage.

In the stereo search, similar to the  $x$ -search, pairs of hits in the first and last station are combined to define a line candidate. By default, the slope of the line candidate ( $s_y$ ) is required not to differ more than 0.1 from the slope of the straight line obtained by connecting the first hit of the cluster with the origin. Additionally, in the algorithm tuning for the trigger, the slope of each hit with respect to the origin is required to

agree within  $n$ -times the RMS value of  $t_y$  with the extrapolated slope from the L0 seed. Without the restrictions from the track direction, the selection of track candidates is best taken with a track likelihood based on a combination of the number of observed and of expected hits and the  $\chi^2$  of a first track fit. The calculation of the likelihood, however, is very time consuming (for details, see Reference [90]). In the restricted pattern recognition studied here, the calculation of the likelihood becomes obsolete since the number of candidates is reduced. It can be replaced by simple sorting according to the reduced  $\chi^2$  of the parabola fit without any loss of efficiency.

### Tuning of the PatSeeding algorithm

The `PatSeeding` algorithm has been developed with a special focus on the algorithm execution time. For example, the search for “complicated” candidates, e. g. those with a large  $|y|$  or tracks migrating from the IT to the OT is consequently postponed after the normal track search. This allows harder selection criteria in the first step and thus reduces the number of candidates which have to be processed with wider cuts. In the offline usage on the full T-Stations, the `PatSeeding` algorithm is slightly more efficient than the `TsaSeeding` algorithm and performs 40 % faster.

In close collaboration with the author, the information on position and direction from the hardware trigger candidate has been implemented in the `PatSeeding` algorithm. It is used as additional requirement in each step of the algorithm when the candidates are required to be consistent with the specified limits. The formalism to use the constraints is as follows (see Reference [92]):

The information on position and direction of a track at a given point  $z_0$  is summarized in a state  $\vec{S}(z_0)$ :

$$\vec{S}(z_0) = \begin{pmatrix} x \\ y \\ t_x \\ t_y \end{pmatrix} (z_0). \quad (4.5)$$

The search window which is calculated from the L0 seed is saved in the covariance matrix  $C(z_0)$ , which is given at the end of T3,  $z_0 = 9340$  mm:

$$C(z_0) = \begin{pmatrix} n_x^2 \times \sigma_{RMS}(x)^2 & 0 & 0 & 0 \\ 0 & n_y^2 \times \sigma_{RMS}(y)^2 & 0 & 0 \\ 0 & 0 & n_{t_x}^2 \times \sigma_{RMS}(t_x)^2 & 0 \\ 0 & 0 & 0 & n_{t_y}^2 \times \sigma_{RMS}(t_y)^2 \end{pmatrix} (z_0), \quad (4.6)$$

with multiples of the parameterized search window sizes (see Section 4.1) on the diagonal elements. This ansatz neglects correlations between the four dimensions of the search window. Then, the search window at any point in the T-Stations is calculated using the following transport formula, where the state  $\vec{S}(z_0)$  is the extrapolated position from

the L0 seed:

$$\vec{S}(z) = P(z - z_0)\vec{S}(z_0), \quad (4.7)$$

$$C(z) = P(z - z_0)C(z_0)P^T(z - z_0), \quad (4.8)$$

where  $P(z - z_0)$  is the matrix that transports the state over a distance  $z - z_0$ :

$$P(z - z_0) = \begin{pmatrix} 1 & 0 & z - z_0 & 0 \\ 0 & 1 & 0 & z - z_0 \\ 0 & 0 & 1 & 0 \\ 0 & 0 & 0 & 1 \end{pmatrix}, \quad (4.9)$$

that is, the search window gets transported linearly within the T-Stations. The search window size  $\sigma$  around the center is given by the square root of the elements on the diagonal of the covariance matrix at  $z$ :

$$\sigma(x) = \sqrt{c_{11}}, \quad (4.10)$$

$$\sigma(y) = \sqrt{c_{22}}, \quad (4.11)$$

$$\sigma(t_x) = \sqrt{c_{33}}, \quad (4.12)$$

$$\sigma(t_y) = \sqrt{c_{44}}, \quad (4.13)$$

where  $c_{ii}$  are the elements of the covariance matrix  $C(z)$ , Equation 4.8. Hits are only picked up in the region given by above formulae, and at every step, the slopes resulting from the combination of hits are checked for consistence with the limits specified. This method makes optimal usage from the seed information inside the track finding algorithm.

### 4.3.3 Performance comparison of trigger tracking algorithms

To compare the performance of both tracking algorithms, the track finding is analyzed for the T-Confirmation step in the HLT1 single muon alley (the other trigger implementations show similar results). The search window sizes are tuned for both algorithms separately, according to the procedure described in Chapter 5. The result of this comparison is summarized in Tab. 4.6.

**Table 4.6:** Comparison of the performance of `PatSeeding` and `TsaSeeding` for T-Confirmation in the HLT1 single muon alley, all performance figures are per seed. The search window sizes for this table are taken from the optimization presented in Chapter 5.

	PatSeeding	TsaSeeding
reconstruction efficiency	96.4 %	96.1 %
reconstructed tracks	1.15	1.5
track finding time (ms)	0.35	0.7

The `PatSeeding` algorithm reconstructs tracks slightly more efficient than the `TsaSeeding` algorithm. The better implementation of the restricted track search results in a lower number of candidates. The biggest difference between the two algorithms is in the CPU time, it is 50% lower for the `PatSeeding` algorithm.

For these reasons, the `PatSeeding` algorithm has been chosen as the default track finding algorithm for the L0 confirmation in HLT1. In the remaining part of this thesis, the `PatSeeding` algorithm will be used.

## 4.4 Performance

The important characteristics of the performance of the T-Confirmation are the efficiency to reconstruct a track belonging to the L0 candidate, the number of tracks found per candidate (purity), the momentum resolution and the algorithm execution time.

The performance of the track confirmation has to be optimized separately for each use case to find the best compromise between high efficiency and low execution time. This optimization in terms of the parameterized resolution is discussed in Chapter 5 where the implementation of the track confirmation in the software trigger is presented. The performance figures shown here are obtained with the search window configurations which were found to be optimal in the tuning from Chapter 5, they are summarized in Table 4.7.

The number of reconstructed tracks and the CPU time is measured on minimum bias events. Details on the used datasets are discussed in Section 2.4. The reconstruction efficiency is determined on simulated events of the following type:

- for the muon performance, simulated  $B_s \rightarrow J/\psi(\mu^+\mu^-)\phi(KK)$  events,
- for the hadron performance, simulated  $B_d \rightarrow \pi^+\pi^-$  events and
- for the electron performance, simulated  $B_s \rightarrow J/\psi(e^+e^-)\phi(KK)$  events.

**Table 4.7:** Optimized search window sizes (from Chapter 5) for each use case of the T-Confirmation. The configuration for electron seeds has not yet been optimized as the implementation is only as prototype available.

type	optimal configuration
	$n \cdot \sigma$ (x,tx,y,ty)
L0- $\mu$	(7,4,8,8)
$\mu$ -seg	(6,8,8,10)
Hadron	(3,3,4,4)
Electron	(5,5,5,5)

### Efficiency and number of reconstructed tracks

The generated particles (MC particles) are required to satisfy the following acceptance criteria:

- the MC particle associated to the seed object is required to be of the same type as the trigger object, i. e., muon, charged hadron or electron respectively,
- it is flagged as reconstructible (at least 1  $x$  and stereo hit per T-Station) and
- the production vertex of the particle is within 50 cm of the origin (0,0,0).

The efficiency as well as the average number of reconstructed tracks per seed is summarized in Tab. 4.8. In the single muon confirmation (L0- $\mu$ ), the efficiency is shown in Figure 4.10 (a) as a function of the momentum, integrated over the whole momentum range, it is 96.4 %. On average, 1.15 tracks are reconstructed per seed. In the muon segment confirmation ( $\mu$ -seg), the search windows are larger due to the absence of  $M_1$ ; the efficiency is 95 %. The efficiency is lower because the resolution distribution of the track hypothesis has large tails which have to be cut at some point to keep the execution time within reasonable limits. As the track hypothesis is less restrictive, on average 5 tracks are reconstructed per seed.

The efficiency to reconstruct tracks belonging to a L0 hadron trigger is shown in Figure 4.10 (b), it is on average 96.6 %. The efficiency to find a track coming from an electron L0 trigger is 95.8 %.

The main gain of the T-Confirmation of electron candidates is the distinction between electron and photon candidates: For true electrons, 1.02 tracks are reconstructed per calorimeter seed, as shown in Figure 4.11 (a). For true photons, in 90 % of the calorimeter seeds, no track is reconstructed, see Figure 4.11 (b). This information can be used for a track confirmation of the electron hypothesis and for a track veto of the photon hypothesis.

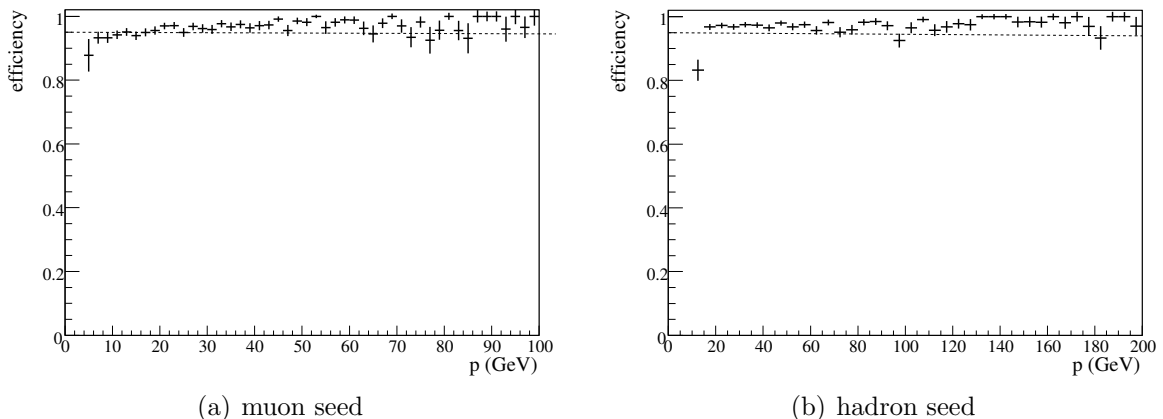


**Figure 4.10:** Track reconstruction efficiency versus momentum (a) for  $B_s \rightarrow J/\psi\phi$  signal events in the *single muon confirmation* with the configuration (7/4/8/8) (b) for  $B_d \rightarrow \pi^+\pi^-$  signal events in the *hadron confirmation* with the configuration (3/4/3/4). The horizontal line indicates 95 % efficiency.

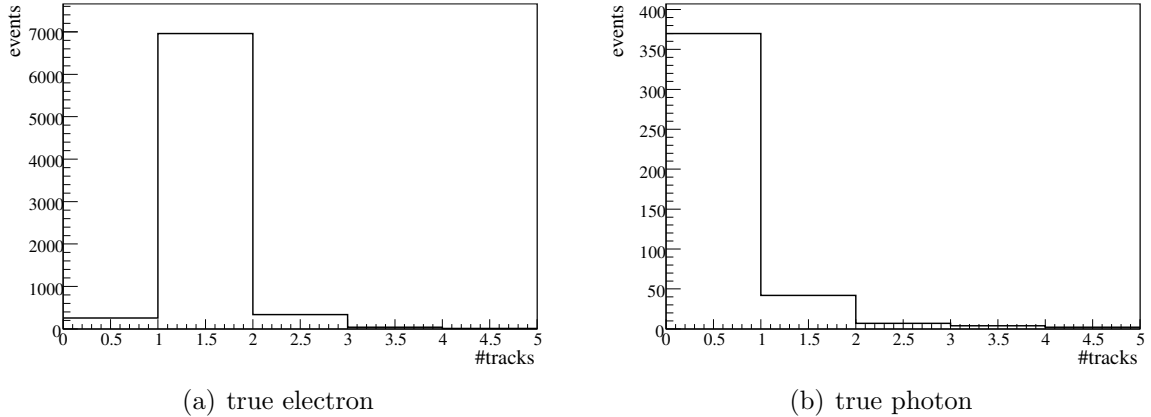


**Figure 4.11:** Number of reconstructed tracks in signal  $B_s \rightarrow J/\psi(e^+e^-)\phi(KK)$  events for a L0 electron trigger candidate which is caused by a generator level (a) electron and (b) photon.

### Transverse momentum resolution

The transverse momentum ( $p_T$ ) resolution is determined on MC particles which fulfill the same acceptance criteria as those used for the efficiency measurement. Fig. 4.12 (a) shows the resolution of the transverse momentum ( $p_T$ ) in black as it is available in the L0 muon trigger and in yellow for the corresponding track reconstructed in the T-Confirmation. The resolution is greatly improved from 30% of the candidate from the hardware trigger to 3.4% (core resolution, the *RMS* is 5.4%) for the reconstructed track.

The  $p_T$  resolution of the track reconstructed from muon segments is 3.2% (core, *RMS* = 4.9%). This is better than the resolution for the single muon confirmation because the average momentum of these muons is lower. For hadronic L0 candidates, the  $E_T$  resolution in the L0 trigger is 35%. This is improved with the track confirmation to  $\sigma_p/p \sim 4.5\%$  (core, *RMS* = 6%). For electron candidates, the  $p_T$  precision hardly improves the energy measurement of the calorimeter, mainly because of bremsstrahlung effects. The information gain here is mainly the distinction between electron and photon candidates.

### Algorithm execution time

The CPU usage of the algorithm has been evaluated on PCs with 2.2GHz-64 bit processors, using standard LHCb compilation options. It can be separated in three parts: seed preparation, hit decoding and track reconstruction. The seed preparation time is negligible in the implementations discussed here. It becomes relevant if the calorimeter has to be decoded, see Section 4.1. The hit preparation is discussed in Section 4.2. Its average lies between 0.7 and 1 ms for the different seeds, i. e., different number of hits in the search windows. The track finding time for single muon confirmation is shown in Fig. 4.12 (b), it is on average 0.35 ms with significant tails in case of high occupancy. All performance numbers are summarized in Tab. 4.8 for the

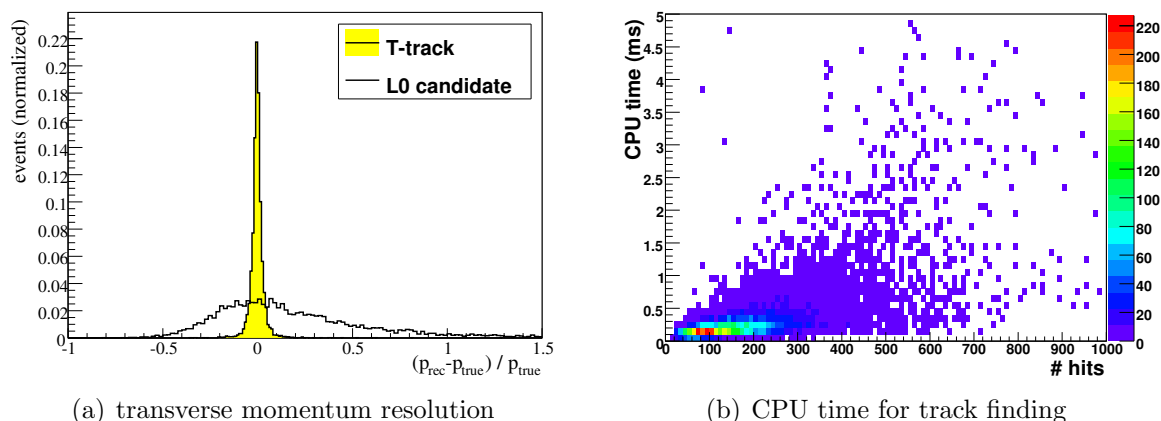


**Figure 4.12:** Performance for *single muon confirmation* in minimum bias events. (a)  $p_T$  resolution of the hardware trigger candidate is shown as black histogram, the resolution of the reconstructed T-track in yellow, both normalized to unit area. (b) Track finding time per seed in ms as a function of the hits in the search window. The average is 0.35 ms.

use cases for the T-Confirmation<sup>2</sup> which are currently implemented in the HLT1.

**Table 4.8:** Summary of the performance for the different use-cases for the T-Confirmation per seed. The optimized search window size is given for each alley in  $n \cdot \sigma$  (x,tx,y,ty). The main differences between the three cases originate in the different resolutions of the track hypotheses.

	L0- $\mu$ (7,4,8,8)	$\mu$ -seg (6,8,8,10)	Hadron (3,3,4,4)	Electron (5,5,5,5)
reconstruction efficiency	96.4 %	95 %	96.6 %	95.8 %
#reconstructed tracks	1.15	5.0	1.2	1.02
$p_T$ resolution (core)	3.4 %	3.2 %	4.5 %	8 %
CPU time decoding	0.7 ms	1 ms	0.8 ms	0.5 ms
CPU time track finding	0.35 ms	1.0 ms	0.75 ms	0.15 ms

## 4.5 Summary

An algorithm to confirm the hardware trigger candidates with tracks in the T-Stations has been presented. This algorithm allows to set up a new, redundant trigger selection in the first level of the software trigger.

L0 trigger candidates for true muons, hadrons and electrons can be confirmed to tracks with an efficiency above 95 %. The transverse momentum resolution is improved from  $\sim 30\%$  to  $3 - 5\%$ . The complete CPU time needed for the L0 confirmation with T-Station tracks is well within the time budget of the online farm (see Section 3.2) for

<sup>2</sup>The track confirmation for L0-electron and L0-photon candidates is currently being implemented.

all four applications. For the HLT1 single muon,  $\mu$ -seg and electromagnetic trigger alley, it is used as default algorithm in the  $LHCb$  trigger system. For the hadronic confirmation, the two algorithms (T-Station confirmation and Velo confirmation) are still competing.

# Chapter 5

## Track based software trigger

This chapter starts with a description of the implementation of a simplified Kalman Filter based track fit in the software trigger. The track fit improves the parameter estimate of the tracks and provides with the track fit  $\chi^2$  a quality criterion on which good tracks can be selected.

Sections 5.2 and 5.3 present the implementation of the *L0 confirmation* algorithm which Chapter 4 describes to select hadrons and muons in HLT1. The muon trigger selection studied in this chapter is focused on the *lifetime unbiased selection* where care has been taken not to introduce any bias in the  $B$  meson lifetime. This chapter concludes with a discussion of the dimuon selection for the second level of the software trigger, where a *lifetime unbiased*  $J/\psi(\mu^+\mu^-)$  selection has been developed.

In this chapter, the complete software trigger chain for muons has been rewritten and optimized such that muons can be triggered without a modification of the  $B_s$  meson lifetime. This is an essential prerequisite for the *lifetime unbiased* analysis of the  $B_s \rightarrow J/\psi\phi$  decay channel, which is discussed in Chapter 6.

### 5.1 The fast kalman filter based track fit

The track fit is used to determine the best estimates of the track parameters along the particle trajectory. In the LHC***b*** experiment, the track fit is used to obtain the momentum from the deflection of the particle in the magnetic field and to locate the primary and secondary vertices. Furthermore, it is used to efficiently match the tracks to RICH rings, calorimeter clusters and muon station measurements. In this section, the Kalman Filter based track fit will be discussed together with the simplifications to make it usable for fast trigger applications.

#### 5.1.1 Full track fit

In the Kalman filter fit procedure [94, 95] the measurements on the track are added one by one into the fit, the knowledge of the track parameters is improved progressively by adding the information of the measurements (see Figure 5.1). As long as material effects are not included, the Kalman filter based track fit is mathematically equivalent to a least squares fit.

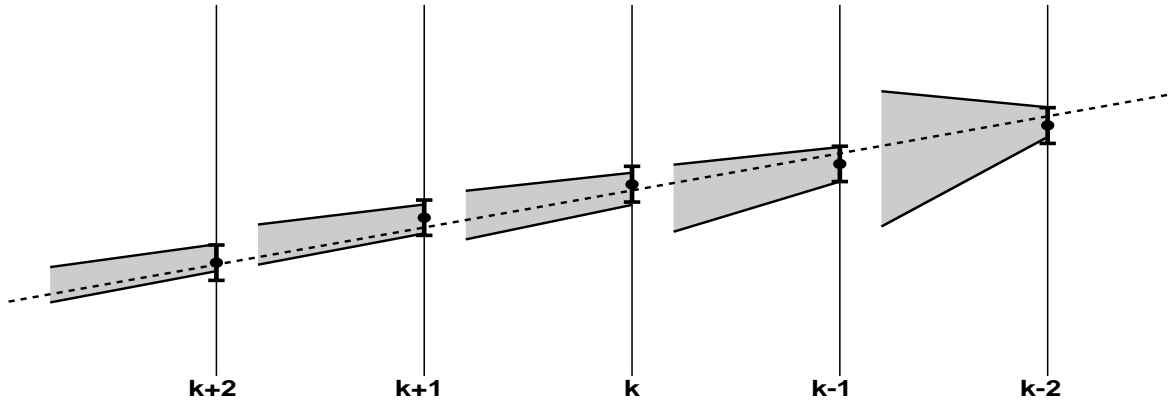


**Figure 5.1:** Kalman filter track fit, applied from right to left: The vertical lines correspond to the detector planes with the measurement points and their errors. The cones represent the uncertainty in the reconstructed track parameters which is stepwise updated with each measurement. (Figure from [96]).

The Kalman Filter track fit implementation in LHC*b* is discussed in detail in the References [21] and [96]. It consists of the following steps:

- **Seeding the fit:** Before the fit starts, the initial state and covariance have to be set. This seed is provided by the pattern recognition. The computation of multiple scattering and energy loss of the particles traversing the detector material is only done with the initial estimate of the track.
- **Prediction:** The prediction of the trajectory (i.e., state and covariance) from one measurement to the next is done using the knowledge of the track so far. Multiple scattering is taken into account by increasing uncertainties depending on the material between the two measurements.
- **Filter:** The prediction is updated with information of the new measurement. The weighted mean of the information of the measurement and the predicted track parameters is calculated. The prediction and filter steps are repeated until all measurements are included. To further improve the estimate of the track parameters, several iterations of the track fit can be done in forward and backward direction. The best information on the track states is obtained by combining the fit result from the forward and backward fit iteration.
- **Iteration:** The above steps can be iterated to improve the precision of the calculated track parameters.

When the fit is iterated, an outlier hit with the highest contribution to the  $\chi^2$  can be removed. The track is then fitted without the contribution of this hit. In the standard LHC*b* implementation of the track fit, three iterations of the bidirectional fit are run (i.e., in total six iterations are done). A maximum of two outlier hits with a  $\chi^2$  contribution of at least 9 are removed.

The CPU time needed for the LHCb track fit is about 10 ms per track<sup>1</sup> as shown in Figure 5.2 (a). This CPU time is largely dominated by the location of intersections with detector material.

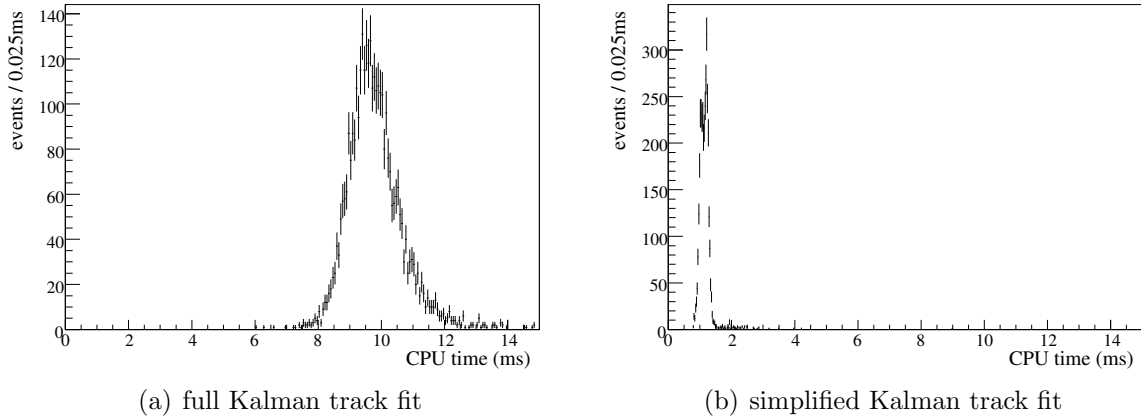


**Figure 5.2:** CPU time needed per track: a) for the full Kalman filter based track fit as it is used offline. The mean time is 10 ms per track. b) for the simplified Kalman filter track fit (see text), the mean time per track is 1 ms.

### 5.1.2 Simplified track fit

To use the Kalman filter based track fit in the trigger, the CPU time has to be minimized. The following simplifications are performed (for details, see [97]):

- In the prediction and projection steps, the material distribution in the detector is extracted from a database. The full track reconstruction uses a very fine granularity of this description, the material lookup therefore takes a significant part of the track fitting time. To speed up, a simplified material service with only a rough geometry resolution is used. This simplification reduces the total time needed for the fit by a factor of three.
- To further reduce the CPU time, only one iteration of the track fit is performed. To get the best estimate of track properties at the interaction point, the fit is done in backwards direction, i. e., from the muon stations to the Velo. Without iterating the track fit, the rejection of outlier hits cannot be done. The degradation of the impact parameter resolution by outlier hits in the Velo is currently under study [98].

These simplifications are a balance between the maximal precision on the track parameters obtained from the full offline fit and the need of the trigger to be as fast as possible. The total CPU time per track for the simplified Kalman filter track fit is shown in Figure 5.2 (b). The average time of 1 ms needed for the simplified track fit is well suited for an application in the HLT first level at a rate of a few tens of kHz. This application is discussed in the following sections.

<sup>1</sup>The time is measured as discussed in Section 3.2.

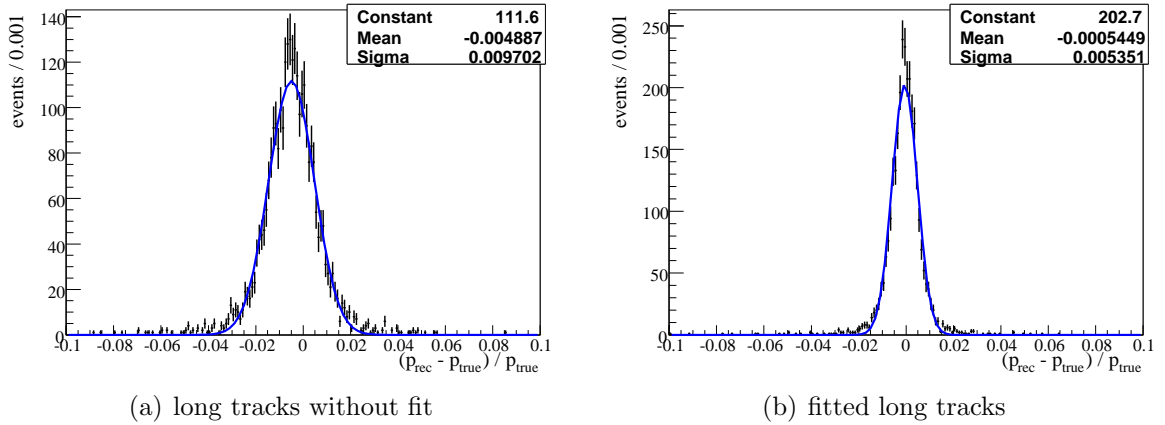


**Figure 5.3:** Relative momentum resolution for (a) unfitted long tracks. The resolution is determined to be 1%. (b) for long tracks fitted with the simplified track fit, the resolution is improved to 0.5%.

Figure 5.3 (a) shows the relative momentum resolution for unfitted long tracks, reconstructed in the *muon alley*. The resolution determined by the width of a single Gaussian fit to the distribution is 1%. Figure 5.3 (b) shows that the relative momentum resolution for these tracks fitted with the fast track fit has improved to 0.5%. This improvement is particularly helpful in HLT2, where the selections are based on the invariant mass, see Section 5.4.

The fast track fit also improves the parameter estimate of the track at the vertex, provides a criterion on the track quality with the fit  $\chi^2$  and can be used to improve the muon identification if a long track with muon hits is fitted. These benefits of the Kalman filter track fit are presented with the discussion of the HLT1 alleys in the following sections.

## 5.2 Hadron selection in the first level of the software trigger

The LHCb hadron alley in HLT1 is based on the identification of charged hadrons with relatively large transverse momentum ( $p_T$ ) and large impact parameter with respect to their closest primary vertex ( $IP$ ), consistent with a secondary vertex separated from the pp-interaction. The entry point of the hadron trigger selection (“hadron alley”) is a positive decision in the Level-0 hadron trigger. This corresponds to an input rate of about 600 kHz. This high rate has to be reduced early in the software trigger chain using as little CPU power as possible. The aim of the HLT1 hadron alley is to reduce this rate at least by a factor of 50.

The hadron alley is divided in two *lines*, named single hadron and dihadron, see Figure 5.4. The single hadron line sets the trigger decision only on tracks from the L0 confirmation while the dihadron combines it with a companion track to form a secondary vertex. The dihadron decision is based on this vertex.

As discussed in Section 3.3.1, there are two ways to confirm a Level-0 candidate in

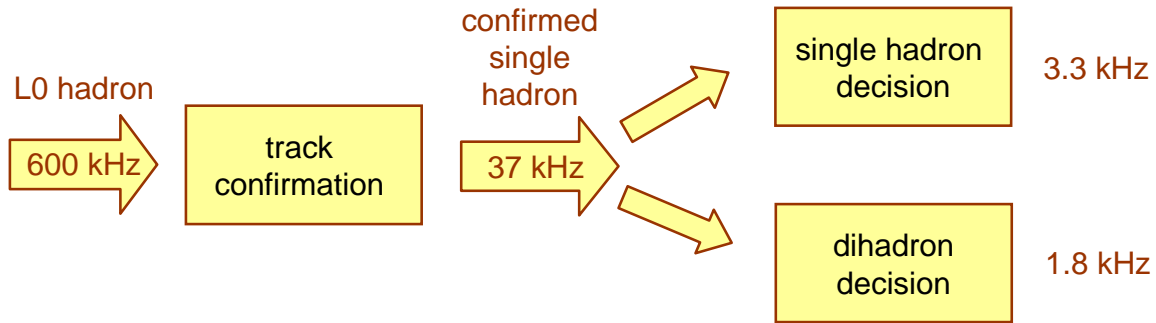


**Figure 5.4:** Scheme of the *hadron alley* which is presented in this section.

the single hadron line: With tracks from the Vertex Locator (Velo) or with tracks from the main tracker. The current default, the confirmation with the Velo, is discussed in Section 3.3.1. This thesis presents an alternative approach, using the confirmation with tracks from the main tracker. At the current time, both strategies are competing and dependent on the performance as measured on data, it will be decided which strategy will be used in the LHCb trigger. The dihadron selection is the same for both strategies.

The tracks which pass the single and dihadron selection are fitted with the simplified Kalman filter based track fit (see Section 5.1.2). The selection cuts are repeated utilizing the improved parameter estimates and tracks with a bad reconstruction quality are rejected.

In the following, these steps are discussed in further detail. Throughout this section, the decay  $B_d \rightarrow \pi^+\pi^-$  will be used as an example channel to illustrate the signal properties (for simplicity called **signal**) and will be compared with **minimum bias** events, see Section 2.4. At the end of this chapter, the efficiencies for single hadron and dihadron HLT1 trigger selection are presented for other  $B$  signal channels.

### 5.2.1 Single hadron selection using the tracker

The general strategy for the single hadron confirmation is as follows: The track assumption for the L0 hadron trigger candidate is first confirmed or discarded using a T-Station track with the requirement of a minimum transverse momentum. This T-track (the definition of the track types is given in Section 2.1.5) is then extended to a long track via a match to a Velo track. A minimum impact parameter is required for this long track. A candidate at this stage is called *confirmed single hadron*, see also Figure 5.4. It is required to have high  $p_T$  so that the rate is sufficiently low for the single hadron decision.

#### Track confirmation

The single hadron alley starts with L0 hadron candidates at a *minimum bias* rate of 600 kHz, see Section 3.1.2. The candidates are confirmed to T-tracks as discussed in Chapter 4. Because of the very high input rate, fast algorithm execution time is the main focus of the tuning of the search window sizes. Figure 5.5 shows a tuning of

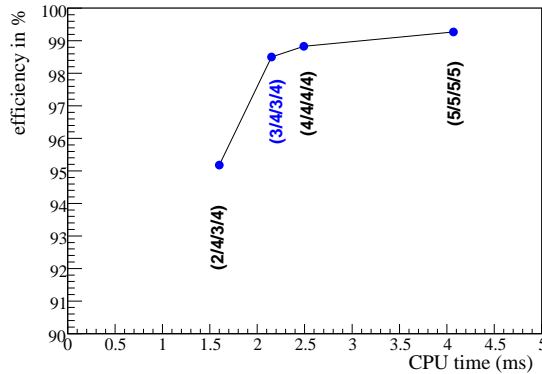


**Figure 5.5:** *Hadron alley:* Tuning of the *T-Confirmation* search windows for the track finding, efficiency versus CPU time per track for various configurations in  $n \cdot \sigma$  in  $(x, t_x, y, t_y)$ . The configurations are indicated in the figure, for an explanation of the notation see text. The chosen configuration (3,4,3,4) is highlighted in blue.

the trigger efficiency of the track confirmation step for various configurations of the search window size. A search window configuration of (3,4,3,4) in  $(n_x, n_{tx}, n_y, n_{ty})$  is found to give an optimal compromise between high signal efficiency and the required fast algorithms execution time. Using this search window configuration, the efficiency to reconstruct a track in the search window is 98.5 % for signal events, the complete reconstruction time is 2.15 ms.

In minimum bias events, no track is reconstructed in the search window for 15 % of the events, those events are discarded. The candidates transverse momentum ( $p_T$ ) resolution of the tracks reconstructed in the T-Station is 4.5 %, as shown in Section 2.1.6. The transverse momentum spectrum of the highest  $p_T$  track per event is shown in Figure 5.6 (a) for signal and minimum bias events. The signal events are clearly shifted to higher  $p_T$  values, a selection based on  $p_T$  gives a good separation power. The signal efficiency versus minimum bias rate for various cuts on  $p_T$  is shown in Figure 5.6 (b). A requirement of  $p_T > 2.5$  GeV keeps 93 % of the signal events and reduces the minimum bias rate to 320 kHz. On average, 1.7 candidates per event are left after the track confirmation and  $p_T$  selection.

### Extension to long tracks

To continue the refinement of the track, the T-track is matched with a track segment reconstructed in the Vertex Locator (Velo) to form a long track.

The Velo sensors measure the  $r$  and  $\phi$ - coordinates of the tracks, see Section 2.1.1. The track reconstruction is done in two steps: First, only the  $r$ -sensor information is used and 2D tracks are reconstructed. These 2D Velo tracks are then matched to the T-Station tracks. Both tracks are extrapolated to the center of the magnet and their distance is calculated, for details see Reference [79]. The distribution of this distance is shown in Figure 5.7 (a) for correct (black) and wrong (red) matches. A cut of 80 mm on this distance reduces the total average number of 66 Velo 2D tracks in minimum bias events to an average of 10 accepted candidate tracks, without losing events on signal.

The Velo 2D tracks which are successfully matched to a T-track are then reconstruct-

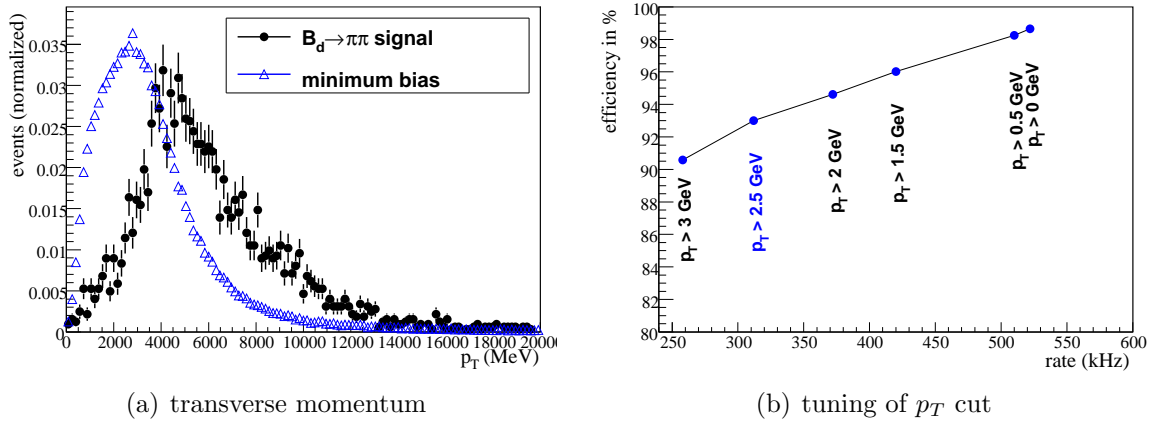


**Figure 5.6:** *Hadron alley*: (a) Spectrum of the highest  $p_T$  track per event for  $B_d \rightarrow \pi^+ \pi^-$  signal (mean: 6 GeV) and minimum bias events (mean: 3.7 GeV), both normalized to unit area. (b) Tuning of the  $p_T$  requirement: Efficiency versus retention for different requirements in  $p_T$ . The chosen requirement ( $p_T > 2.5$  GeV) is indicated in blue.

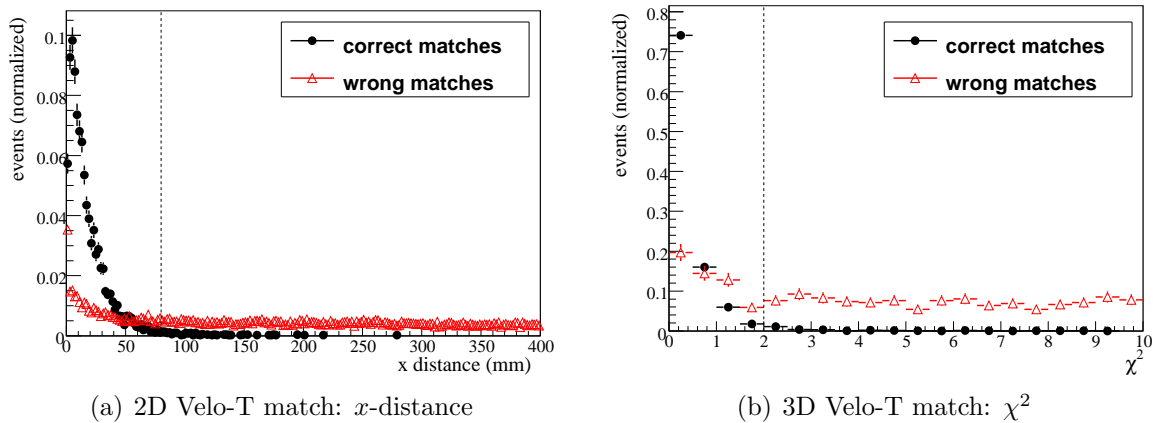


**Figure 5.7:** Velo-T match in the *hadron alley*: (a)  $x$ -distance at the center of the magnet for the 2D Velo-T match. The requirement of 80 mm is indicated by a dashed line. (b)  $\chi^2$  distribution for the 3D Velo-T match. The requirement of 2 is indicated by a dashed line. The Histograms are normalized to unit area.

ed to a Velo 3D track. This two step procedure reduces the costly Velo 3D reconstruction to a minimum, only 10 % of the Velo 3D tracks are reconstructed. This Velo 3D track is now again matched to the T-track. A  $\chi^2$  quantity is then calculated [99]:

$$\chi^2 = \frac{\text{dist}(x)}{\sigma_x^2} + \frac{\text{dist}(y)}{\sigma_y^2}, \quad (5.1)$$

where the distance in  $x$  is evaluated at the center of the magnet and the distance in  $y$  at the end of T3, taking the worse resolution of the T-Stations in  $y$  direction into account. The errors  $\sigma_x$  and  $\sigma_y$  are parameterized as

$$\sigma_x^2 = 8^2 + (t_{x,T} - t_{x,V})^2 \times 80^2 \text{ mm}^2, \quad (5.2)$$

$$\sigma_y^2 = 8^2 + \theta^2 \times 240^2 \text{ mm}^2, \quad (5.3)$$

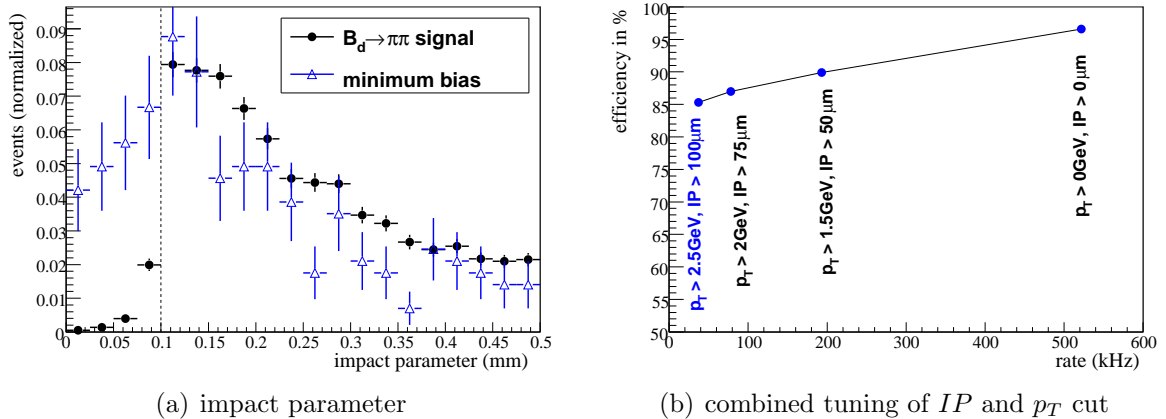


**Figure 5.8:** *Hadron alley*: (a) Impact parameter with respect to the closest primary vertex for  $B_d \rightarrow \pi^+\pi^-$  signal and minimum bias events, normalized to unit area. (b) Tuning of the  $IP$  selection criteria for candidates which passed the  $p_T$  selection. The chosen combination of  $p_T$  and  $IP$  requirement ( $p_T > 2.5 \text{ GeV}$ ,  $IP > 0.1 \text{ mm}$ ) is indicated in blue.

where  $t_{x,T}$  and  $t_{x,V}$  are the  $x$  direction of the track in the T-Stations and the Velo respectively and  $\theta$  is the angle between the track and the beam axis. The factors are determined empirically [99]. In Figure 5.7 (b), the  $\chi^2$  distribution of the 3D matching is shown in black for correct matches and in red for wrong matches. A cut at  $\chi^2 < 2$  is highly efficient on correctly matched tracks and reduces the majority of wrong matches. The Velo 3D and T-track together form a long track. The momentum resolution of these long tracks before the track fit is 1%.

### Confirmed single hadron

In the next step, the primary vertex (PV) is reconstructed from the 2D Velo tracks. The impact parameter ( $IP$ ) of the long tracks is then calculated with respect to the closest PV. Figure 5.8 (a) shows the impact parameter for tracks from signal and minimum bias events, a clear separation at low  $IP$  values is seen. To find the optimal combination of  $IP$  and  $p_T$  requirements on the tracks, the  $p_T$  requirement applied earlier is opened. Figure 5.8 (b) shows the signal efficiency versus the minimum bias rate for a subsequent tightening of both  $IP$  and  $p_T$  requirements. A minimum impact parameter of  $100 \mu\text{m}$  together with a requirement of  $p_T > 2.5 \text{ GeV}$  gives a minimum bias rate of 37 kHz and a signal efficiency of 85.5%.

The requirement to have a high  $IP$  and  $p_T$  on the same track gives a large reduction in the rate (a factor of ten), while both the  $p_T$  and the  $IP$  requirement alone reduce the rate only by a factor of two.

### Single hadron decision

To further reduce the minimum bias rate, the minimum  $p_T$  is required to be 5 GeV. This reduces the rate to 7.5 kHz and the efficiency in  $B_d \rightarrow \pi^+\pi^-$  decays to 55%. This efficiency is relatively low, however, the single hadron decision guarantees the robustness

of the hadron trigger as it is only based on one track.

### Dihadron selection

After a single hadron has been confirmed, the dihadron trigger selection starts with the reconstruction of all Velo 3D tracks at a rate of Vertices are created combining the candidate with a second track. The requirement of a good vertex is that two tracks have a distance of closest approach (DOCA) smaller than 0.2 mm. This distance is large enough to include tracks from other short lived decays, e. g., hadrons from  $B_s \rightarrow D_s^\mp K^\pm$ . Additionally, the vertex is required to be downstream compared to its closest PV.

In the next step, the forward reconstruction of the Velo tracks is performed. Only vertices where the companion track has a  $p_T$  greater than 1 GeV are selected. Furthermore, the combined momentum vector of the two tracks in the secondary vertex is required to point to the primary vertex. This reduces the rate to 5.8 kHz with on average 1.9 candidates per event. The signal efficiency for  $B_d \rightarrow \pi^+ \pi^-$  events is 79.9%.

### 5.2.2 Fast track fit in the hadron alley

The candidates accepted by the single hadron and dihadron selection are fitted using the fast Kalman filter based track fit. As the fit is applied to 1.9 tracks at a rate of 11.3 kHz, the contribution of the track fit to the total CPU time for the hadron alley is negligible, it adds less than 2.5% to the total hadron alley CPU time.

On the fitted tracks, the selection cuts are repeated profiting from the improved parameter estimate. The improved  $IP$  estimate reduces the rate by approximately 15% while it is almost 100% efficient on signal tracks.

Next, a requirement on the track  $\chi^2$  is applied to reduce ghost tracks. Figure 5.9 shows the  $\chi^2$  contribution of real tracks and ghost tracks. A separation between the two distributions is clearly seen, real tracks have a dominant peak to low  $\chi^2$  whereas ghost tracks have a much wider  $\chi^2$  distribution. A requirement of  $\chi^2 < 10$  is chosen to be almost 100% efficient on real tracks whereas it efficiently removes ghost tracks. As a result, this requirement reduces the minimum bias rate by 40%. In total, the fast track fit reduces the trigger rate of the hadron alley by a factor of two while the signal events which have passed all HLT cuts so far are accepted in 98% of the events.

### 5.2.3 Summary of the hadron alley

An implementation for the L0 confirmation with the T-Stations in the HLT1 hadron alley has been presented. The efficiency to select signal events is summarized in Table 5.1. The efficiency is normalized to events which are selected by the respective analysis and the L0 hadron trigger. The minimum bias rate is reduced by almost a factor of 130. The efficiency for two-prong decays is good ( $\sim 80\%$ ), it is not as good for four-prong decays, e. g.,  $\sim 50\%$  for  $B_s \rightarrow \phi\phi$ . The problem in multi body decays is that the requirement for the L0 trigger (a cluster with  $E_T > 3.5$  GeV) is very hard, in these events the hardware trigger is often issued by a particle independent of the signal. If one restrict the events to those where the signal decay products triggered the L0, the confirmation efficiency increases, e. g., for  $B_s \rightarrow \phi\phi$  from 53% to 89% [100].

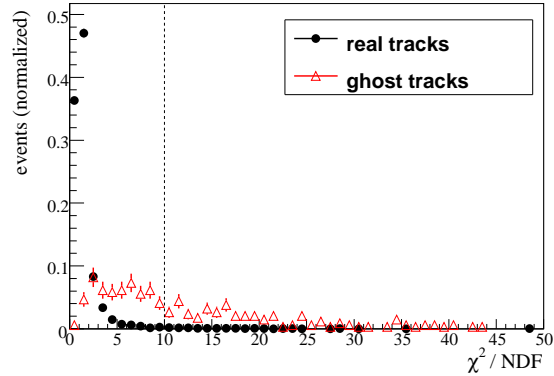


**Figure 5.9:** Track fit in the *hadron alley*:  $\chi^2$  for tracks which are associated to a generated particle (real tracks) and those which are not (ghost tracks), normalized to unit area.

This reveals a general problem of the HLT1 confirmation strategy: a L0 trigger can only be confirmed if the L0 decision was based on a signal decay product. If the L0 was triggered by a particle independent from the signal, it should by concept not be confirmed. Whereas this strategy works very well for two and three prong decays, it shows some inefficiencies in  $B$  decays with more particles in the final state. An approach to lower this threshold to start the confirmation after a L0 trigger decision is currently being investigated [100].

**Table 5.1:** HLT1 rate determined on minimum bias events and efficiency determined on events accepted by L0 and offline analysis of the respective channel.

channel	single hadron	dihadron	total
minimum bias	3.3 kHz	1.8 kHz	4.6 kHz
$B_{(s)}^0 \rightarrow h^+ h^-$	56 %	76.2 %	78 %
$B_s \rightarrow D_s^- \pi^+$	37.5 %	66.5 %	68.3 %
$B_s \rightarrow \phi\phi$	19 %	51.5 %	53 %

### 5.3 Muon selection in the first level of the software trigger

In the first level of the software trigger (HLT1), events with muons in the final state are selected by a single muon and a dimuon trigger selection, called *muon alley*.

The L0 muon candidate is first confirmed with a track. The HLT1 trigger decision is then done based on the muon track (L0- $\mu$ ) or on the dimuon vertex (L0-di $\mu$ ). To reduce the minimum bias rate, the selection on a single muon track needs harder requirements than on a dimuon vertex.

Many of the core physics analyses of LHCb contain two muons in the final state, e. g.,  $B_s \rightarrow J/\psi\phi$ ,  $B_s \rightarrow \mu^+\mu^-$  or  $B_d \rightarrow K^{*0}\mu^+\mu^-$ . For these events, the L0 single muon trigger

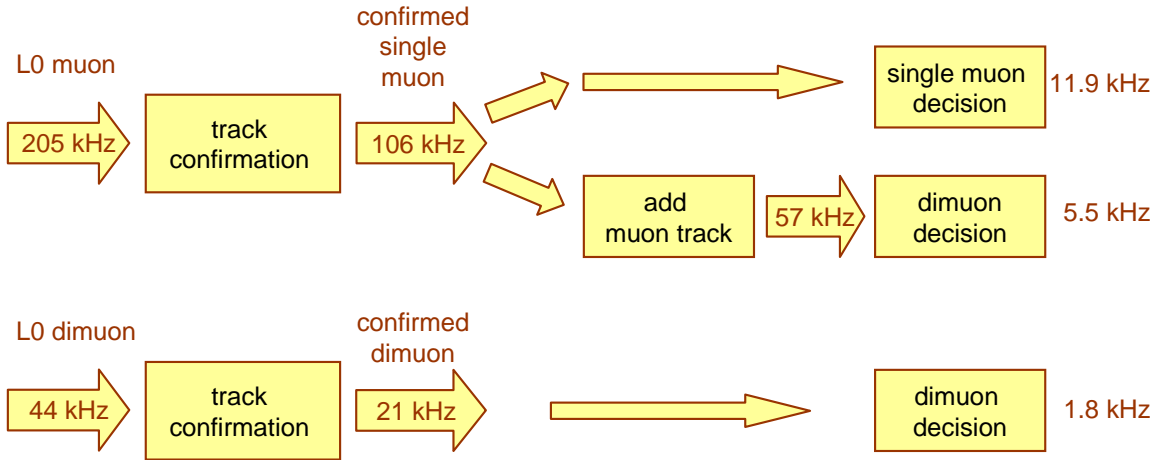


**Figure 5.10:** Scheme of the *muon alley* which is presented in this section.

is much more efficient than the dimuon trigger, e. g., in  $B_s \rightarrow J/\psi\phi$ : the  $L0\text{-}\mu$  efficiency is 91.8 % whereas the  $L0\text{-}di\mu$  efficiency is only 65.6 %, see Table 3.1. In HLT1, these events are most efficiently triggered by a dimuon selection, therefore an additional selection starts from a single muon trigger and recovers the second muon with a standalone muon track. This increases the efficiency for dimuon events.

The HLT1 muon alley is summarized in Figure 5.10. In total, the muon alley consists of three different confirmation alleys: A single muon selection which starts from a  $L0\text{-}\mu$  trigger, and two dimuon selections. The first dimuon selection starts from a  $L0\text{-}\mu$  candidate which passed the track confirmation and adds a standalone muon track while the second dimuon selection starts from a  $L0\text{-}di\mu$  trigger.

Each of these confirmation alleys implements two selections at the end:

- A **lifetime unbiased selection** which carefully avoids any requirement on selection variables which is correlated with the  $B$  meson lifetime. To control the minimum bias rate, the requirements on the transverse momentum and dimuon invariant mass are tightened. In the following this selection is called *unbiased* selection.
- A **lifetime biased selection** which selects the candidates based on the muons impact parameter with respect to the primary vertex ( $IP$ ) and on the separation between primary and secondary vertex. In the following this selection is called *biased* selection.

This gives a total of six types of selected events. While the reconstruction code of the different selections is almost the same, the criteria applied in the candidate selection and in the final decision are specific and will be tuned in order to reduce the bandwidth and to keep the efficiency as high as possible for the different muon channels.

Only the single muon and the recovered dimuon alley from standalone muon tracks will be discussed in this chapter, a description of the alley from  $L0\text{-}di\mu$  can be found in

Reference [79]. The optimization of the reconstruction and selection criteria is studied with a special focus on the decay  $B_s \rightarrow J/\psi\phi$ , in the rest of this section referred to as **signal**. The performance figures for other  $B$  decay channels are given at the end of this section. A description of the standard LHCb Muon Alley can be found in Reference [79]. As the reconstruction steps are analogue to those in the hadron alley, a focus will be put on the performance figures for the muon confirmation line.

### 5.3.1 Single muon selection

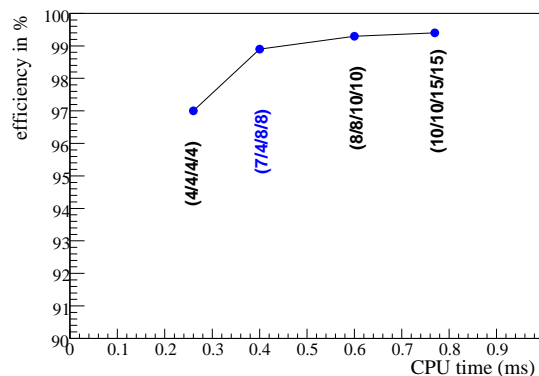
A track in the T-Stations is searched to confirm the L0 trigger candidate. The confirmed track is then extrapolated to the Velo and extended to a long track. All efficiencies quoted in this section are relative efficiencies with respect to generated signal  $B_s \rightarrow J/\psi\phi$  events, see Section 2.4, which are selected by the L0 muon trigger and the offline analysis.

#### Track confirmation in the T-Stations

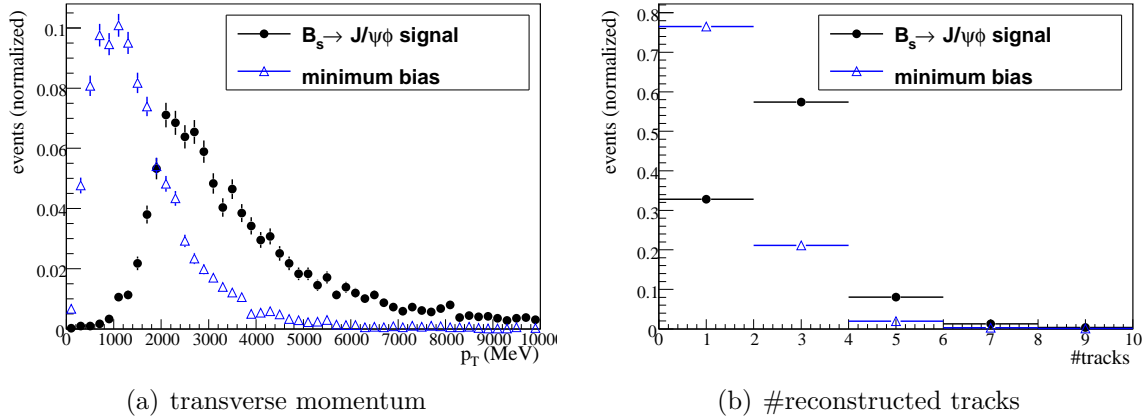
The size of the search window is parameterized according to the granularity of the muon chambers region (see Section 4.1) but has to be tuned for an optimal implementation in the trigger alley. In contrast to the hadron alley, Section 5.2, the input rate of the muon alley is lower by a factor of three. Therefore, the focus of the track confirmation can be put on a maximal signal efficiency.

Figure 5.11 shows the reconstruction efficiency for different configurations of the search window size as a function of the track finding time. A search window configuration  $n \cdot \sigma$  in  $(x, t_x, y, t_y)$  of (7,4,8,8) is found to give an optimal compromise between high efficiency and low algorithm execution time. For this configuration, the confirmation step of the single muon line selects signal events with an efficiency of 98.8%, the minimum bias rate is 142 kHz. The CPU time for track finding is 0.4 ms. In minimum bias events, in about 30% of the cases, no track is reconstructed. These events are rejected even before the  $p_T$  cut.

The spectrum of the highest  $p_T$  track per event is shown in Figure 5.12 a) for



**Figure 5.11:** *Single muon alley:* Tuning of the *T-Confirmation* search windows for the track finding, efficiency versus CPU time per track for various configurations in  $n \cdot \sigma$  in  $(x, t_x, y, t_y)$ . The chosen configuration is (7,4,8,8).



**Figure 5.12:** *Single muon alley:* (a) Transverse momentum distribution for minimum bias (mean: 1.6 GeV) and  $B_s \rightarrow J/\psi\phi$  signal (mean: 3.7 GeV). (b) Number of reconstructed tracks with sufficient  $p_T$  per event for minimum bias (mean: 1.3) and signal (mean: 2.1). Both histograms are normalized to unit area.

minimum bias and signal events. The  $p_T$  spectrum of signal events is clearly shifted to higher  $p_T$  values. A minimum  $p_T$  of 500 MeV yields to a relative signal efficiency of 98.7% with 2.1 candidates per event on average, as shown in Figure 5.12 (b). On minimum bias events, 1.3 tracks reconstructed per event at a rate of 130 kHz.

### Extension to long tracks

These T-tracks are then matched to Velo tracks, analogue to the hadron confirmation. A requirement of 200 mm  $x$ -distance at the center of the magnet for 2D Velo tracks and a matching  $\chi^2$  better than 6 for the 3D Velo to T-Station match gives 1.5 candidates at a rate of 106 kHz. The efficiency in signal events is 98.3%. The Velo 3D and T-track together form a long track.

### Confirmed single muon

After the extension to long tracks, the minimum bias rate at 106 kHz is too high to be passed to the second trigger level, so either some harder trigger selections are introduced for the single muon trigger decision or the candidates are passed to the recovered dimuon search.

### Single muon decision

The confirmed single muon events are passed to two selections:

- **Unbiased selection:** The candidates are only selected by their  $p_T$  (requirement:  $p_T > 6$  GeV) which gives no trigger bias on the  $B$ -lifetime.
- **Biased selection:** The candidates are selected by their  $IP$  and  $p_T$  (requirements:  $IP > 80 \mu\text{m}$ ,  $p_T > 1.3$  GeV). This selection is referred to as *biased* selection because it modifies the lifetime distribution of the  $B$  meson.

The *unbiased* selection requires a large transverse momentum to reduce the rate to 1.3 kHz. The  $B_s \rightarrow J/\psi\phi$  signal efficiency for these events is 14.9%. The *lifetime biased* selection accepts minimum bias events with a rate of 13 kHz and has a signal efficiency of 78.8%. The rate of 13 kHz is almost 50% of the total HLT1 output rate. This is because a single, high  $p_T$  muon is a generic signature of a leptonic  $B$  decay. The high rate of  $b \rightarrow \mu + X$  events gives a large sample of events where one of the two  $B$  mesons is completely unaffected by the trigger. The signal efficiency and minimum bias rate of the single muon alley are summarized in Section 5.3.4 together with the other lines of the HLT1 muon trigger.

### 5.3.2 Dimuon recovery selection

The dimuon recovery selection starts from a confirmed single muon trigger candidate and adds an additional muon candidate, called muon segment ( $\mu$ -seg). The muon segment is confirmed to a long track with the same algorithm flow as the L0 triggered muon candidates. Pairs of tracks of one confirmed L0 muon and one confirmed muon segment are then used to form a dimuon vertex on which the trigger decision is based.

In this section, the performance of the reconstruction and selection of the recovered dimuon pairs is discussed. The efficiencies within this section are relative efficiencies normalized to selected  $B_s \rightarrow J/\psi\phi$  events which have a confirmed L0 muon candidate and at least one reconstructed muon segment, see Section 2.3.1. At the end of this chapter, the efficiency normalized to L0 triggered events will be given as well.

#### Muon segment reconstruction

The reconstruction of muon segments is described in Section 2.3.1. To exclude muon segments which have already been found as L0 candidates, it is checked if the segment shares hits with the L0 candidate. Only muon segments which do not share hits in the muon stations  $M_2$  and  $M_3$  with a confirmed L0 candidate are taken for the confirmation.

The requirement that one confirmed L0 candidate is accompanied by one (different) standalone muon track reduces the minimum bias rate from 107 kHz to 57 kHz. On selected, L0 triggered  $B_s \rightarrow J/\psi\phi$  events, 77% of the events pass this requirement. In the next step, the muon segments have to be confirmed by a track in the T-Stations.

#### Track confirmation

The standalone muon track is required to pass the same confirmation algorithm as a L0 triggered muon. However, as the average momentum is lower ( $\sim 28$  GeV, see Figure 4.1) and the search windows are less precise (see Section 4.1.1), the region of interest for the track search is generally larger than for the single muon confirmation. However, the lower input rate of 57 kHz makes the CPU time consumption less constraining.

A tuning of the search window size similar to the one discussed in the last section is performed, see Figure 5.13. A configuration in  $n \cdot \sigma$  in  $(x, t_x, y, t_y)$  of (6, 8, 8, 10) has found to be optimal. The search windows are relatively large as the distribution of the seed estimate has significant non-gaussian tails. For this configuration, signal tracks are confirmed with 98.3% efficiency in a CPU time of 6 ms.

At this stage, the events are not filtered on their transverse momentum. E.g., in the decay channel  $B_d \rightarrow K^{*0} \mu^+ \mu^-$ , this would introduce modifications in the angular structure of the decay products, see Section 6.3.1.

### Extension to long tracks

Completely analogously to the single muon confirmation, the T-tracks from muon segments are then matched with first a Velo 2D and then with Velo 3D tracks. The rate after the matching to Velo 3D tracks is 51 kHz while being 96 % efficient for  $B_s \rightarrow J/\psi \phi$  events. The transverse momentum spectrum of the muon candidates is shown in Figure 5.14 (a). The separation between signal and minimum bias events is not as clear as in the spectrum of confirmed L0- $\mu$ .

### Muon pair combination

One confirmed, L0 selected muon and one confirmed muon segment are then combined to form a dimuon system. The distance of closest approach (DOCA) between the two *long tracks* is required to be smaller than 0.5 mm. The invariant mass spectrum for muons from  $B_s \rightarrow J/\psi \phi$  and for minimum bias events is shown in Figure 5.14 (b). For signal events, the dimuon invariant mass shows a clear peak at the  $J/\psi$  mass, the resolution (from a Gaussian fit) is 34 MeV. The events shown in Figure 5.14 (b) correspond to 41 kHz and contain 94.3 % of the signal events from the beginning of the recovered dimuon selection. In minimum bias events, the true  $J/\psi$  decays are seen as a small peak in the combinatorial background.

### Dimuon decision

To reduce the minimum bias rate, the events have to pass further selection requirements:

- **Unbiased selection:** The dimuon pair is selected by its invariant mass (requirement:  $m_{\mu\mu} > 2.5$  GeV) and transverse momentum ( $p_T > 0.5$  GeV), which gives no trigger bias in the  $B$ -lifetime.

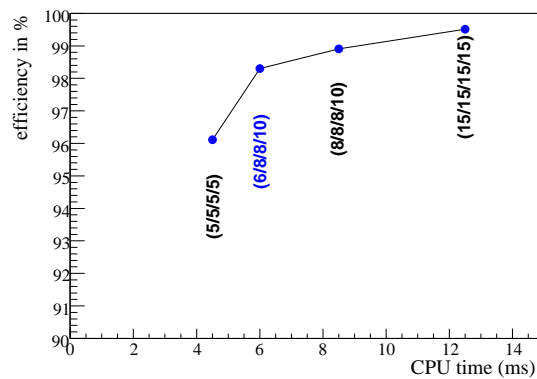


**Figure 5.13:** *Dimuon recovery selection:* Tuning of the *T-Confirmation* search windows, efficiency versus CPU time per track for various configurations in  $n \cdot \sigma$  in  $(x, t_x, y, t_y)$ . The chosen configuration (6, 8, 8, 10) is indicated in blue.

- **Biased selection:** The dimuon pair is selected by its invariant mass and the minimum  $IP$  of the tracks (requirements:  $m_{\mu\mu} > 0.5 \text{ GeV}$  and minimum  $IP > 150 \mu\text{m}$ ). No requirement on the muon  $p_T$  is done at any stage of the software trigger selection.

In both selections, the combinatorial background towards small invariant masses is rejected. These selections give a rate of 13.2 kHz. The efficiency of the *lifetime unbiased* selection is 89.8% with respect to the input of the alley. Measured on all L0 triggered events, the efficiency of this selection is 69%. This efficiency is relatively low because this selection focuses on low transverse momentum muons (one candidate above the L0 threshold, the other below). The dimuon from L0-di $\mu$  selection, which is discussed in detail in Reference [79], is the complementary, high  $p_T$  selection. The total signal efficiency, obtained by the combination of low- and high momentum dimuon selections, is summarized in Section 5.3.4.

The efficiency of the *lifetime biased* selection is 53.3% with respect to the input of the alley. The impact parameter requirement reduces the efficiency dramatically because no lifetime biasing requirement is applied in the analysis. The efficiencies of the *biased* dimuon selection in other  $B$  signal channels is summarized in Section 5.3.4.

### 5.3.3 Fast track fit in the muon alley

The candidates accepted by the single muon and the three dimuon selections are fitted using the simplified Kalman filter based track fit, as discussed in Section 5.1. The fit is applied on average to 2.5 candidates at a rate of 25 kHz. The additional time needed by the fit is less than 10% of the total CPU time for the HLT1 muon selection.

For the *muon alley*, the main benefits from the track fit is the muon identification and the ghost rejection: the candidates are fitted including the muon hits and the  $\chi^2$  of the *long track* (without the muon hits) is studied separately to the  $\chi^2$ -contribution of

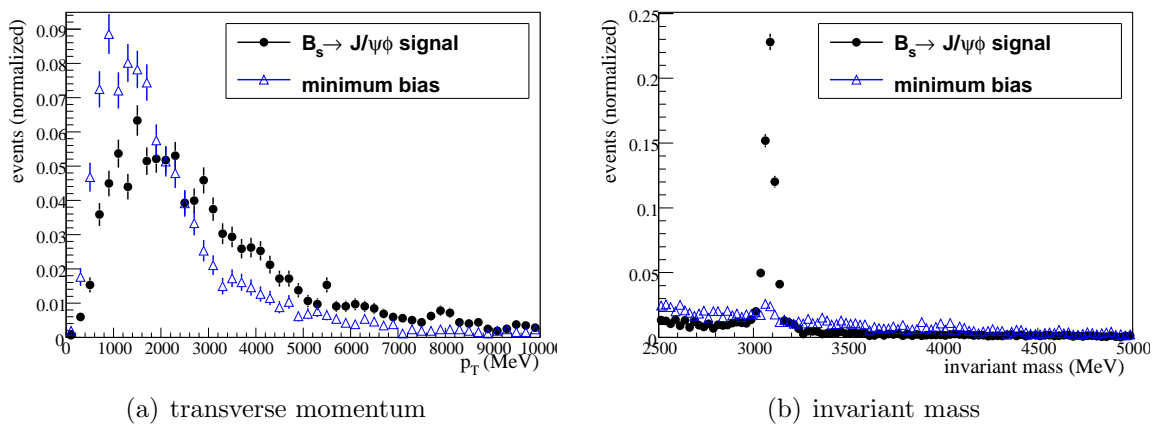


**Figure 5.14:** *Dimuon recovery selection:* (a) Transverse momentum spectrum of the highest  $p_T$  track of the *confirmed muon segments* for  $B_s \rightarrow J/\psi\phi$  signal (mean: 3.1 GeV) and minimum bias (mean: 2.2 GeV). (b) Dimuon invariant mass. Both normalized to unit area.

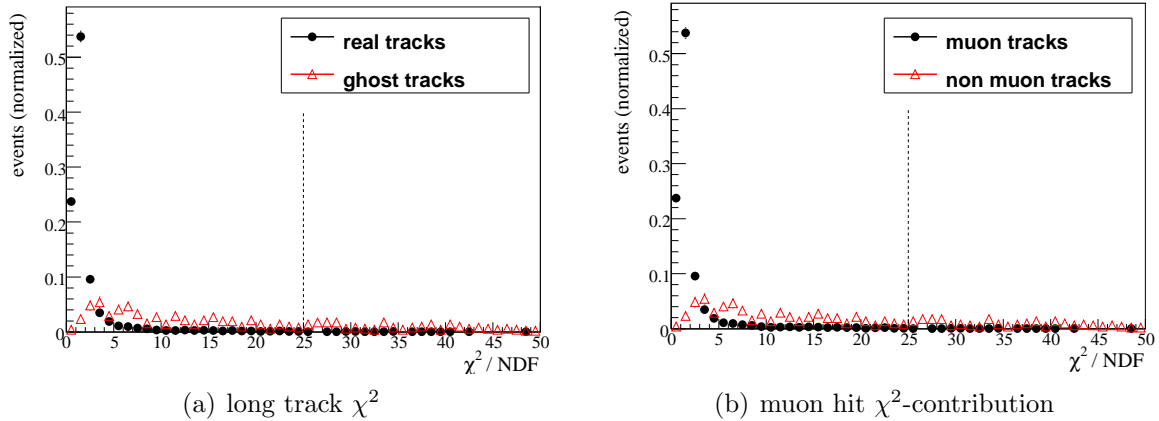


**Figure 5.15:** Track fit in the *muon alley*: (a) Long track contribution to the track fit  $\chi^2$  for tracks which could be associated to a generated particle (real tracks) and tracks which could not be associated (ghost tracks). (b) Muon hit contribution to the track fit  $\chi^2$  for tracks which are generated as muons (black) and other tracks (red).

the muon hits. The latter gives a measure how consistent the muon hits are with the remaining part of the track.

The *long track* fit  $\chi^2$  is shown in Figure 5.15 (a) for single muon tracks. Tracks which are matched<sup>2</sup> to a MC particle are shown in black (real tracks) and those which could not be matched in red (ghost tracks). Dashed lines indicate the proposed cuts which are almost fully efficient on real tracks but suppress a significant amount of ghost tracks.

Figure 5.15 (b) shows the muon hit  $\chi^2$  contribution for tracks which are generator level muons in black and for non-muon tracks in red. A dashed line indicate the proposed cut which again is chosen to be almost fully efficient on real muons but suppress a significant amount of non-muon tracks. The requirements on track quality and muon identification are 98 % efficient in the single muon trigger selection (93 % on the muon segment selection) and suppress 30 % of the minimum bias rate.

### 5.3.4 Summary of the muon alley

The trigger efficiency is summarized for the following LHCb physics channels with muons in the final state:  $b \rightarrow J/\psi X$ ,  $B_s \rightarrow \mu^+ \mu^-$  and  $B_d \rightarrow K^{*0} \mu^+ \mu^-$ .

The channel  $B_s \rightarrow J/\psi \phi$  and the control channels  $B_d \rightarrow J/\psi K^{*0}$  and  $B^+ \rightarrow J/\psi K^+$  are summarized to  $b \rightarrow J/\psi X$  because the kinematic distribution of the  $J/\psi$  decay products is almost identical for all three channels. The rate of events accepted from minimum bias events and the signal efficiencies for all sub-alleys is summarized in Table 5.2. The efficiencies are normalized to any L0 muon triggered events which are selected by the offline selection and the L0 single- or dimuon selection.

Simulated  $B_s \rightarrow J/\psi \phi$  signal events can be selected without exploiting the  $B$  meson lifetime with an efficiency of 86.4 %. This excellent trigger efficiency with a minimal

<sup>2</sup>A MC truth association is considered good if more than 70 % of the hits on the track originate from the same generated particle.

distortion of the acceptances of physics observables enables a lifetime unbiased analysis of the  $B_s \rightarrow J/\psi\phi$  decay to extract the  $CP$  violating phase  $\Phi_s$ , see Section 6.1 for a discussion.

**Table 5.2:** HLT1 muon alley efficiency for events accepted by the L0 muon trigger (single- and dimuon selection) and by their respective offline selection.

	selection	L0- $\mu$	L0-di $\mu$	L0- $\mu+\mu$ -seg	all
minimum bias	biased	11.3 kHz	0.5 kHz	1.0 kHz	17.2 kHz
	unbiased	0.9 kHz	1.5 kHz	4.7 kHz	
$B_s \rightarrow J/\psi\phi$	biased	76.0 %	22.2 %	35.9 %	93.3 %
	unbiased	14.1 %	56.8 %	62.7 %	86.4 %
$B_s \rightarrow \mu^+\mu^-$	biased	97.6 %	64.1 %	56.6 %	98.3 %
	unbiased	33.2 %	69.6 %	63.6 %	92.1 %
$B_d \rightarrow K^{*0}\mu^+\mu^-$	biased	86.3 %	41.2 %	49.5 %	92.1 %
	unbiased	13.7 %	20.7 %	38.4 %	51.2 %

The relatively high rate of 17.2 kHz of minimum bias events that gets accepted by the muon alley is further studied. The generator level information of the particles which triggered the muon alley is used to categorize the events as follows:

- 40 % have the same MC particle associated to the Velo and the T-track. Of these, 70 % are real muons either coming from hadrons containing  $b$  or  $c$ -quarks (dominant) or from  $\pi^\pm$  and K decays.
- 60 % are ghost tracks, either they have a different MC particle associated in the Velo and the T-Stations or they are a ghost already in the Velo- or T-track.

The very high fraction of ghost tracks passing the trigger selection is observed in all HLT selections. It is currently under investigation and there is hope to reduce it significantly [98].

## 5.4 Inclusive dimuon selection for the second software trigger level

In this section, a dimuon selection for HLT2 is presented. A trigger selection which does not introduce a trigger bias on the  $B$  meson lifetime was developed for the analysis of the  $CP$  violating phase  $\Phi_s$  in the channel  $B_s \rightarrow J/\psi\phi$ .

For this final HLT trigger selection, the events from HLT1 are “fully reconstructed” which means the track reconstruction and muon identification is performed independently from any L0 or HLT1 trigger. This has the advantage that the HLT2 reconstruction is as close as possible to the offline event reconstruction, see Section 3.3.2. To identify muons, the tracks are extrapolated to the muon stations and a region of interest is

opened where muon hits are picked up. A track with a sufficient number of muon hits (dependent on the momentum) is identified as muon candidate [65].

These muon candidates are then combined using a kinematic fit [101] to form a common vertex with the quality  $\chi_{vtx}^2$ . The distribution of the vertex fit quality is shown in Figure 5.16 (a). A loose criteria ( $\chi_{vtx}^2 < 15$ ) selects almost 100% of the real dimuon vertices and reduces the rate to  $\sim 7$  kHz. Figure 5.16 (b) shows the dimuon invariant mass for minimum bias and selected signal  $B_s \rightarrow J/\psi\phi$  events. In minimum bias events, a combinatorial rise of the reconstructed invariant mass to low  $m_{\mu\mu}$  is observed. On these dimuon candidates, two selections are performed:

- a **lifetime unbiased** selection which selects the signal based on the muon transverse momentum ( $p_T$ ) and the dimuon invariant mass ( $m_{\mu\mu}$ ) and
- a **lifetime biased** selection which selects the dimuon candidates based on the muon impact parameter, the secondary vertex separation,  $m_{\mu\mu}$  and the dimuon  $p_T$ .

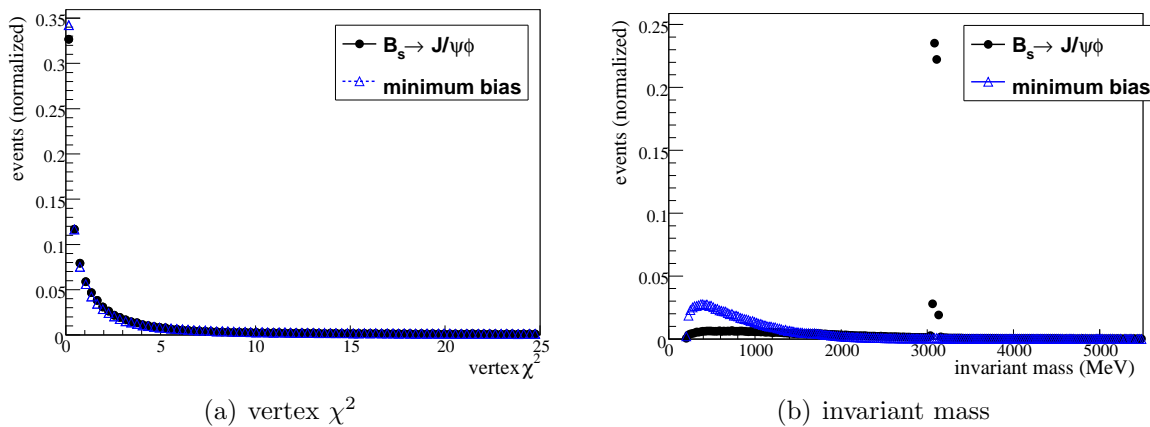


**Figure 5.16:** Dimuon candidates in HLT2 for selected  $B_s \rightarrow J/\psi\phi$  events and minimum bias: (a) Vertex  $\chi^2$  of the dimuon pair. In minimum bias events, the dimuon candidates originate mostly from the primary vertex. (b) Dimuon invariant mass. Both distributions are normalized to unit area.

### 5.4.1 Lifetime unbiased dimuon selection

Figure 5.17 (a) shows the dimuon invariant mass for selected  $B_s \rightarrow J/\psi\phi$  signal events. The  $J/\psi$  mass resolution is 24 MeV. The muon track candidates are fitted with a simplified Kalman track fit (see Section 5.1). As the track fit is only executed on the two daughter tracks from a dimuon candidate, the additional CPU time to the total HLT2 time budgeted is negligible. The  $J/\psi$  invariant mass resolution improves to 14 MeV, as shown in Figure 5.17 (b). The background consists mainly of real prompt  $J/\psi$  decays.

The transverse momentum spectrum of the muon candidates from  $J/\psi$  decays is shown in Figure 5.17 (c) for muons from selected  $B_s \rightarrow J/\psi\phi$  decays and minimum bias events. The muons from signal decays have on average a higher transverse momentum. The offline selection criteria of 500 MeV is clearly seen. In the  $p_T$  spectrum of the  $J/\psi$  candidates, Figure 5.17 (d), the offline selection criterion of 1 GeV is seen.

To select the events, the muon candidates are required to pass the same requirements as used in the offline  $B_s \rightarrow J/\psi\phi$  analysis ( $p_T(\mu) > 500$  MeV,  $p_T(J/\psi) > 1$  GeV). The excellent mass resolution allows a tight selection on the dimuon invariant mass of 70 MeV around  $m_{J/\psi}$ , which corresponds to  $\sim 5\sigma(m_{J/\psi})$ . This set of requirements selects  $B_s \rightarrow J/\psi\phi$  signal events with an efficiency of 98.1% and accepts minimum bias events with a rate of 200 Hz, measured on events which passed the previous trigger levels (in HLT1, the unbiased dimuon selection is required). This rate is well acceptable for the total HLT2 output rate [84]. Note that the hard requirement on the  $J/\psi$  invariant mass does not influence the sidebands of the  $B$ -mass, which are needed for the background determination in the  $\Phi_s$ -analysis<sup>3</sup> [29].

To complete the unbiased dimuon selection, other signals have to be added. As an example, a second selection with a 100 MeV window around the  $B_s$ -mass ( $\sim 5\sigma(m_{B_s})$ ) is added to trigger  $B_s \rightarrow \mu^+\mu^-$  events. This selection adds less than 10 Hz to the output rate and accepts selected  $B_s \rightarrow \mu^+\mu^-$  signal events with an efficiency of 95%.

<sup>3</sup>If sidebands in the  $J/\psi$  mass are needed, they can be included by a pre-scaled selection.

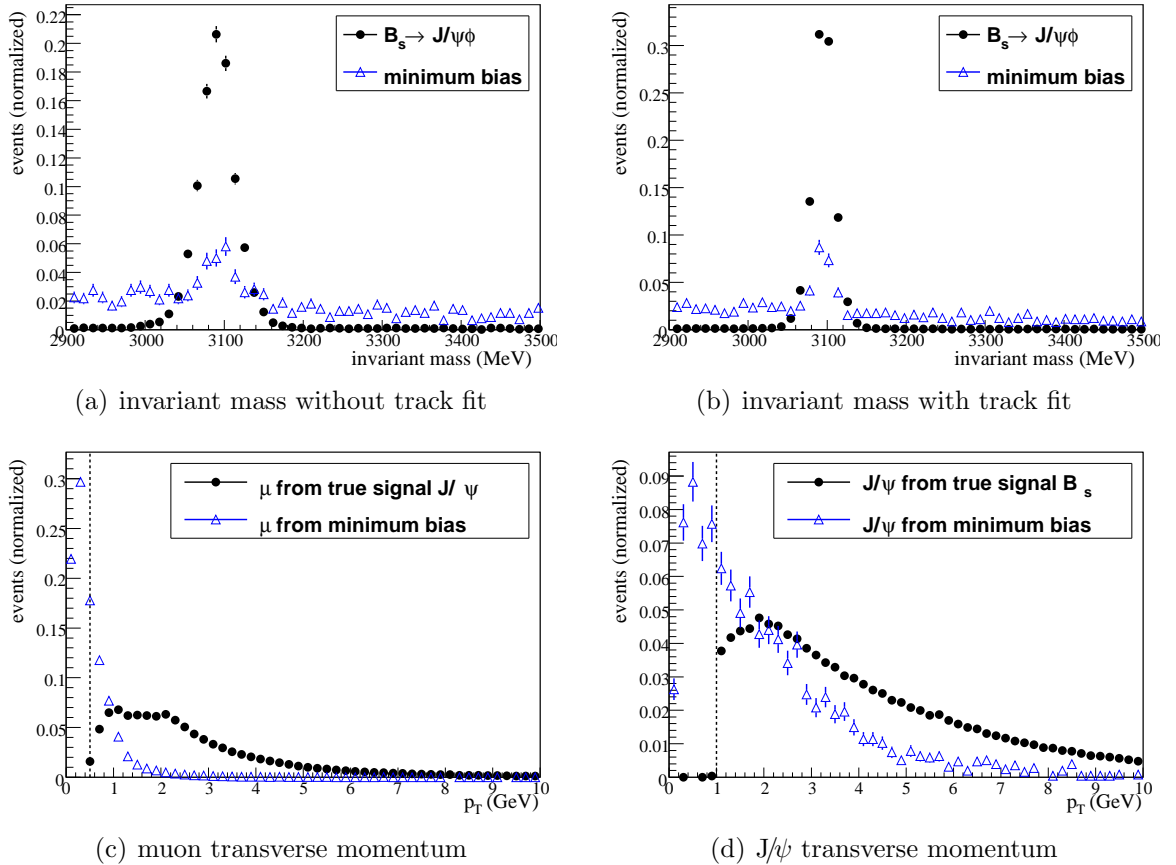


**Figure 5.17:**  $J/\psi$  candidate invariant mass for  $B_s \rightarrow J/\psi\phi$  signal and minimum bias events: (a) Without track fit, the resolution is 24 MeV. (b) For tracks fitted with the simplified track fit, the resolution is 14 MeV. (c) Transverse momentum of muons from signal (mean: 3.5 GeV) and minimum bias (mean 1.8 GeV). (d) Transverse momentum of the  $J/\psi$  for signal and minimum bias events. All histograms are normalized to unit area.

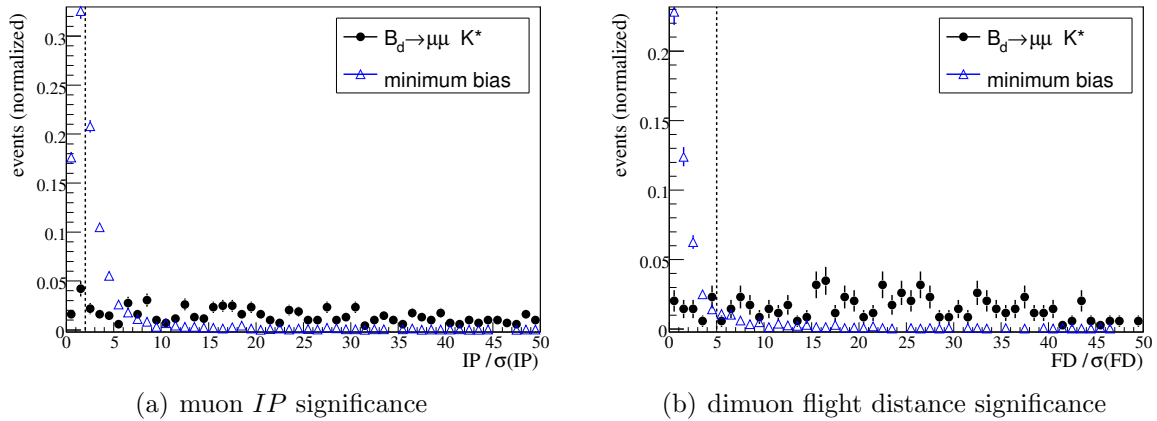


**Figure 5.18:** True signal  $B_d \rightarrow K^{*0} \mu^+ \mu^-$  events and minimum bias background: (a) Muon impact parameter significance. The requirement of  $IP/\sigma(IP) > 2$  is indicated as a dashed line. (b) Dimuon flight distance significance, the requirement of  $FD/\sigma(FD) > 5$  is indicated.

### 5.4.2 Lifetime biased dimuon selection

The lifetime biased dimuon selection is based on the impact parameter of the muons with respect to the primary vertex and the flight distance between the primary vertex and the  $B$  decay vertex. Instead of selecting on the value itself, the selection is based on the significance of the value, i. e., on the value divided by its error.

One of the prime decays triggered by the lifetime biased dimuon selection is the electroweak penguin decay  $B_d \rightarrow K^{*0} \mu^+ \mu^-$  (see Section 6.3) which is studied in the following. The muon impact parameter significance for true signal  $B_d \rightarrow K^{*0} \mu^+ \mu^-$  and minimum bias events is shown in Figure 5.18 (a). A clear separation between the signal and background is seen. Figure 5.18 (b) shows the flight distance significance.

To reject the background from wrong dimuon combinations, a minimum invariant mass is required ( $m_{\mu\mu} > 0.5 \text{ GeV}$ ). The transverse momentum of the dimuon system is further required to be above 2 GeV. This combination of criteria gives a selection efficiency for  $B_d \rightarrow K^{*0} \mu^+ \mu^-$  events of 85.3 % and accepts minimum bias events at a rate of 222 Hz. The selections presented here are optimized with respect to the discussion in Section 6.3.1.

### 5.4.3 Inclusive dimuon summary

Two dimuon selections for the second level of the software trigger have been presented. A lifetime biased selection which requires a separated secondary vertex and selects  $B_d \rightarrow K^{*0} \mu^+ \mu^-$  events with an efficiency of above 85 % (see Table 5.3). A lifetime unbiased selection with dedicated mass windows around the  $J/\psi$  and  $B_s$  mass have also been developed.  $B$  decays containing a  $J/\psi$  in the final state can be selected with an efficiency of above 98 % with respect to selected events which have passed the previous trigger levels. No selection criteria correlated with the  $B$ -lifetime has been used. The combination of these inclusive dimuon triggers selects minimum bias events with a rate of 400 Hz after the previous two trigger levels. The performance of both dimuon

selections is summarized in Table 5.3.

**Table 5.3:** Performance of the HLT2 selection for events which passed L0 and HLT1. The  $b \rightarrow J/\psi X$  channels are normalized to an HLT1 *unbiased dimuon* selection (see Section 5.3.4), the other channels are normalized to any HLT1 selection.

channel	unbiased dimuon	biased dimuon	OR of both
minimum bias	190 Hz	222 Hz	393 Hz
$B_s \rightarrow J/\psi \phi$	98.2 %	67.9 %	98.6 %
$B_d \rightarrow J/\psi K^{*0}$	98.3 %	68.1 %	98.7 %
$B^+ \rightarrow J/\psi K^+$	97.8 %	68.2 %	98.3 %
$B_s \rightarrow \mu^+ \mu^-$	93.8 %	89.7 %	98.1 %
$B_d \rightarrow K^{*0} \mu^+ \mu^-$	—	85.3 %	85.3 %

## 5.5 Trigger performance summary

The selection criteria which govern the performance of the LHCb trigger system have to be balanced between a good suppression of the minimum bias rate, the CPU time consumption on the Event Filter Farm (see Section 3.2) and a high selection efficiency on the  $B$ -decay channels relevant for the LHCb physics program. To evaluate the performance, the trigger efficiency is analyzed for a selection of benchmark channels which cover the different types of trigger strategies: channels which are triggered dominantly by the hadron line, the muon line and the electromagnetic line respectively.

### 5.5.1 Hadronic channels

The efficiency for the key  $B$  decays where the trigger selection relies on final state hadrons is presented for the following channels:

- $B_{(s)}^0 \rightarrow h^+ h^-$  which summarizes the decays  $B$  into two hadrons. The simultaneous analysis of the time dependent  $CP$ -asymmetry of  $B_s \rightarrow K^+ K^-$  and  $B_d \rightarrow \pi^+ \pi^-$  gives a handle to measure the CKM angle  $\gamma$  from the ratio of penguin to tree amplitudes [102, 103]. These decays have the highest efficiency of the hadronic channels as the  $p_T$  spectrum of the two-prong  $B$  decays is relatively hard.
- The  $B_s \rightarrow D_s^\mp K^\pm$  and  $B_s \rightarrow D_s^- \pi^+$  channels give another handle to measure the CKM angle  $\gamma$  [104], the channel  $B_s \rightarrow D_s^- \pi^+$  is also used for the calibration of the flavor tagging algorithms.
- The  $B_s \rightarrow \phi \phi$  is governed by a  $b \rightarrow s$  hadronic penguin diagram which is very sensitive to possible New Physics contributions in the weak mixing phase  $\Phi_s$  [105]. This decay is challenging to trigger because the four final state Kaons have a very soft transverse momentum spectrum.

**Table 5.4:** Summary of trigger performance. All efficiencies are normalized to selected and L0 hadron triggered events. The HLT1 rate corresponds to the hadron alley rate and the HLT2 rate to the rate of the inclusive topological trigger selection, see Section 3.3.2.

channel	Hardware Trigger	Software Trigger		total
	L0	HLT1	HLT2	
minimum bias	600 kHz	5 kHz	750 Hz	–
$B_{(s)}^0 \rightarrow h^+h^-$	50 %	78 %	80 %	31 %
$B_s \rightarrow D_s^- \pi^+$	44 %	68 %	83 %	25 %
$B_s \rightarrow \phi\phi$	34 %	53 %	78 %	14 %

In the hardware trigger, these events are selected by the L0 hadron trigger, efficiencies are between 34 % and 50 %. This is the main source of inefficiencies in the complete trigger chain. In HLT1, they are dominantly selected by the dihadron alley, in HLT2 by the inclusive topological trigger selection, see Section 3.3.2. The trigger efficiency for hadronic channels is summarized in Table 5.4, it ranges between 14 % for the four-prong decays  $B_s \rightarrow \phi\phi$  to 34 % for the two-prong decays in  $B_{(s)}^0 \rightarrow h^+h^-$ .

### 5.5.2 Muonic channels

In this section, the online selection efficiency of the key  $B$  decay channels with muons in the final state is presented for the complete trigger chain. A detailed discussion of the physics analyses and trigger issues of these channels can be found in Chapter 6, the trigger performance is summarized in Table 5.5.

### 5.5.3 Electromagnetic channels

$B$  decay channels whose trigger selection is based on electrons or photons in the final state are selected by the hardware trigger with an efficiency of the order of 70 %. At the current time, the software trigger selection both in HLT1 and HLT2 are only

**Table 5.5:** Summary of Trigger performance for muonic channels. In case two numbers are given, the first corresponds to the *lifetime biased* selection and the second to the *lifetime unbiased* selection. The non default selection is given in brackets. The HLT1 rate corresponds to the muon alley rate and the HLT2 rate to the inclusive dimuon rate.

channel	hardware trigger	software trigger		total
	L0	HLT1	HLT2	
minimum bias	225 kHz	17.2 kHz	393 Hz	–
$B_s \rightarrow J/\psi(\mu^+\mu^-)\phi(KK)$	93.9 %	(93.3 %) 86.4 %	98.2 %	(83.7 %) 79.8 %
$B_s \rightarrow \mu^+\mu^-$	97.1 %	98 % (92 %)	98.1 %	93.3 % (86.6 %)
$B_d \rightarrow K^{*0}\mu^+\mu^-$	86.3 %	92.1 %	85.3 %	67.5 %

as prototypes available. Therefore, it will not be discussed here in detail. Typical efficiencies are of the order of 70 % for the total software trigger selection, giving about 50 % total trigger efficiency.

# Chapter 6

## Potential of LHCb to measure New Physics in B decays

One of the main challenges of the LHCb trigger system is that the minimum bias rate has to be reduced by a factor 20 000 whereas the additional systematic error introduced by the trigger selections has to be kept at a minimum. The optimization of the trigger and analysis strategy strongly depend on each other: Both select a small fraction of the  $B$  decays in one channel, the critical point is to ensure that the trigger selects the same events as the analysis. To maximize the overlap, the trigger efficiency is evaluated on events that are accepted by the analysis of the respective channel. Similarly, the additional distortions the trigger introduces on the acceptances are minimized. It is an important aspect of the construction of the trigger system to adjust it as close as possible to the needs of the physics analyses. The trigger selection developed in Chapter 5 has been optimized according to the requirements of the LHCb core physics analyses whose trigger decision is based on muons.

This chapter first introduces the measurement of the weak phase  $\Phi_s$  in the interference between mixing and decay in the channel  $B_s \rightarrow J/\psi(\mu^+\mu^-)\phi(KK)$ . An introduction of the analysis strategy is given while the focus lies on the lifetime and decay angle dependent acceptances and their distortion introduced by the trigger selection. In Sections 6.2 and 6.3, the other key measurements of LHCb which are triggered by muons in the final state are discussed:  $B_s \rightarrow \mu^+\mu^-$  and  $B_d \rightarrow K^{*0}\mu^+\mu^-$ . The very different requirements of these analyses are studied.

### 6.1 $CP$ violation in the $B_s$ system

The interference between direct  $B_s$  decays to  $J/\psi\phi$  and decays via a  $B_s-\bar{B}_s$  oscillation give rise to a  $CP$  violating phase  $\Phi_s$ . In the Standard Model (SM), this phase is predicted to be  $\Phi_s = -2\beta_s$ , with the assumption that the penguin contributions are negligible, see Section 1.3.1. The precise measurement of this phase is one of the key goals of the LHCb experiment. New Physics can lead to new virtual contributions to the  $B_s-\bar{B}_s$  mixing diagram which may significantly modify  $\Phi_s$ , see for example Reference [106].

The most promising way to measure  $\Phi_s$  at LHC***b*** is a tagged, time-dependent angular analysis of the  $B_s \rightarrow J/\psi\phi$  decay [29, 107]. The process  $B_s \rightarrow J/\psi\phi$  is a decay of a pseudo-scalar into two vector mesons ( $P \rightarrow VV$ ) where the two mass eigenstates  $B_L$  (long lived in the SM) and  $B_H$  (short lived in the SM) decay with three complex amplitudes given by the three possible combinations of the polarizations of the decay products. In order to disentangle the two  $CP$  eigenstates, the three amplitudes need to be separated statistically through an angular analysis. The size of the time dependent  $CP$  asymmetry is proportional to  $\sin(\Phi_s)$ .

In this section, first the selection and trigger for  $B_s \rightarrow J/\psi(\mu^+\mu^-)\phi(KK)$  decays will be discussed. Then, the kinematic distributions of the signal and control channels before and after the trigger selection will be compared and the section will be concluded with an analysis of the distortion of  $B_s$  meson lifetime and angular acceptance introduced by the trigger selection.

The  $B_s$  physical properties used in the generation are summarized in Table 6.1. The data sets used in this section correspond to the expected number of  $B_s \rightarrow J/\psi\phi$  signal events collected by the LHC***b*** detector with an integrated luminosity of  $\mathcal{L} = 2 \text{ fb}^{-1}$ , see Section 2.4 for a discussion of the datasets.

**Table 6.1:**  $B_s$  parameters used in the generation of the  $B_s \rightarrow J/\psi(\mu^+\mu^-)\phi(KK)$  sample. The amplitudes are expressed in the transversity base. From the values of the  $B_s$  lifetime and  $\Delta\Gamma_s$ , one can derive the lifetime of the  $B_s$  mass eigenstates:  $\tau_H=1.538 \text{ ps}$  and  $\tau_L=1.391 \text{ ps}$ .

Parameter	Value
$B_s$ mass	5.3696 GeV
$B_s$ lifetime	1.461 ps
$\Delta m_s$	20 ps <sup>-1</sup>
$\Delta\Gamma_s$	0.06852 ps <sup>-1</sup>
$ A_{\parallel}(0) $	0.49
$\delta_{\parallel}$	2.50 rad
$ A_0(0) $	0.775
$\delta_0$	0.0 rad
$ A_{\perp}(0) $	0.4
$\delta_{\perp}$	-0.17 rad
$2\beta_s$	0.04 rad

### 6.1.1 Selection of $B_s \rightarrow J/\psi\phi$ events and trigger strategy

The selection of  $B_s \rightarrow J/\psi(\mu^+\mu^-)\phi(KK)$  and the two control channels  $B^+ \rightarrow J/\psi(\mu^+\mu^-)K^+$  and  $B_d \rightarrow J/\psi(\mu^+\mu^-)K^{*0}(K\pi)$  can be summarized as follows:

- maximize the signal yield while keeping the background at a reasonable level;
- minimize lifetime and angular acceptance distortions: the selection has been designed in such a way that the distortions are small and as similar as possible among signal and control channels;
- select the  $B_{u,d,s}$  mesons of the control and signal channels in such a way that their momentum distributions are similar: this is important in order to allow the tagging performance determined on control channels to be applied on the signal with a minimum of corrections.

The signal selection is summarized in Table 6.2, a detailed discussion of the selection of signal and control channels can be found in Reference [108]. To minimize the distortions in lifetime and angular acceptance, the selection has to avoid any criteria correlated with the  $B_s$  lifetime, such as the impact parameter of the track, and it has

**Table 6.2:** Summary of the  $B_s \rightarrow J/\psi(\mu^+\mu^-)\phi(KK)$  selection criteria (from [108]). Additionally to the requirements shown here, the muon candidates are required to have hits in the muon chambers, see [64] for details.

$J/\psi \rightarrow \mu\mu$ selection:		
$\mu^\pm$ :	$p_T$	$> 500 \text{ MeV}$
	$\chi_{\text{track}}^2/\text{nDoF}$	$< 5$
	$\Delta \ln \mathcal{L}_{\mu\pi}$	$> -5$
$J/\psi$ :	$p_T$	$> 1 \text{ GeV}$
	$\chi_{\text{vtx}}^2/\text{nDoF}$	$< 6$
	$ M(\mu\mu) - M(J/\psi) $	$< 42 \text{ MeV} (= 3\sigma)$
$\phi \rightarrow K^+K^-$ selection:		
$K^\pm$ :	$p$	$> 2 \text{ GeV}$
	$\chi_{\text{track}}^2/\text{nDoF}$	$< 10$
	$\Delta \ln \mathcal{L}_{K\pi}$	$> 0$
$\phi$ :	$p_T$	$> 1 \text{ GeV}$
	$\chi_{\text{vtx}}^2/\text{nDoF}$	$< 20$
	$ M(KK) - M(\phi) $	$< 12 \text{ MeV} (= 3\sigma)$
$B_s \rightarrow J/\psi\phi$ selection:		
$B_s$ :	$\chi_{\text{vtx}}^2/\text{nDoF}$	$< 5$
	$IPS$	$< 5$

to minimize requirements on the transverse momentum. A necessary requirement to perform a lifetime unbiased signal selection is the possibility to trigger without using  $B_s$  lifetime information. This is possible with the trigger strategy presented in Chapters 4 and 5.

Using a fully simulated Monte Carlo data sample (see Section 2.4), the efficiency to select true signal events is found to be

$$\epsilon_{tot} = \epsilon_{gen} \times \epsilon_{sel} = 2.78\%, \quad (6.1)$$

where  $\epsilon_{gen}$  is the generator level cut efficiency (see Section 2.4.2) and  $\epsilon_{sel}$  is the efficiency of the combination of acceptance, reconstruction and selection. The annual event yield  $\mathcal{S}$  is now expressed as follows:

$$\mathcal{S} = \mathcal{L} \times \sigma_{b\bar{b}} \times 2 \times f_B \times BR_{vis} \times \epsilon_{tot} \times \epsilon_{trig}, \quad (6.2)$$

where  $\mathcal{L} = 2fb^{-1}$  is the integrated luminosity in one nominal year of running ( $10^7s$ ),  $\sigma_{b\bar{b}}$  is the  $b\bar{b}$  production cross section at 14 TeV (see Section 1.4), the factor of two accounts for the pair production of  $b$ -quarks,  $f_B = 11 \pm 1.2\%$  is the hadronisation fraction for  $b \rightarrow B_s$  [109],  $BR_{vis} = (2.71 \pm 0.96) \times 10^{-5}$  is the visible branching fraction<sup>1</sup> [109] and  $\epsilon_{trig}$  is the combination of the trigger efficiencies of the three levels: L0, HLT1 and HLT2.

The optimal trigger selection for the signal  $B_s \rightarrow J/\psi\phi$  and the control channels is an inclusive, lifetime unbiased trigger only on the muons from the  $J/\psi$  decay. By selecting only on the  $J/\psi$  decay products, the signal and control channels are selected with identical trigger efficiencies. In the different trigger levels, the trigger selection is realized as follows:

- in the hardware trigger, using a L0 muon or dimuon decision,
- in HLT1, using the unbiased dimuon selection, see Section 5.3;
- and in HLT2 using the unbiased dimuon selection, see Section 5.4.

The total trigger efficiency,  $\epsilon_{trig}$ , is defined as the product of the efficiencies of the three trigger levels:

$$\epsilon_{trig} = \epsilon_{L0} \times \epsilon_{HLT1} \times \epsilon_{HLT2} = 93.9\% \times 86.4\% \times 98.2\% = 79.8\%, \quad (6.3)$$

where  $\epsilon_{L0}$  is normalized to events which are selected by the analysis and  $\epsilon_{HLT1}$ ,  $\epsilon_{HLT2}$  on events that passed the previous trigger stage. Using this combination of trigger selections, one expects an annual yield of 132 000 selected events. In the following, the influence of the trigger selections on the kinematic distributions, the proper time and angular acceptances will be studied.

---

<sup>1</sup>The visible branching fraction contains the branching fraction for the  $B_s \rightarrow J/\psi\phi$  decay and the subsequent  $\phi \rightarrow KK$  and  $J/\psi \rightarrow \mu\mu$  decays.

### 6.1.2 Kinematic distributions of signal and control channels

To apply the tagging properties determined on the control channels to the signal channel without having to apply large corrections, it is important that the selected  $B_s$  signal candidates have a similar distribution in phase space as the two flavor specific control channels. To study this, the transverse momentum spectrum of the  $B$  meson is analyzed in the channels  $B_s \rightarrow J/\psi\phi$ ,  $B^+ \rightarrow J/\psi K^+$  and  $B_d \rightarrow J/\psi K^{*0}$ . Figure 6.1 (a) shows these distributions for selected events without any trigger selection applied. The shape of the distribution of  $B_s \rightarrow J/\psi\phi$  and  $B^+ \rightarrow J/\psi K^+$  agree well. In the distribution of  $B_d \rightarrow J/\psi K^{*0}$ , a minimum  $p_T$  of 2 GeV is required to limit the combinatorial background. At low  $p_T$ , the shape of the  $p_T$  spectrum for  $B_d \rightarrow J/\psi K^{*0}$  differs slightly from the two other channels.

It is studied if the agreement changes when the trigger selections are applied. Figure 6.1 (b) shows the  $p_T$  distribution of  $B$  mesons from the three decay channels for events which passed the complete trigger chain. The spectrum of all three decay channels is shifted to higher transverse momenta. This is due to the usage of transverse momentum requirements in the trigger selection to discriminate between signal and minimum bias background. However, the  $p_T$  spectra of signal and control channels is shifted in the same way, the shapes of the distributions after trigger selection agree well. The difference in the shape of the distribution of  $B_d \rightarrow J/\psi K^{*0}$  remains unaltered by the trigger selection, the reason for the discrepancies remains to be studied.

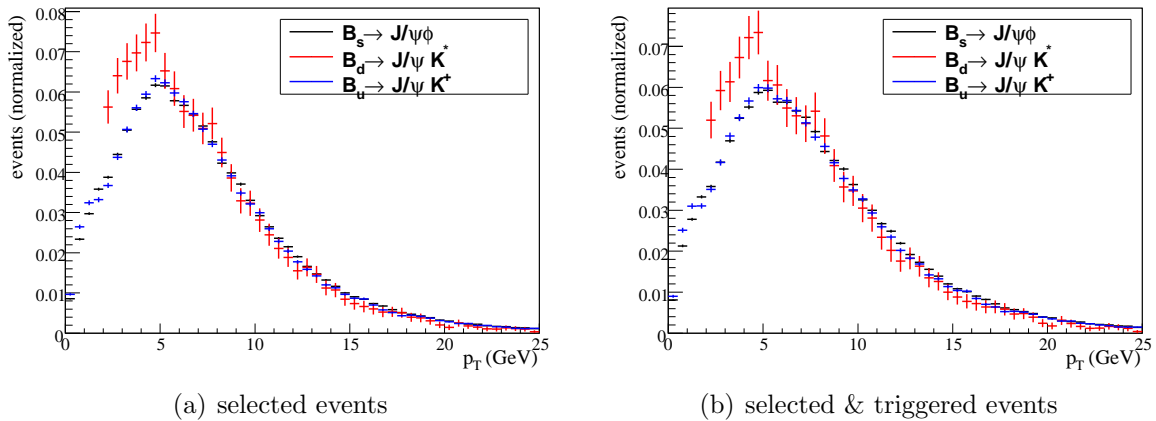


**Figure 6.1:** Transverse momentum spectrum of the  $B_s \rightarrow J/\psi\phi$  signal and control channels. (a) For events which passed the selection criteria (see Section 6.1.1) and (b) For events which additionally pass the complete trigger chain. The  $p_T$  spectra of signal and control channels agrees before and after the trigger selection.

### 6.1.3 Proper time distribution

The  $B_s$  proper time,  $t_{rec}$ , defined by the measured decay length  $d = \beta\gamma ct_{rec}$ , is given as

$$t_{rec} = m \cdot \frac{\vec{d} \cdot \vec{p}}{|p^2|}, \quad (6.4)$$

where  $m$  is the reconstructed invariant mass,  $|p|$  the momentum and  $\vec{d}$  the distance vector of the  $B_s$  candidate from the primary to the secondary vertex. The secondary vertex is uniquely defined by the decay products while there can be multiple primary vertices, reconstructed from all reconstructed tracks with a dedicated algorithm [77]. The primary vertex (PV) which has the smallest impact parameter relative to the  $B_s$  is used, see also Figure 3.5.

To determine the theoretical expectation of the proper time, one has to take into account that  $B_s$  and  $\bar{B}_s$  are a superposition of two states,  $B_L^0$  and  $B_H^0$  evolving with time with the lifetimes  $\tau_L$  and  $\tau_H$ , see Section 1.3.1. Using Equations 1.29-1.31, the probability of a decay is given by:

$$P(t_{av}) \propto \left( (1 - \cos \phi_s) \frac{|A_0(0)|^2}{2} + (1 - \cos \phi_s) \frac{|A_{\parallel}(0)|^2}{2} + (1 + \cos \phi_s) \frac{|A_{\perp}(0)|^2}{2} \right) e^{-t/\tau_H} + \left( (1 + \cos \phi_s) \frac{|A_0(0)|^2}{2} + (1 + \cos \phi_s) \frac{|A_{\parallel}(0)|^2}{2} + (1 - \cos \phi_s) \frac{|A_{\perp}(0)|^2}{2} \right) e^{-t/\tau_L}, \quad (6.5)$$

the parameters are defined in Section 1.3.1; their values are given in Table 6.1. There is thus a long and short lifetime component which differ in the Standard Model by 10 % ( $\Delta\Gamma/\Gamma \sim 10\%$ ).

Figure 6.2 (a) shows the generator level value of the  $B_s$  proper time for signal events which passed the selection criteria discussed in Section 6.1.1. The theoretical expectation, Equation 6.5, is shown as well, normalized to the same number of events. It is important for the  $\Phi_s$  analysis that the shapes of the two distributions agree. To evaluate this, the acceptance is calculated as a function of the proper time. It is defined as follows:

$$\text{acceptance} = \frac{N_{sel}(t_i)}{N_{th}(t_i)}, \quad (6.6)$$

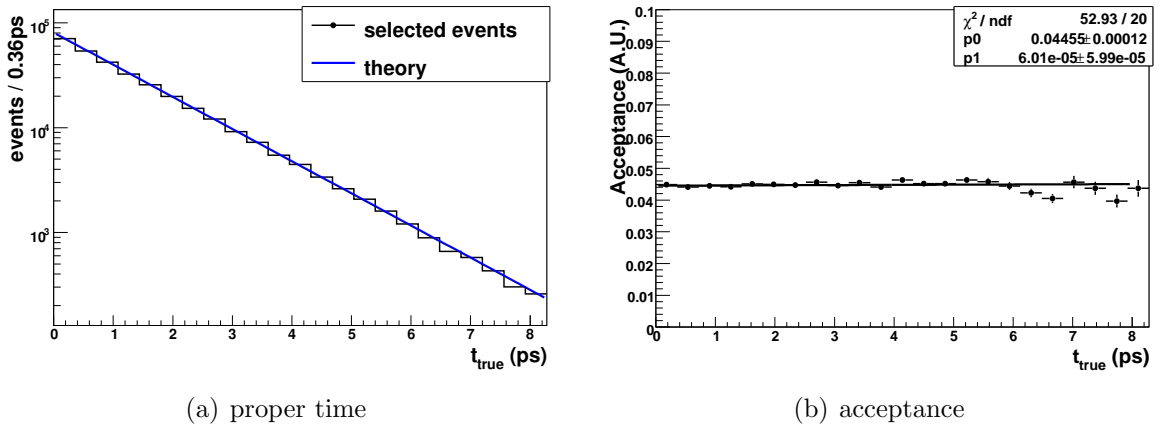


**Figure 6.2:**  $B_s \rightarrow J/\psi\phi$  signal events: (a) Generator level value of the  $B_s$  proper time for selected events. The theory expectation, Equation 6.5, is shown as well, normalized to the same area. (b) Proper time acceptance as defined in Equation 6.6. A straight line fitted to the histogram has no significant slope.

where nominator and denominator in a bin  $t_i$  in the proper time contain  $N_{sel}$  selected and  $N_{th}$  predicted events respectively. The absolute value of this ratio, determined by the normalization of the theoretical expectation, plays no role. The acceptance histogram is hence normalized to unit area. It is shown in Figure 6.2 (b). A straight line fit to the acceptance gives no significant slope. It can thus be concluded that the selection criteria summarized in Table 6.2 do not disturb the acceptance as a function of the proper time.

As next step, the effect of the trigger selection which is discussed in Section 6.1.1 is investigated. First the acceptance of triggered events is studied, it is defined as

$$\text{trigger acceptance} = \frac{N_{trig}(t_i)}{N_{th}(t_i)}, \quad (6.7)$$

where  $N_{trig}$  contain the events which are selected by the analysis and the trigger selection.  $N_{th}$  contain the expected events, with arbitrary normalization. Figure 6.3 (a) shows the trigger acceptance as a function of the proper time. The acceptance for triggered events slightly decreases with proper time, an effect which is already introduced by the hardware trigger. It remains for events which pass the software trigger selections.

To separate out the distortion introduced by the trigger selection, and to reduce statistical fluctuations, the triggered events are normalized to selected events, giving a lifetime dependent trigger efficiency, which is defined as:

$$\text{trigger efficiency} = \frac{N_{trig}(t_i)}{N_{sel}(t_i)}, \quad (6.8)$$

where  $N_{sel}$  contains selected events and  $N_{trig}$  selected events which additionally pass the trigger requirements. The trigger efficiency as a function of the lifetime is shown in

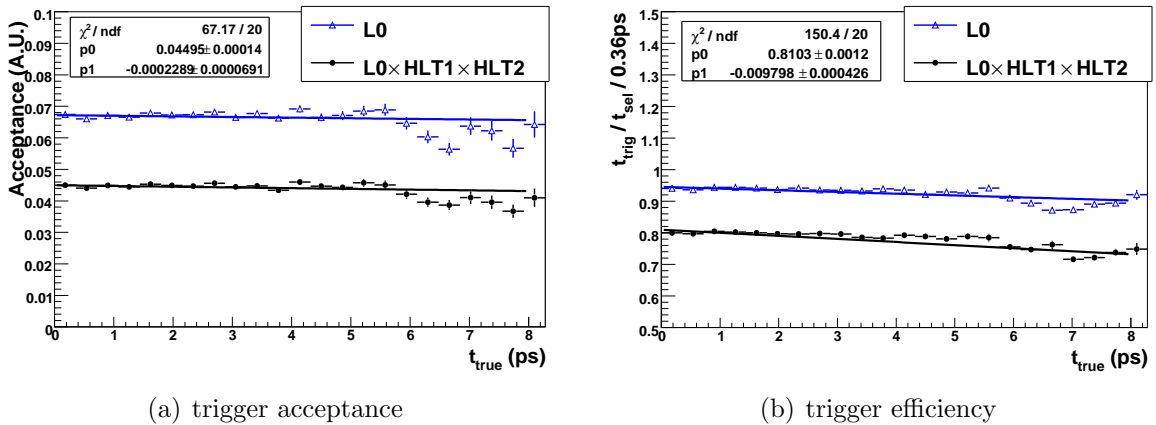


**Figure 6.3:** Selected  $B_s \rightarrow J/\psi\phi$  signal events: (a) Trigger acceptance dependent on proper time (Equation 6.7) for events which pass L0 (open triangles) and the complete trigger chain (closed points) with an arbitrary scale. (b) Trigger efficiency dependent on proper time (Equation 6.8). The fit details in both figures are given for the case L0 x HLT1 x HLT2.

Figure 6.3 (b). The same decrease as of the acceptance introduced by the L0 trigger is observed. As expected, it shows less statistical fluctuations.

Note that the lifetime acceptance is flat down to small proper times. Also in the trigger selection, where care has been taken not to introduce any bias on the  $B_s$  lifetime, no acceptance drop at small lifetimes is seen. This is particularly important for the determination of the lifetime resolution, see Section 6.1.5.

### 6.1.4 Angular acceptances

The decay  $B_s \rightarrow J/\psi\phi$  is a pseudo-scalar to vector-vector decay. Due to total angular momentum conservation, the final state is a superposition of three possible states with relative orbital momentum  $\ell = 0, 1, 2$  between the vector mesons. The  $CP$  eigenvalue of the final state, denoted  $\eta_f$ , is given by:

$$\begin{aligned} CP|J/\psi\phi\rangle_\ell &= \eta_f |J/\psi\phi\rangle_\ell \\ &= (-1)^\ell |J/\psi\phi\rangle_\ell. \end{aligned} \quad (6.9)$$

The three different angular momentum final states can be disentangled statistically by an analysis of the three decay product angles:  $\Omega = \{\theta, \varphi, \psi\}$ . The definition of these so called transversity angles is given in Section 1.3.1.

For this analysis, the precise shape of the angular distribution is essential. Therefore, as in the proper time analysis, the angular distribution determined from simulated events is compared to the theoretical expectation, which is given by Equation 1.28. The normalization of the theoretical curve is arbitrary. In Figure 6.4 (a, c, e), the distribution of the three angles in the transversity base is shown for selected events, together with the theoretical predictions, normalized to the same area. Some deviations in the shape between the reconstructed decay angles and the theoretical curve are seen. They have to be taken into account for the extraction of the physics parameters, see Section 6.1.5.

To investigate the distortions in detail, the angle dependent acceptance is calculated, analogously to Equation 6.6. In Figure 6.4 (b, d, f), the acceptances of these angles are shown, normalized to unit area. Distortions on the level of 10 % are observed, they are caused by the requirement that all four final state tracks are required to be within the geometrical acceptance of the LHC***b*** detector [29]. The effect of these distortions on physics parameters can be controlled if taken into account properly [110]. The angular acceptance on data can be tested using the  $B_d \rightarrow J/\psi K^{*0}$  control channel [111].

In the following, the effect of the trigger selection on the transversity angles will be studied. The angular dependent trigger efficiency is calculated, defined analogously to Equation 6.8. With this method, the additional distortions on the angles from the trigger selection can be studied. It is shown in Figure 6.5. The overall trigger efficiency of  $\sim 80\%$  is seen. Modifications of less than 2 % are introduced by the trigger. A straight line fit to the distributions gives no significant slope. It can therefore be concluded that the trigger selection as discussed in Section 5.3.2 and Section 5.4 does not introduce additional distortions on the distribution of the  $B_s \rightarrow J/\psi\phi$  decay angles.

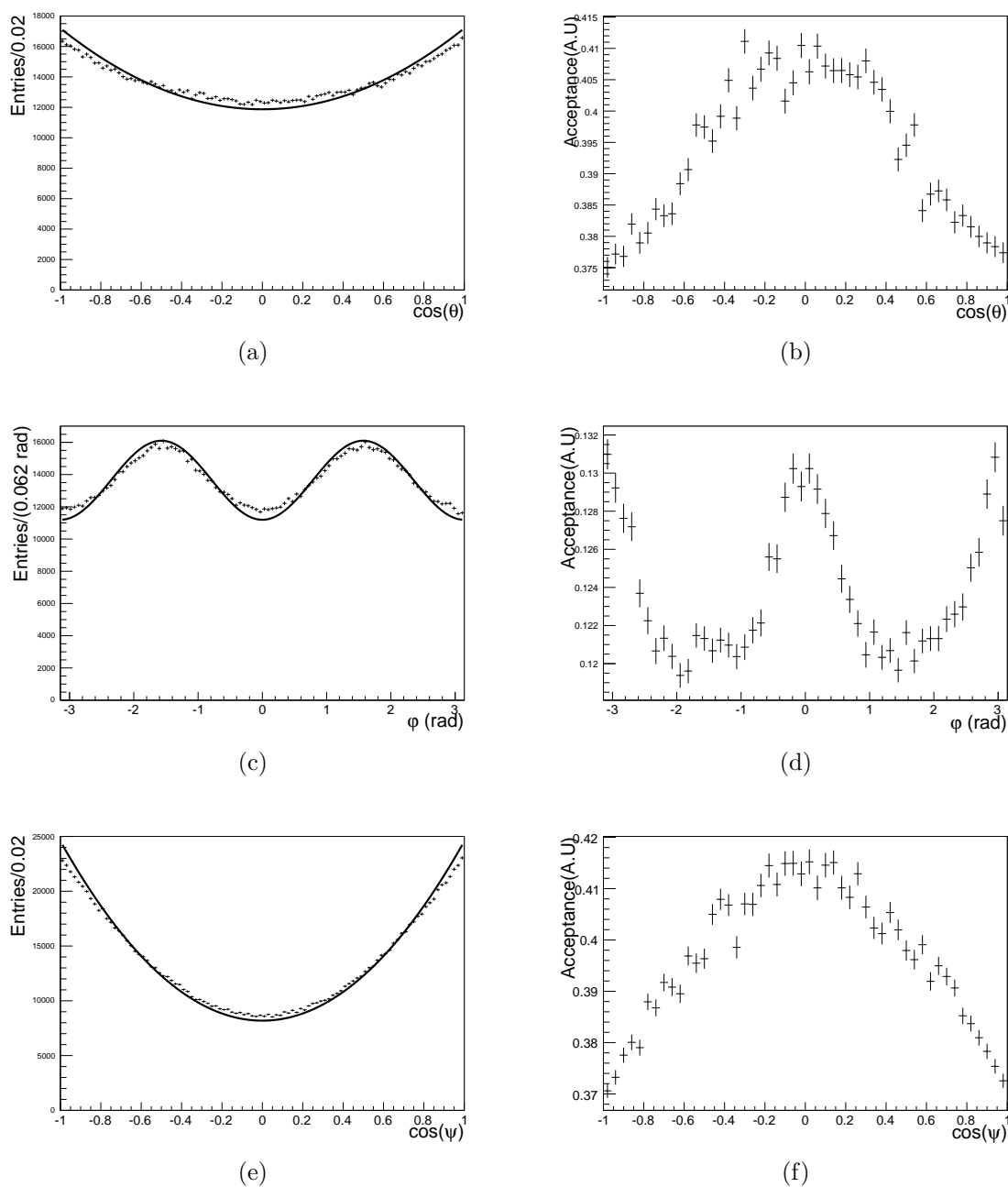


**Figure 6.4:**  $B_s \rightarrow J/\psi\phi$  decay angles in the transversity base. (left) Reconstructed angles for selected events compared to the theory function. (right) Acceptance in these angles obtained by a bin-by-bin division of the reconstructed angles and the theoretical expectation. Note the zero-suppressed  $y$ -axis on the right side.

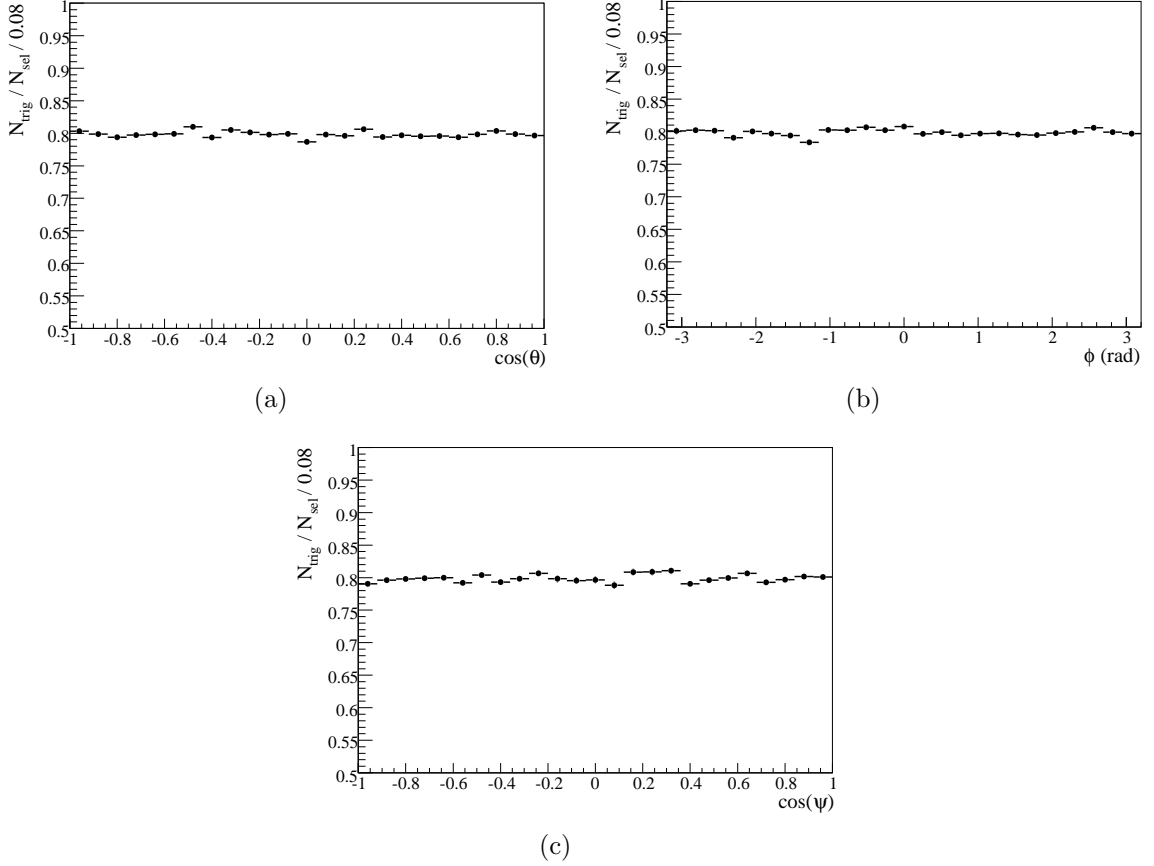


**Figure 6.5:** Trigger efficiency dependent on the transversity angles: The reconstructed angle for selected and triggered events is divided bin-by-bin with the angle for selected events. The trigger efficiency ( $L0 \times HLT1 \times HLT2$ ) shows no dependence on the angles, distortions are smaller than 2%.

### 6.1.5 Extraction of the $CP$ violating phase

The procedure for determining physics parameters from the data will be based on an unbinned likelihood fit method which involves a simultaneous proper time and angular analysis. Construction and normalization of the PDF is discussed in detail in [110]. In this section, only the general idea of the signal fit is outlined. The production flavor of the  $B_s$  (or  $\bar{B}_s$ ) meson is measured with a *flavor tagging* algorithm, discussed in reference [112]. The *flavor tagging* algorithm is calibrated using the  $B^+ \rightarrow J/\psi K^+$  and  $B_d \rightarrow J/\psi K^{*0}$  control channels.

The likelihood function for  $N$  events can be written generically as:

$$\mathcal{L} = \prod_e^N \mathcal{P}(t, m, \Omega, q; \lambda_{\text{phys}}, \lambda_{\text{det}}), \quad (6.10)$$

where  $t$  and  $m$  are the measured  $B_s$  proper time and reconstructed invariant mass,  $\Omega$  the three transversity angles and  $q$  the initial  $B$  flavor tag.  $\lambda$  is an abbreviation for all parameters determined by the fit.  $\lambda_{\text{phys}} = \{\Gamma_s, \Delta\Gamma_s, R_{\perp}, R_{\parallel}, \delta_{\perp}, \delta_{\parallel}, \Delta m_s, \Phi_s\}$

contains the physical parameters, as discussed in Section 1.3.1.  $\lambda_{\text{det}}$  are the detector parameters: mass resolution  $\sigma_m$ , proper time resolution  $\sigma_t$ , mistag rate  $\omega$  and background properties, they are discussed in reference [110]. Instead of maximizing the product, which is numerically unstable due to the large number of multiplications, the negative logarithmic likelihood is minimized.

The PDF consists of signal PDF,  $\mathcal{S}$ , and background PDF,  $\mathcal{B}$ :

$$\mathcal{P} = f_{\text{sig}}\mathcal{S} + (1 - f_{\text{sig}})\mathcal{B}, \quad (6.11)$$

where  $f_{\text{sig}}$  is the expected overall signal fraction and  $\mathcal{B}$  contains the prompt and long lived background categories. The signal PDF can be factorized as:

$$\mathcal{S}(X; \lambda) = \mathcal{S}_1(t, \Omega, q; \lambda) \mathcal{S}_2(m; \sigma_m), \quad (6.12)$$

where  $\mathcal{S}_2(m; \sigma_m)$  is the mass PDF and  $\mathcal{S}_1(t, \Omega, q; \lambda)$  is the angular and time dependent part of the PDF which contains the differential decay rates described in Section 1.3.1. The production flavor of the  $B_s$  is not perfectly known, it is measured with flavor tagging algorithms [112]. The signal PDF is written as (ommiting the normalization):

$$\mathcal{S}_1(t, \Omega, q; \lambda) \propto \left( \frac{1 + qD}{2} \right) \frac{d^4\Gamma}{dt d\Omega} + \left( \frac{1 - qD}{2} \right) \frac{d^4\bar{\Gamma}}{dt d\Omega}, \quad (6.13)$$

where  $q$  is the tagging decision,  $D = (1 - 2\omega)$  is the dilution and  $\omega$  is the mistag fraction. The angular and proper time acceptances (as discussed in Section 6.1.3 and Section 6.1.4) are taken into account in the fit as well as the proper time resolution. A detailed discussion can be found in [110].

To determine the sensitivity for  $\Phi_s$ , a three angle, time dependent tagged fit is performed on a toy Monte Carlo data sample including background, proper time resolution and imperfect tagging. Two toy Monte Carlo datasets are analyzed where the event numbers correspond to  $0.5 \text{ fb}^{-1}$  and  $2 \text{ fb}^{-1}$  respectively.

Figure 6.6 shows the proper time spectrum for selected  $B_s \rightarrow J/\psi\phi$  events together with a projection of the complete signal PDF onto the proper time axis. The  $CP$ -even and  $CP$ -odd components can be seen as dashed lines. The flat acceptance to small proper times is especially important for the correct determination of the background contribution in the fit. A lifetime biased trigger selection would lead to an acceptance drop for low proper times. In Figure 6.6, this would lead to a loss of events for low proper times and hence introduce large systematic uncertainties on the separation between signal and background in this region.

The sensitivity on  $\Phi_s$  is determined to be:

$$\mathcal{L} = 0.5 \text{ fb}^{-1} \quad : \quad \sigma(\Phi_s) = 0.060 \pm 0.005, \quad (6.14)$$

$$\mathcal{L} = 2 \text{ fb}^{-1} \quad : \quad \sigma(\Phi_s) = 0.030 \pm 0.002, \quad (6.15)$$

where only statistical errors are given. Figure 6.7 shows the statistical uncertainty on  $\Phi_s$  versus the integrated luminosity. The red line is an extrapolation from these two values, assuming the errors scale like  $1/\sqrt{\mathcal{L}_{\text{int}}}$ . The blue band shows the uncertainties coming from the  $b\bar{b}$  cross-section and the visible branching ratio of  $B_s \rightarrow J/\psi(\mu^+\mu^-)\phi(\text{KK})$ .

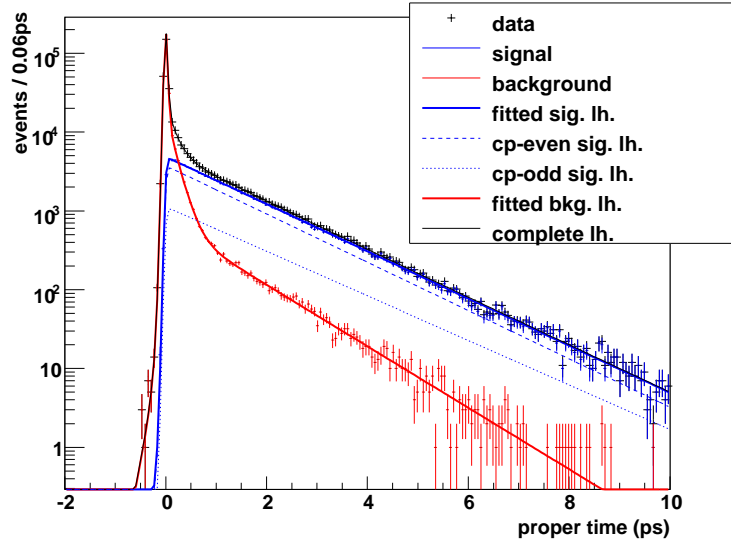


**Figure 6.6:** Proper time fit of the  $B_s \rightarrow J/\psi\phi$  selected sample. The different contributions of the fitted PDF are shown. (Figure from [110].)

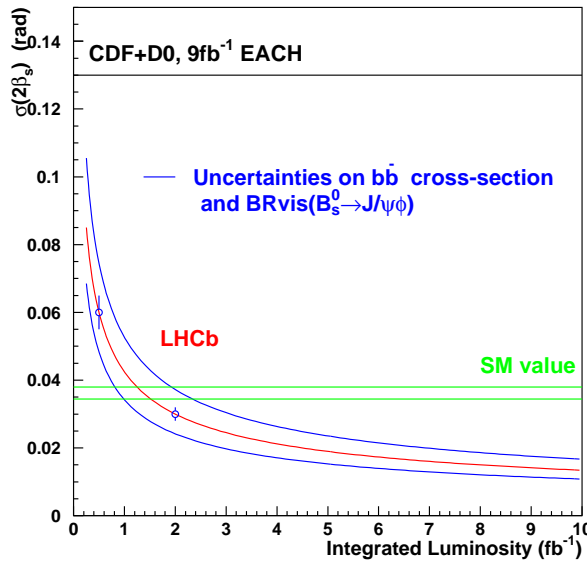


**Figure 6.7:** Red line: Statistical uncertainty on  $\Phi_s$  (in the legend denoted as  $2\beta_s$ ) versus the integrated luminosity. Blue band: uncertainties coming from the  $b\bar{b}$  cross-section and the visible branching ratio on  $B_s \rightarrow J/\psi(\mu^+\mu^-)\phi(KK)$ . The green band is the SM value, see Equation 1.27. (Figure from [29].)

The black line is the combined CDF/DØ uncertainty in 2008 scaled to an expected luminosity of  $18 \text{ fb}^{-1}$ , as expected by the Tevatron by 2010, see Section 1.3.1. With an integrated luminosity of  $2 \text{ fb}^{-1}$ , LHC***b*** can measure the weak mixing phase  $\Phi_s$  with a precision better than the magnitude of the Standard Model value.

## 6.2 Rare Decays: $B_s \rightarrow \mu^+ \mu^-$

The measurement of the branching ratio of the extremely rare decay  $B_s \rightarrow \mu^+ \mu^-$  (expected SM branching ratio:  $3.86 \pm 0.15 \times 10^{-9}$  [34]) has been identified as one of the measurements that are a sensitive probe for New Physics and constrain the parameter space of models describing physics beyond the Standard Model, see Section 1.3.2. In many Supersymmetric models, the  $B_s \rightarrow \mu^+ \mu^-$  branching ratio is highly enhanced with respect to the Standard Model.

### 6.2.1 Event selection and trigger strategy

The strategy in *LHCb* to search for the  $B_s \rightarrow \mu^+ \mu^-$  decay is described in References [33, 113]. The real challenge of this analysis is not the reconstruction of the signal but the suppression of the background. The basic concept is to apply a very efficient selection on signal events, removing the obvious backgrounds to reduce the size of the data sample to be analyzed. Then, each event is assigned a likelihood to be signal-like or to be background-like. This likelihood is defined to consist of three parts: an invariant mass part, an PID contribution which combines the information from the PID system and an geometrical contribution which is constructed from variables related to the vertex, pointing and isolation.

The most important aspect for the trigger selection of  $B_s \rightarrow \mu^+ \mu^-$  events is to efficiently select the signal. The high transverse momentum of the muons and their invariant mass provide a clear signature for the trigger selection. The following trigger selections are used:

- In the hardware trigger, L0, the signal events are selected by the single muon and the dimuon selection with an efficiency of 97 %.
- In the first level of the software trigger (HLT1) the combination of all muon trigger selections (see Section 5.3) selects events with an efficiency of 98 % evaluated on L0 accepted events. A very clean alternative which does not modify the acceptances is the HLT1 lifetime unbiased dimuon trigger selection (see Section 5.3.2). It selects signal events with an efficiency of 92 %.
- In the second level of the software trigger (HLT2), the lifetime biased and unbiased dimuon selections (see Section 5.4) can both be used to select  $B_s \rightarrow \mu^+ \mu^-$  events. The combined efficiency is 98.1 %, evaluated on HLT1 accepted events.

The total trigger efficiency,  $\epsilon_{trig}$ , is

$$\epsilon_{trig} = \epsilon_{L0} \times \epsilon_{HLT1} \times \epsilon_{HLT2} = 97.1 \% \times 98 \% \times 98.1 \% = 93.3 \%. \quad (6.16)$$

This excellent efficiency together with the fact that the signal can be triggered by several inclusive selections makes the analysis robust against inefficiencies, e. g., in the hardware trigger muon track finding.

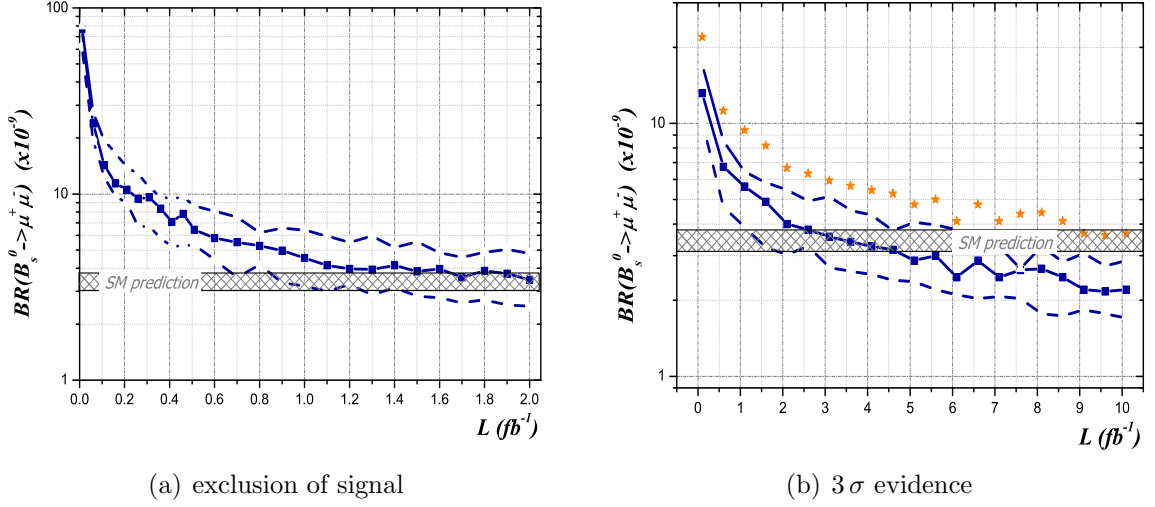


**Figure 6.8:** Branching ratio of the  $B_s \rightarrow \mu^+ \mu^-$  decay as a function of the luminosity. (a) If no signal is present, the branching ratio which is excluded at 90 % confidence level. (b) Evidence with a significance of  $3\sigma$ . Dashed lines indicate the 90 % probability region. Orange stars in (b) indicate the luminosity needed for a  $5\sigma$  discovery. (Figure from [33])

## 6.2.2 Sensitivity

A sensitive region with a sufficient geometrical likelihood and a mass window around the  $B_s$  mass ( $\Delta m < 60$  MeV) is defined. After applying loose signal selection criteria, 21 signal events (with the Standard Model branching ratio) and  $180_{-80}^{+140}$  background events are expected in  $2 \text{ fb}^{-1}$  of data (one year with nominal luminosity) [33]. The exclusion limits (or observation significance) is obtained by a combination of the information binned in the three likelihood variables using the  $CL_s$  method described in [114].

The potential of LHC***b*** with limited luminosity ( $\mathcal{L} < 0.1 \text{ fb}^{-1}$ ) is to exclude any significant excess of the branching ratio with respect to the Standard Model, as shown in Figure 6.8 (a). With  $\mathcal{L} \sim 1 \text{ fb}^{-1}$ , limit up to the Standard model prediction can be set if no signal is observed. In case of presence of a signal, the luminosity needed for a  $3\sigma$  evidence of a given branching ratio is shown at Figure 6.8 (b). About  $3 \text{ fb}^{-1}$  luminosity are needed for a  $3\sigma$  evidence if the branching ratio is within the Standard Model prediction. If the  $\mathcal{BR}$  is  $\sim 2 \times 10^{-8}$ , as predicted by some Minimal Supersymmetric Standard Model scenarios (see Section 1.3.2), with a luminosity of less than  $0.5 \text{ fb}^{-1}$ , LHC***b*** has the potential to claim a  $5\sigma$  discovery.

Irrespectively of whether the  $B_s \rightarrow \mu^+ \mu^-$  decay is found in agreement with the Standard Model prediction or not, the measurement will severely constrain the Higgs sector and the parameter space for the Minimal Supersymmetric Standard Model.

## 6.3 Radiative penguin transitions: $B_d \rightarrow K^{*0} \mu^+ \mu^-$

The decay  $B_d \rightarrow K^{*0} \mu^+ \mu^-$  is a flavor changing neutral current process which proceeds via a  $b \rightarrow s$  transition through a loop diagram (see Section 1.3.3). The branching ratio is  $1.10_{-0.26}^{+0.29} \cdot 10^{-6}$  [15]. New Physics (NP) processes can enter at the same level as the Standard Model processes, making the decay a sensitive probe of NP contributions. The branching ratio as a function of the squared dimuon invariant mass ( $q^2$ ) and the angular asymmetry constructed from the number of forward and backward emitted positive muons in the dimuon rest frame ( $A_{FB}$ ) and the zero crossing point of  $A_{FB}$  are the prime observables [115–117].

From the trigger point of view, the decay  $B_d \rightarrow K^{*0} \mu^+ \mu^-$  is challenging because the shape of the angular distributions is essential in the analysis. In contrast to  $B_s \rightarrow J/\psi \phi$ , the clear experimental signature of the  $J/\psi$  and as well of the two kaons is missing.

### 6.3.1 Event selection and trigger strategy

An investigation of the event selection required to isolate the candidates from the decay has been performed with Monte Carlo simulations of the signal and  $b\bar{b} \rightarrow \mu^+ \mu^- X$  background events [118, 119]. Both cut based and multivariate approaches have been investigated. No time dependence needs to be measured [41], so the selection can use lifetime biased criteria to isolate the signal. The challenge in the event selection is to minimize the bias introduced on the angular acceptances. The multivariate selection which is described in Reference [119], uses a Fisher discriminant [120] to separate signal and background events. The main variables used to construct the Fisher discriminant are: the  $B_d$  flight distance and pointing, the daughter impact parameter significances and particle identification likelihoods for all particles. The signal selection efficiency is 1.4% which results in 7100 events in  $2 \text{ fb}^{-1}$  with a background-to-signal ratio of 0.2. For the following discussion, the multivariate selection is used.

An angular efficiency that depends on  $\theta_L$  (the angle is defined in Figure 1.8) alters the measured value of  $A_{FB}$ , see Section 1.3.3. Any symmetric (about  $\theta_L = \pi/2$ ) effects on  $\theta_L$  result in a scaled value of  $A_{FB}$  but do not shift the zero crossing point. One of the central challenges of the analysis are corrections of the acceptance effects introduced by reconstruction, selection and trigger requirements. Figure 6.9 (figure from [41]) illustrates the sensitivity of  $\theta_L$  (and thus  $A_{FB}$ ) on a requirement of a minimum transverse momentum of both muons of 300 MeV in two different regions of  $q^2$ . For low  $q^2$ , a steep drop at  $\theta_L = 0, \pi$  to an efficiency of  $\sim 20\%$  is observed whereas for high  $q^2$ , the effect is more moderate.

Applying the requirements to only one of the muons  $p_T$  or to the dimuon  $p_T$  has been shown to cause significantly less bias in the angular distributions [41]. Figure 6.10 shows the effect of an 1.3 GeV requirement on one of the two final state muons, as it is imposed in the L0 single muon trigger. The distortion is far less significant (the efficiency drops to a minimum of  $\sim 70\%$ ) than the much lower requirement on both muons shown in Figure 6.9.

This discussion illustrates how potentially dangerous the selection criteria of the trigger are. However, to reduce the rate sufficiently, some requirements have to be

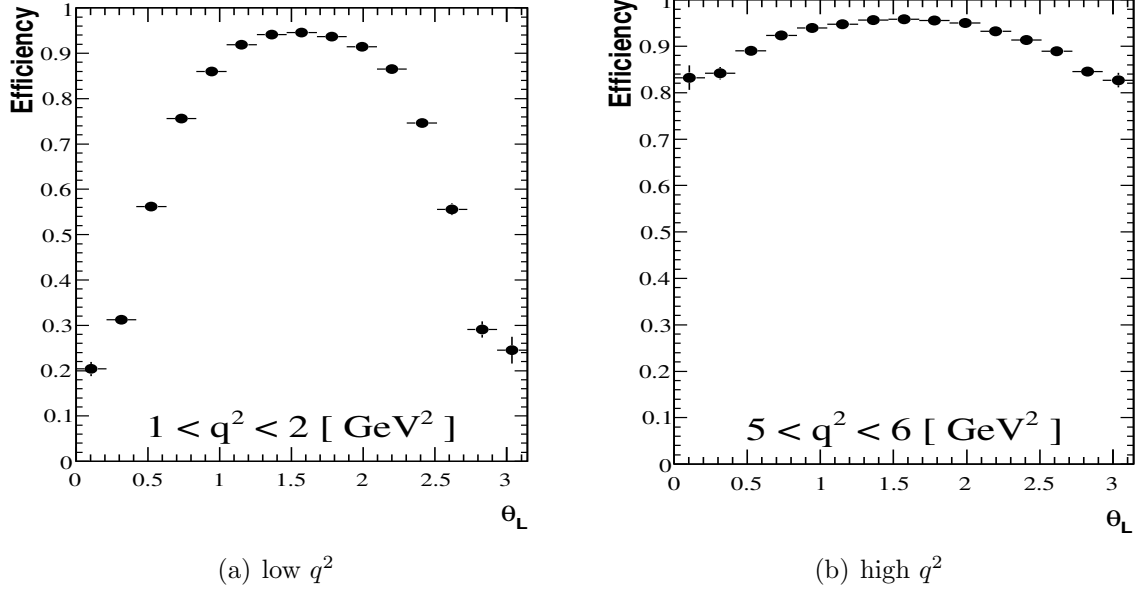


**Figure 6.9:** The effect of requiring a  $p_T$  greater than 300 MeV for both muons on the  $\theta_L$  efficiency for low and high dimuon invariant mass squared ( $q^2$ ). (Figure from [41]).

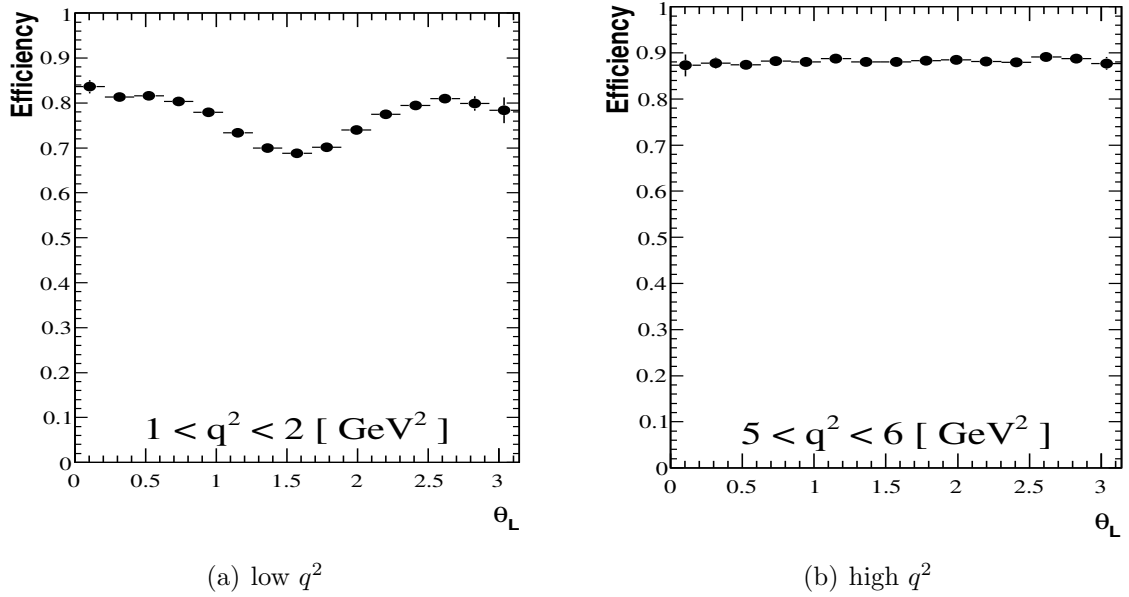


**Figure 6.10:** The effect of requiring a  $p_T$  greater than 1.3 GeV for one muon on the  $\theta_L$  efficiency for low and high dimuon invariant mass squared. (Figure from [41]).

made. As no requirement on the muons transverse momentum is made in the offline analysis, any requirement on  $p_T$  in the trigger introduces large inefficiencies and angular acceptance effects. Additionally, the dimuon invariant mass can become very small. The only remaining signature for the trigger selection is the displaced dimuon vertex.

The HLT1 lifetime biased dimuon selection is used in the first level of the software trigger, see Section 5.3.2. The rate is controlled with the requirement of a minimum impact parameter of the muons. In the setup of the HLT1 lifetime biased dimuon selection, any requirement on the  $p_T$  of the muons is carefully avoided. It gives an efficiency of 92.1 % on selected, L0 triggered signal events. For the second software trigger level (HLT2) a lifetime biased dimuon selection (see Section 5.4.2) is 85.3 % efficient in selecting signal events. The total trigger efficiency for selected  $B_d \rightarrow K^{*0} \mu^+ \mu^-$  events,  $\epsilon_{trig}$ , is:

$$\epsilon_{trig} = \epsilon_{L0} \times \epsilon_{HLT1} \times \epsilon_{HLT2} = 86.3\% \times 92.1\% \times 85.3\% = 67.5\%. \quad (6.17)$$

This online selection efficiency is significantly improved with respect to the previous trigger efficiency of about 52 % [41]. The main improvement is in the biased dimuon selection, see Section 5.4.2.

### 6.3.2 Sensitivity

With a few weeks of data taking at nominal luminosity, the signal yields from the multivariate analysis will be comparable to those from the B-factories [121, 122]. Both data derived and simulation based acceptance corrections for the effects introduced by the selection and trigger are being studied [41]. Uncertainties on these corrections are expected to give the dominant systematic uncertainties.

Several methods of extracting the physics parameters from the angular distribution of the signal are available, with increasing levels of complexity. Initially, the data will be analyzed with a binned counting analysis, and when the data and the detector are better understood, a fit to the angular distributions will be used. This gives access to

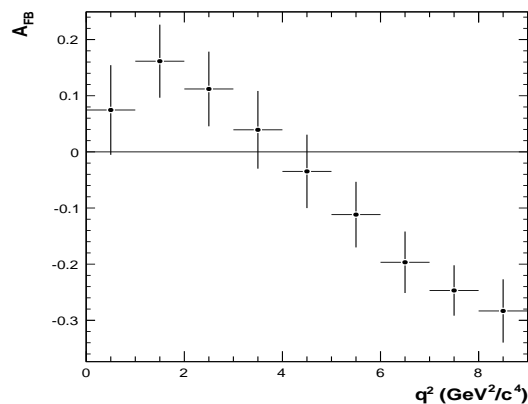


**Figure 6.11:** Estimated experimental sensitivity to  $A_{FB}$  as a function of the dimuon invariant mass ( $q^2$ ), assuming the SM in a binned counting analysis. Simulated data corresponding to  $2 \text{ fb}^{-1}$  are used. (Figure from [41].)

new observables. In Figure 6.11, taken from [41], the forward-backward asymmetry  $A_{FB}$  is determined with a binned counting analysis from a simulated data sample which corresponds to an integrated luminosity of  $\mathcal{L} = 2 \text{ fb}^{-1}$ .

# Chapter 7

## Summary and conclusion

In this thesis, a track reconstruction algorithm for the first stage of the LHCb software trigger system has been developed. At the software trigger input rate of 1 MHz, the algorithm uses the hardware trigger objects as seeds to open a search window in the main tracker. True signals are confirmed by a track with an efficiency above 95 %. The track reconstruction including the preparation of the detector data takes about 1 ms. This time is well within the time budget of the Event Filter Farm where the software trigger is executed. The relative momentum resolution of these online tracks is about 3 %. This improves the estimate of the hardware trigger system by an order of magnitude and thus allows tighter selections to reduce the large background of inelastic proton–proton collisions.

The track confirmation algorithm developed in this thesis allows to set up a trigger selection complimentary to the previously existing one which is based on the confirmation with tracks from the Vertex Locator. A trigger sequence to select hadrons has been set up which selects true signal decays with efficiencies between 50 % and 80 % and reduces the minimum bias rate by a factor of 130.

A simplified Kalman Filter based track fit was introduced to the software trigger which allows to discard trigger candidates with a bad track quality. This criteria reduces the output rate of the first software trigger level by 50 % while its relative efficiency on signal events is higher than 95 %.

The fast track reconstruction has been used to set up a *lifetime unbiased* trigger selection for muons. This selection does not modify the lifetime dependent acceptance of the  $B$  meson nor the angular dependent acceptance of its decay products. In the first level of the software trigger, this *unbiased* selection is 86 % efficient on true signal events, reducing the minimum bias rate from 220 kHz to 5 kHz. In the second level of the software trigger, the developed selection has an efficiency of 98 % normalized to the previous trigger levels, reducing the rate to below 200 Hz.

In the LHCb trigger strategy, the presented algorithm will be used as default to select muons, electrons and photons. For the selection of hadrons, it has proven to have similar performance as the existing algorithm based on vertex detector confirmation.

The analysis of the  $B_s \rightarrow J/\psi\phi$  decay to measure the  $CP$  violating phase  $\Phi_s$  from the interference between mixing and decay is considered as one of the key analyses of the LHCb experiment. It relies critically on the measurement of the angular structure of the decay products to determine their  $CP$  eigenvalue and on the flat acceptance of the  $B$  meson proper time. The trigger selections in this work are developed to minimize the effect of the trigger on the acceptances of decay angles and proper time. It has been shown that the trigger system can select these events with an efficiency of

$$\epsilon_{trig} = \epsilon_{L0} \times \epsilon_{HLT1} \times \epsilon_{HLT2} = 93.9\% \times 86.4\% \times 98.2\% = 79.8\%,$$

while introducing only a negligible bias on the acceptances. Compared to the previous  $B_s \rightarrow J/\psi\phi$  trigger selection efficiency of 58%, this is a significant improvement.

# List of Figures

1.1	Scheme of the unitarity triangle. . . . .	7
1.2	Global fit of all measurements contributing to $\mathbf{V}_{\text{CKM}}$ . . . . .	8
1.3	Dominant diagrams for $B_s - \bar{B}_s$ mixing. . . . .	9
1.4	Definition of the transversity angles. . . . .	12
1.5	Constraints on New Physics in the $(\text{Re}(\Delta_s), \text{Im}(\Delta_s))$ plane. . . . .	15
1.6	Feynman diagrams for the $B_s \rightarrow \mu^+ \mu^-$ decay. . . . .	16
1.7	Standard Model Feynman diagrams for the $B_d \rightarrow K^{*0} \mu^+ \mu^-$ decay. . . . .	17
1.8	Angles used to describe the decay $B_d \rightarrow K^{*0} \mu^+ \mu^-$ . . . . .	17
1.9	Production of heavy quarks at the LHC. . . . .	18
1.10	Cross sections for hard scattering versus $\sqrt{s}$ . . . . .	19
1.11	B meson production properties. . . . .	20
2.1	Number of interactions versus luminosity. . . . .	21
2.2	Layout of the LHCb detector. . . . .	22
2.3	Principal idea of the tracking system and magnetic field. . . . .	24
2.4	Layout of the Vertex Locator. . . . .	25
2.5	Sketch of the Velo $r$ and $\phi$ -sensors. . . . .	25
2.6	Trigger Tracker Layout . . . . .	26
2.7	Inner Tracker Layout . . . . .	27
2.8	Layout of the Outer Tracker. . . . .	27
2.9	Track classification. . . . .	29
2.10	Track reconstruction performance. . . . .	30
2.11	Side view of the calorimeter system. . . . .	32
2.12	Front view of the ECal and HCal. . . . .	33
2.13	Side view of the muon stations. . . . .	35
3.1	Track finding by the L0 muon trigger. . . . .	40
3.2	L0 muon trigger candidates properties. . . . .	41
3.3	General structure of the detector readout. . . . .	43
3.4	Overview of the LHCb trigger system. . . . .	44
3.5	Definition of the impact parameter. . . . .	45
4.1	Kinematic distribution of muon candidates. . . . .	55
4.2	Resolution of the L0- $\mu$ muon track hypothesis in T3. . . . .	56
4.3	Relative position in the ECal. . . . .	57
4.4	Momentum kick method used in the ECal. . . . .	58
4.5	Sketch of the three-by-three ECal cells in front of the HCal. . . . .	59

4.6	Hit Preparation in the single muon alley. . . . .	62
4.7	First search window in the $(x-z)$ projection. . . . .	64
4.8	Construction of a parabola with a hit in T2. . . . .	64
4.9	Stereo confirmation in the OT. . . . .	65
4.10	Track reconstruction efficiency. . . . .	69
4.11	Number of reconstructed tracks for electrons and photons. . . . .	70
4.12	Performance for single muon confirmation. . . . .	71
5.1	Kalman filter track fit scheme. . . . .	74
5.2	CPU time needed per track fit. . . . .	75
5.3	Relative momentum resolution for unfitted and fitted tracks . . . . .	76
5.4	Scheme of the hadron trigger alley. . . . .	77
5.5	Tuning of the search windows for the hadron track finding. . . . .	78
5.6	Transverse momentum spectrum and minimum bias retention. . . . .	79
5.7	2D Velo T-Station match. . . . .	79
5.8	Impact parameter distribution and minimum bias retention. . . . .	80
5.9	Track fit $\chi^2$ in the <i>hadron alley</i> for good and bad tracks. . . . .	82
5.10	Scheme of the muon trigger alley. . . . .	83
5.11	Tuning of the search windows for the muon track finding. . . . .	84
5.12	Transverse momentum distribution and minimum bias retention. . . . .	85
5.13	Tuning of the search windows in the muon recovery selection. . . . .	87
5.14	Dimuon invariant mass and $p_T$ . . . . .	88
5.15	Fit $\chi^2$ contributions. . . . .	89
5.16	Dimuon candidate properties. . . . .	91
5.17	$J/\psi$ candidate invariant mass and momentum spectrum. . . . .	92
5.18	Dimuon candidate impact parameter and flight distance. . . . .	93
6.1	$B_s \rightarrow J/\psi\phi$ signal and control channel $p_T$ spectra. . . . .	101
6.2	$B_s \rightarrow J/\psi\phi$ lifetime and lifetime acceptance. . . . .	102
6.3	$B_s \rightarrow J/\psi\phi$ proper time acceptance with trigger. . . . .	103
6.4	$B_s \rightarrow J/\psi\phi$ angular distribution and acceptance. . . . .	105
6.5	$B_s \rightarrow J/\psi\phi$ angular acceptance dependent trigger efficiency. . . . .	106
6.6	Proper time fit of the $B_s \rightarrow J/\psi\phi$ selected sample. . . . .	108
6.7	Expected sensitivity on $\Phi_s$ . . . . .	108
6.8	Expected sensitivity on $\mathcal{BR}(B_s \rightarrow \mu^+\mu^-)$ . . . . .	110
6.9	$B_d \rightarrow K^{*0}\mu^+\mu^-$ acceptance distortion by a $p_T$ requirement on both muons. . . . .	112
6.10	$B_d \rightarrow K^{*0}\mu^+\mu^-$ acceptance distortion by a $p_T$ requirement one muon. . . . .	112
6.11	Estimated experimental sensitivity to $A_{FB}$ . . . . .	113

# List of Tables

1.1	Boson content of the Standard Model. . . . .	4
1.2	Fermion content of the Standard Model. . . . .	4
1.3	Weak flavor quantum numbers. . . . .	5
1.4	Definition of the functions $h_k(t)$ and $f_k(\theta, \psi, \varphi)$ . . . . .	13
2.1	Position, depth and dimensions of the calorimeters. . . . .	33
2.2	Position and dimensions of the muon stations. . . . .	35
2.3	Summary of the used datasets. . . . .	37
3.1	L0 muon trigger minimum bias rate and efficiency. . . . .	41
3.2	Expected L0 hadron trigger minimum bias rate and efficiency. . . . .	42
3.3	Summary of the requirements of the global event veto. . . . .	42
4.1	Resolution of the muon track hypothesis at T3. . . . .	56
4.2	Resolution of the electron track hypothesis at the ECal. . . . .	58
4.3	Resolution of the electron track hypothesis at T3.a . . . . .	59
4.4	Resolution of the hadron track hypothesis at T3. . . . .	60
4.5	Average number of hits consistent with the track hypothesis. . . . .	62
4.6	Comparison of the performance of PatSeeding and TsaSeeding. . . . .	67
4.7	Optimized search window size. . . . .	68
4.8	Summary of the T-Confirmation performance. . . . .	71
5.1	HLT1 hadron rate and efficiency. . . . .	82
5.2	HLT1 muon rate and efficiency. . . . .	90
5.3	HLT2 dimuon performance. . . . .	94
5.4	Summary of trigger performance for hadronic channels. . . . .	95
5.5	Summary of trigger performance for muonic channels. . . . .	95
6.1	$B_s$ parameters used in the generation of the $B_s \rightarrow J/\psi\phi$ sample. . . . .	98
6.2	Summary of the $B_s \rightarrow J/\psi(\mu^+\mu^-)\phi(KK)$ selection criteria. . . . .	99



# Bibliography

- [1] S.L. Glashow. *Nucl. Phys.* **22** , 579 (1961).
- [2] A. Salam and J.C. Ward. *Phys. Lett.* **13** , 168 (1964).
- [3] S. Weinberg. *Phys. Rev. Lett.* **19** , 1264 (1967).
- [4] G. Bertone, D. Hooper and J. Silk. *Particle Dark Matter: Evidence, Candidates and Constraints*, (2004). arXiv:hep-ph/0404175v2.
- [5] G. R. Farrar and M. E. Shaposhnikov. *Phys. Rev. D* 50, 774 [hep-ph/9305275], (1994).
- [6] P. Huet and E. Sather. *Phys. Rev. D* 51, 379 (1995) [hep-ph/9404302], (1995).
- [7] M. B. Gavela, M. Lozano, J. Orloff and O. Pene. *Nucl. Phys. B* 430, 345 [hep-ph/9406288], (1994).
- [8] Y. Nir. *CP Violation in Meson Decays*. arXiv:hep-ph/0510413v1, (2005).
- [9] Y. Nir. *Probing new physics with flavor physics (and probing flavor physics with new physics)*. arXiv.org:0708.1872, (2007).
- [10] Halzen, F. and Martin, A. D. *Quarks and Leptons: An Introductory Course in Modern Particle Physics*. John Wiley & Sons Inc., (1984).
- [11] Nachtmann, O. *Phänomene und Konzepte der Elementarteilchenphysik*. Friedr. Vieweg & Sohn, (1986).
- [12] Perkins, D. H. *Introduction to High Energy Physics*. Cambridge University Press, 4th edition, (2000).
- [13] E. Gamiz et al. *High En. Phys.* 01 060, (2003).
- [14] Yao, W.-M. et al. *J. Phys.* **G33** , 1–1232 (2006, and 2007 partial update for the 2008 edition available on the PDG WWW pages (URL: <http://pdg.lbl.gov/>)).
- [15] Amsler, C. et al. *Physics Letters B* 667 , 1–1232 (2008).
- [16] S.L. Glashow, J. Iliopoulos and L. Maiani. *Phys. Rev.* **D2** , 1285 (1970).
- [17] N. Cabibbo. *Phys. Rev. Lett.* **10** , 531–532 (1963).

- [18] Kobayashi, Makoto and Maskawa, Toshihide. *Prog. Theor. Phys.* **49** , 652–657 (1973).
- [19] Wolfenstein, L. *Phys. Rev. Lett.* **51** , 1945 (1983).
- [20] Jarlskog, C. *Commutator of the quark mass matrices in the standard electroweak model and a measure of maximal CP violation.* *Phys.Rev.Lett.* **55** 1039, (1985).
- [21] J. Van Tilburg. *Track simulation and reconstruction in LHCb.* CERN-THESIS-2005-020, (2005).
- [22] CKMfitter group, J. Charles et al. *updated results and plots available at: <http://ckmfitter.in2p3.fr>.* *Eur. Phys. J. C*41, 1-131, hep-ph/0406184, (2009).
- [23] Sozzi, M. *Discrete Symmetries and CP violation: From experiment to theory.* Oxford University Press, (2008).
- [24] Branco, G. *CP violation.* Oxford University Press, (1999).
- [25] A. Lenz. *Theoretical status of  $B_s$ -mixing and lifetimes of heavy hadrons.* arXiv:0705.3802v2 [hep-ph], (2007).
- [26] Belle collaboration, K. Abe et al. *Improved measurement of direct CP violation in  $B \rightarrow K^+\pi^-$ .* Belle-Conf-0523, (2005).
- [27] BaBar collaboration, B. Aubert et al. *Direct CP violation asymmetry in  $B \rightarrow K^+\pi^-$ .* *Phys.Rev.Lett.* **93**, **131801**, (2004).
- [28] A. Lenz, U. Nierste . *Theoretical Update on  $B_s$ - $\bar{B}_s$  Mixing.* hep-ph/0612167v3, (2006).
- [29] J. Albrecht et al. *Road map for the measurement of mixing induced CP violation in  $B_s \rightarrow J/\psi\phi$  at LHCb.* LHCb/ROADMAP3-001 document in preparation, (2009).
- [30] The CDF collaboration. *First Flavor-Tagged Determination of Bounds on Mixing-Induced CP Violation in  $B_s \rightarrow J/\psi\phi$  Decays.* *Phys. Rev. Lett.* **100**, 161802, (2008).
- [31] The CDF collaboration. *An updated measurement of the CP violating phase  $\Phi_s$ .* CDF/ANAL/BOTTOM/PUBLIC/9458, (2009).
- [32] The D0 collaboration. *Measurement of  $B_s$  mixing parameters from the flavor-tagged decay  $B_s \rightarrow J/\psi\phi$ .* hep-ex, arXiv:0802.2255v1, (2008).
- [33] D. Martinez et al. *Analysis of the decay  $B_s \rightarrow \mu^+\mu^-$  at LHCb.* LHCb/ROADMAP1-002 document in preparation, (2009).
- [34] G. Buchalla et al.  *$B$ ,  $D$  and  $K$  decays, report on the CERN workshop: Flavor in the era of the LHC.* arXiv:0801.1833, (2008).
- [35] H.E. Logan, U. Nierste.  *$B_{s,d} \rightarrow \ell^+\ell^-$  in a Two-Higgs-Doublet Model.* arXiv:hep-ph/0004139, (2000).

- [36] J.F. Gunion, H.E. Haber, G.L. Kane and S Dawson. *Errata for The Higgs Hunter's Guide*. arXiv:hep-ph/9302272, (1993).
- [37] T. Aaltonen et al[CDF collaboration]. Phys. Rev. Lett. **100** 101802, (2008).
- [38] D0 collaboration. D0 public note 5344-CONF, (2007).
- [39] U. Egede, T. Hurth, J. Matias, M. Ramon, W. Reece. *New observables in the decay mode  $B_d \rightarrow K^{*0} \mu^+ \mu^-$* . arXiv:0807.2589, CERN-TH/2008-155, (2008).
- [40] W. Reece, U. Egede. *Performing the full angular analysis of  $B_d \rightarrow K^{*0} \mu^+ \mu^-$  at LHCb*. LHCb/PUB-2008-041, (2008).
- [41] J. Dickens et al. *Roadmap for the analysis of  $B_d \rightarrow K^{*0} \mu^+ \mu^-$* . LHCb/ROADMAP2-001 document in preparation, (2009).
- [42] J. Nardulli. *Reconstruction of two-body B decays in LHCb*. CERN-THESIS-2007-063, (2007).
- [43] P. Nason et al. *Bottom Production*. arXiv:hep-ph/0003142v2, (2001).
- [44] G. Altarelli and M.L. Mangano (editors). *Standard model physics (and more) at the LHC*. CERN-2000-004, (2000).
- [45] R. Hierck. *Optimisation of the LHCb detector*. CERN-THESIS-2003-025, (2003).
- [46] The LHCb Collaboration. *LHCb Technical proposal*. CERN-LHCC/98-4, 1998.
- [47] The LHCb Collaboration. *The LHCb Detector at the LHC*. 2008 JINST 3 S08005.
- [48] The LHCb Collaboration. *LHCb Technical proposal*. CERN-LHCC/2000-007, 1999.
- [49] ARGUS collaboration, H. Albrecht et al. *Observation of  $B^0 - \bar{B}^0$  mixing*. Phys.Lett **B192** 245, (1987).
- [50] The LHCb collaboration. *LHCb Velo technical design report*. CERN-LHCC/2001-011, (2001).
- [51] The LHCb collaboration. *LHCb Inner Tracker design report*. CERN-LHCC/2002-029, (2003).
- [52] The LHCb Collaboration. *LHCb Outer Tracker Technical Design Report*. CERN/LHCC-2001-024, (2001).
- [53] G. v. Apeldoorn et al. *Beam Tests of Final Modules and Electronics of the LHCb Outer Tracker in 2005*. LHCb/PUB-2005-076, (2005).
- [54] O. Callot. *Improved robustness of the Velo tracking*. LHCb-2003-017, (2003).
- [55] S. Hansmann-Menzemer, O. Callot. *The Forward Tracking: Algorithm and Performance Studies*. CERN-LHCb-2007-015, (2007).

- [56] M. Schiller. *LHCb tracking Twiki page*. <https://twiki.cern.ch/twiki/bin/view/LHCb/LHCbTrackingStrategies>, (2008).
- [57] Needham, M. *Clone Track Identification using the Kullback-Liebler Distance*. CERN-LHCb-2008-002, (2008).
- [58] Hansmann-Menzemer, S. *Status Pattern Recognition*. LHCb tracking workshop, 28-February 2008.
- [59] The LHCb Collaboration. *LHCb Calorimeters Technical Design Report*. CERN/LHCC-2000-036.
- [60] The LHCb Collaboration. *LHCb Trigger System Technical Design Report*. CERN/LHCC-2003-031.
- [61] The LHCb Collaboration. *LHCb Muon Technical Design Report*. CERN/LHCC-2000-037.
- [62] G. Charpak et al. *The use of Multiwire Proportional Counters to Select and Localize Charged Particles*. Nucl. Instr. Meth. **62** 235, (1968).
- [63] The LHCb Collaboration. *Addendum to the Muon Technical Design Report*. CERN/LHCC-2003-002, (2003).
- [64] Polycarpo, E., Gandelman, M. . *The performance of the LHCb muon identification procedure*. LHCb/PUB-2007-145, (December 2007).
- [65] Satta, A. *Muon identification in the LHCb High Level Trigger*. CERN-LHCb-2005-071, (September 2005).
- [66] N. Metropolis, S. Ulam. *The Monte Carlo Method*. Journal of the American Statistical Association 44 (247): 335341, (1949).
- [67] The LHCb Collaboration. *LHCb Computing Technical Design Report*. CERN/LHCC-2005-019, (2005).
- [68] G. Barrand et al. *GAUDI - A software architecture and framework for building HEP data processing applications*. Comput. Phys. Commun. 140 45, (2001).
- [69] T. Sjöstrand et al. *PYTHIA*. Computer Physics Commun.**135** 238., (2001).
- [70] A. Ryd et al. *EvtGen A Monte Carlo Generator for B-Physics*. BAD 522 v6., (2005).
- [71] I. Belyaev et al. *Simulation application for the LHCb experiment*. physics/0306035, (2003).
- [72] GEANT 4 collaboration. Nucl. Inst. and Methods **A 506** (2003), 250., (2003).
- [73] S. Ponce et al. *Detector Description Framework in LHCb*. physics/0306089, (2003).

- [74] H. Dijkstra. *Information on DSTs of benchmark channels*. <http://lhcb-trig.web.cern.ch/lhcb-trig/HLT/benchmark.pdf>.
- [75] The LHCb Collaboration. *LHCb Online Technical Design Report*. CERN/LHCC-2002-011, (2002).
- [76] Barczyk, A; Haefeli, G; Jacobsson, R; Jost, B; Neufeld, N . *1 MHz Readout*. CERN-LHCb-2005-062.
- [77] Krasowski, M. et al. *Primary Vertex Reconstruction*. LHCb/PUB-2007-11, (2007).
- [78] N. Zwahlen. *HLT hadronic L0 confirmation*. CERN/LHCb-2006-040.
- [79] Amato, S., Satta, A., Souza de Paula, B., de Paula, L. *Hlt1 Muon Alley Description*. CERN-LHCb-2008-058, (November 2008).
- [80] A. Perez-Calero, H. Ruiz. *The muon+track alley of the LHCb High Level Trigger*. CERN-LHCb/PUB-2008-075, (2008).
- [81] K. Senderowska, M. Witek, A. Zuranski. *HLT Electromagnetic Alley*. CERN-LHCb/PUB-2009-001, (April 2009).
- [82] S. Barsuk.  $\gamma / \pi^0$  separation at high  $E_T$ . CALO software meeting, 20.05.2003.
- [83] G. Krocker, J. Albrecht, S. Hansmann-Menzemer. *Fast Fit in inclusive  $B \rightarrow Dh$  selection - first results of PatSeeding on unused hits*. Presented at the LHCb tracking workshop, 16. February 2009.
- [84] H. Dijkstra. *HLT summary*. Presented at the 36<sup>th</sup> LHCb software week, 20. March 2009.
- [85] F. Teubert. *HLT2 inclusive selections and muon channels*. Joint physics and HLT meeting, 30.03.2009.
- [86] G. Guerrer. *The topological trigger*. LHCb plenary talk, (Nov. 2008).
- [87] M.H. Lieng. *An inclusive  $\phi$  stream for the LHCb high level trigger, DC06 analysis*. CERN/LHCb-2009-010.
- [88] R. Forty, C. Jones, M. Patel. *RICH particle identification for the trigger*. LHCb/INT-2005-052, (2005).
- [89] K. Vervink. *Inclusive  $\phi$  trigger for HLT2*. Presentation at LHCb TRec meeting, (30. March 2009).
- [90] Forty, R., Needham, M. *Standalone Track Reconstruction in the T-Stations*. CERN-LHCb-2007-022, (2007).
- [91] Forty, R., Needham, M. *Updated Performance of the T seeding*. CERN-LHCb-2007-023, (2007).

- [92] Callot, O., Schiller, M. *Pat Seeding: A Standalone Track Reconstruction Algorithm*. CERN-LHCb-2008-042, (2008).
- [93] Schiller, M. *Standalone track reconstruction for the outer tracker of the LHCb experiment using a cellular automaton*. Diploma Thesis, Universitat Heidelberg, (July 2007).
- [94] Kalman, R.E. *A new approach to linear filtering and prediction problems*. Trans. ASME J. Bas. Eng. **D82** (1960) 35.
- [95] Frühwirth, R. *Application of Kalman Filtering to track and vertex fitting*. Nucl. Instrum. Meth. A **262** (1987) 444.
- [96] R. Van der Eijk. *Track reconstruction in the LHCb experiment*. CERN-THESIS-2002-032, (2005).
- [97] Hulsbergen, W.. *Status of simplified geometry for track fitting*. Presented at the LHCb software week, (May 2007).
- [98] G. Krocker, J. Albrecht, M. Schiller, S. Hansmann-Menzemer. *Update on HLT Ghosts - A very fast clone killing algorithm*. Presentation at LHCb TRec meeting, (27. April 2009).
- [99] Callot, O. *News from the Pat packages*. LHCb tracking workshop in Heidelberg, 22-February 2007.
- [100] J.A. Hernando, D. Martinez, X. Cid, G. Guerrer, A. dos Santos, J. Albrecht. *The 'Hadron Alley' description*. CERN-LHCb/PUB-2009-034, (April 2009).
- [101] Ruiz, H. *Fast tools for vertexing and geometry calculations for the HLT*. CERN-LHCb-2005-013, (January 2006).
- [102] R. Fleischer.  *$B_{s,d} \rightarrow \pi\pi, \pi K, KK$ : Status and Prospects*. arXiv:0705.1121, (2007).
- [103] A. Carbone et al. *Charmless charged two-body B decays in LHCb*. LHCb/PUB-2007-059, (2007).
- [104] J. Borel, L. Nicolas, O. Schneider, J. Van Hunen. *The  $B_s \rightarrow D_s^- \pi^+$  and  $B_s D_s K$  selections*. LHCb/PUB-2007-017, (2007).
- [105] S. Amato, et al. *LHCb's sensitivity to New CP-violating Phases in the Decay  $B_s \rightarrow \phi\phi$* . CERN-LHCb-2007-047, (2007).
- [106] U. Nierste. *Bounds on new physics from  $B_s$  mixing*. Int. J. Mod. Phys. 22, 5986, (2008).
- [107] Dighe, A.S., Duniety, I., Fleischer, R. . Eur. Phys. J. C6, 647 (1999) and hep-ph/9804253.
- [108] Clavi, M., Khanji, B., Lanfranchi, G., Leroy, O. and Poss, S. . *Lifetime unbiased selection of  $B_s \rightarrow J/\psi\phi$  and related control channels:  $B_d \rightarrow J/\psi K^{*0}$  and  $B^+ \rightarrow J/\psi K^+$* . LHCb/PUB-2009-025, (March 2009).

- [109] Yao, W.-M. et al. *J. Phys.* **G33**, 1–1232 (2006).
- [110] Langenbruch, C., Uwer, U. Hansmann-Menzemer, S. *Fit of the decay  $B_s \rightarrow J/\psi\phi$* . LHCb/PUB-2009-028, (February 2009).
- [111] C. Linn, U. Uwer, S. Hansmann-Menzemer, C. Langenbruch. *Time and angular dependent analysis of  $B_d \rightarrow J/\psi K^{*0}$  decay*. LHCb/PUB-2009-015, (March 2009).
- [112] Calibration of flavor tagging with  $B^+ \rightarrow J/\psi K^+$  and  $B_d \rightarrow J/\psi K^{*0}$  control channels at LHCb. *M. Calvi, G. Lanfranchi, O. Leroy, M. Musy, S. Poss and S. Vecchi*. LHCb/PUB-2009-020, (2009).
- [113] D. Martinez, J.A. Hernando, F. Teubert. *LHCb potential to measure / exclude the branching ratio of the decay  $B_s \rightarrow \mu^+ \mu^-$* . LHCb/PUB-2007-033, (2007).
- [114] A.L. Read. *Modified Frequentist analysis of search results (the  $CL_s$  Method)*. CERN Yellow report 2000-005, (2000).
- [115] A. Ali, T. Mannel, T. Morozumi. *Forward backward asymmetry of dilepton angular distribution in the decay  $b \rightarrow sl^+l^-$* . Phys. Lett. B 273 505, (1991).
- [116] M. Beneke et al. *Systematic approach to exclusive  $B \rightarrow Vl^+l^-$ ,  $V\gamma$  decays*. Nucl. Phys. B 612:25-58, (2001).
- [117] M. Beneke et al. *Exclusive radiative and electroweak  $b \rightarrow d$  and  $b \rightarrow s$  penguin decays at NLO*. Eur.Phys.J. C 41:173-188, (2005).
- [118] H.P. Skottowe, M. Patel. *A cut based selection for  $B_d \rightarrow K^{*0}\mu^+\mu^-$  at LHCb*. CERN-LHCB/PUB-2009-008, (2009).
- [119] H.P. Skottowe, M. Patel. *A Fisher discriminant selection for  $B_d \rightarrow K^{*0}\mu^+\mu^-$  at LHCb*. CERN-LHCB/PUB-2009-009, (2009).
- [120] Gunnar, S. M. and Mika, S. *Fisher Discriminant Analysis With Kernels*, (1999).
- [121] I. Adachi et al. *Measurement of the Differential Branching Fraction and Forward Backward Asymmetry for  $B_d \rightarrow K^{*0}\mu^+\mu^-$* . arXiv:0810.0335v1, (2008).
- [122] B. Aubert et al. *Measurements of the branching fractions, rate asymmetries and angular distributions in the rare decays  $B \rightarrow K\ell^+\ell^-$  and  $B_d \rightarrow K^{*0}\mu^+\mu^-$* . Phys. Rev. D 73:092001, (2006).

